UNIVERSITY OF CALIFORNIA
RIVERSIDE

Charge and Spin Transport in Graphene Heterostructures and $Cr_2Ge_2Te_6$

A Dissertation submitted in partial satisfaction
of the requirements for the degree of

Doctor of Philosophy

in

Physics

by

Zhisheng Lin

September 2017

Dissertation Committee:
Dr. Jing Shi, Chairperson
Dr. Ward Beyermann
Dr. Nathaniel Gabor

The Dissertation of Zhisheng Lin is approved:

Committee Chairperson

University of California, Riverside

Acknowledgement

Getting a Ph.D. degree is not just finishing all the courses and passing all the exams. It is a self-disciplined process because you are not limited from showing your talent. It is also a self-motivating process because you are independent and no one is in charge of your failure. You are independent on cogitation but you are not alone. The success needs collaboration and teamwork. It is you to trigger discussion and encourage your colleagues to be involved in. You should welcome the suggestions but it is also important to think independently and insist on and fight for your own idea. These valuable experiences are what I learned from my advisor Prof. Jing Shi. He not only teaches me the rigorous logical thinking with his rich knowledge and clear physics pictures but also teaches me how to be a leader in a team as a senior student. It is very joyful and helpful to talk with him because he can always raise fundamental and profound questions to stimulate deeper thinking on my research. I want to express my deepest gratitude to Dr. Shi for helping me grow up to be an independent person. Without his enthusiasm, guidance, patience, encouragement and support, I could not achieve what I have today.

I would like to thank my committee member Professor Ward Beyermann for the useful discussion on my pressure cell projects and his kindness for teaching and letting me use the Quantum Design's physical property measurement system. I would also express my appreciation to Professor Nathaniel Gabor for helpful discussion on my graphene/TMD projects. I would also like to deeply thank Prof. Jeanie Lau, Prof. Vivek Aji and Prof. Jianlin Liu for their time being my qualifying exam committee members.

I would like to thank Professor Roland Kawakami for the collaboration of Al_2O_3 tunnel barrier project; Professor Wei Han and his student Wenyu Xing for providing the $Cr_2Ge_2Te_6$ sample; Yafis Barlas for his insightful comments and helpful discussions; Dong Yan, Dexter Humphrey, Nissim Amos and Frank Lee for the technical help in cleanroom. I would like to thank Derek Beving and all the other faculty members and staff in the Department of Physics and Astronomy, for their help and support during my Ph.D. career.

I also would like to acknowledge all my labmates and friends. I would like to thank Zhiyong Wang, Raymond Sachs and Tao Lin for teaching me the measurement skills and fabrication techniques. I would like to thank Junxue Li, Zhong Shi for the insightful discussion and the enthusiasm for physics. I am inspired by their rich knowledge in physics and the careful and serious attitude towards the research work. I would like to thank Peng Wei, Xinfei Liu, Hamad Alyahyaei, Zilong Jiang, Yadong Xu, Chi Tang, Bowen Yang, Mohammed Aldosary, Yawen Liu, Victor Ortiz and Benjamin Madon for their assistance, helpful discussion and precious friendship. I want to express special gratitude to Mark Lohmann for his huge help in the device fabrication and the numerous discussion and support when I am stuck in the projects and feel depressed. Thanks to my colleagues and friends for the kind help and friendship, they are Xiaoxiao He, Peng Wang, Bin Cheng, Yong Wu, Tengfei Miao, Fenglin Wang, Weimin Zhou, Changtao Hou, Yanmeng Shi, Yi Wu, Shaolong Chen, Supeng Ge, ShanShan Su and many others.

Last but not least, I want to express my deepest love to my parents and families. In such a long and tough Ph.D. career, it is the patience, care and love they give that help me insist on finishing the big challenge in my life. Love you all!

ABSTRACT OF THE DISSERTATION

Charge and Spin Transport in Graphene Heterostructures and $Cr_2Ge_2Te_6$

by

Zhisheng Lin

Doctor of Philosophy, Graduate Program in Physics
University of California, Riverside, September 2017
Dr. Jing Shi, Chairperson

This dissertation summarizes my past work on hydrogenation of graphene, development of Al_2O_3 tunnel barrier, pressure effects on $Cr_2Ge_2Te_6$ (CGT), and proximity effects in graphene/WSe_2 heterostructures. There are three main parts. The first part is the study of hydrogenation of graphene and the development of atomically smooth Al_2O_3 tunnel barrier. Graphene device is coated with hydrogen silsesquioxane (HSQ) resist and exposed with electron beam. Graphene is hydrogenated by forming the covalently bonds to the hydrogen atoms and transforms from sp^2 to sp^3 bonds. By breaking the inversion symmetry perpendicular to the graphene plane, Rashba spin orbit coupling (SOC) is enhanced. We characterized the hydrogenation effects by performing Raman spectroscopy measurements. A clear D and D$'$ peak grow abruptly with small hydrogenation dosage and keep growing with higher dosage, indicating the increased defects density in graphene. Electrical transport properties are characterized by measuring the gate voltage dependence at different hydrogenation percentages: mobility

decreases and graphene becomes more electron-doped upon hydrogenation. The hydrogenation process is reversible, which means the hydrogenation effects are almost gone after annealing. Nonlocal resistivity is 1 to 3 orders of magnitude larger than that of the pristine graphene, which cannot be accounted for by the ohmic contribution assuming uniform graphene channel. The problems of nonlocal measurement method are discussed. The rest of first part is focused on developing the atomically smooth Al_2O_3 tunnel barrier by sputtering a thin layer of aluminum first and oxidizing it in O_2 atmosphere.

The second part is about the pressure effects on the magnetic anisotropy of CGT. Magnetoresistance of CGT bulk crystal is measured under applied hydrostatic pressures up to 2 GPa. Upon the application of hydrostatic pressure, we observe an induced transition of easy axis from c axis to the ab plane of the crystal. Furthermore, we observe a reduction of the band gap of CGT by approximately 0.066 eV once the applied pressure reaches 2 GPa. We verify that the magnetoresistance (MR) change originates from anisotropic magnetoresistance (AMR) by measuring the temperature dependence of MR below and above Curie temperature (T_C) under the different applied pressures.

The last part is focused on the proximity effects in bilayer graphene/WSe_2 heterostructures and the pressure induced insulating behavior. The enhancement of spin-orbit coupling is verified by observing the weak-anti localization for the graphene region covered with WSe_2 but the weak localization (WL) for the uncovered region. The Rashba SOC strength value extracted from the weak-antilocalization (WAL) fitting is about 1 meV while the intrinsic SOC in graphene is about tens of μeV. It increases by more than two orders of magnitude. Graphene covered with WSe_2 shows a strong insulating

behavior by applying pressure and the insulating behavior is stronger under higher pressure, which is a signature of a band gap opening. Two hypotheses to explain the insulating behavior are discussed. One is the strain induced work function difference in top layer and bottom layer; this difference causes the charge transfer and builds up an electric field, generating the band gap. The other hypothesis is the proximity induced intrinsic electric field built across the bilayer graphene/WSe_2 heterostructure, resulting in the breaking of inversion symmetry.

Contents

Figures

Chapter 1 Introduction

Novel materials are in great demand for scientific research interests and future applications. Many two-dimensional (2D) materials exist in bulk form as stacks of strongly bonded layers in plane while with weak interlayer interaction, allowing for exfoliating into atomically thin layers.[1] In the family of 2D atomically layered materials, graphene stands out because of its extraordinary high mobility,[2] superb properties of conducting electron, heat[3] and spin. However, pristine graphene lacks a band gap, meaning that it cannot be effectively switched off. In contrast, 2D transition metal dichalcogenides (TMDs) possess sizable band gaps around 1-2 eV[4] and the tunability of selective photoexcitation of different carriers, which offers new opportunities in new field-effect transistors (FETs) and optoelectronic devices. Recent additions include Ising super conductors,[5-7] possible Mott insulators,[8] and topological semi-metals with edge transport.[8] In particular, CGT has been demonstrated to have intrinsic long-range ferromagnetic order in the atomic layers down to monolayer,[9] breaking the Mermin-Wagner theorem[10] due to magnetic anisotropy. This triggers a lot of interests in exploring layered 2D materials with intrinsic magnetism because it is another degree of freedom which can be utilized in magenetoelectronics.[11]

1.1 Graphene

Graphene is a single layer of carbon atoms arranged in hexagonal honeycomb format. The band structure[12] first calculated by P.R. Wallace in 1946 showed unusual semimetallic behavior. The unique electrical properties of graphene originate from its

special lattice structure. One s-orbital and two p-orbitals form the sp^2 hybridization, which corresponds to the σ band and forms a deep valence band. The σ band is responsible for the honeycomb lattice structure stability. The unaffected p_z orbital perpendicular to the planar structure forms the π band and contributes to the electrical properties of graphene.[13]

From the tight-binding model, the energy bands derived from Hamiltonian considering the nearest-neighbor hopping and next nearest-neighbor hopping can be written as[13]: $E_{\pm}(\vec{k}) = \pm t\sqrt{3 + f(\vec{k})} - t' f(\vec{k})$ (Eq 1.1)

with $f(\vec{k}) = 2\cos(\sqrt{3}k_y a) + 4\cos(\frac{\sqrt{3}}{2}k_y a)\cos(\frac{\sqrt{3}}{2}k_x a)$

where the plus sign denotes the upper (π*) band and the minus sign denotes the lower (π) band. If we don't consider the next nearest hopping, that is t'= 0, then the band structure is symmetric around zero energy, as shown in Fig. 1.1. The linear dispersion can be obtained by expanding the full band structure near the Dirac point as $E_{\pm}(\vec{k}) = \pm h\nu_F|\vec{k}|$ with the Fermi velocity ν_F ~ 1× 10^6 m/s.[13] Carriers in graphene behave as chiral massless particles: i.e., Dirac fermions, resulting in the striking difference from the massive charge carrier governing conduction in common semiconductor materials and the extremely high mobility. These unusual properties also lead to many novel physical phenomena, such as half integer quantum hall effect[14,15] and Klein tunneling.[16-20]

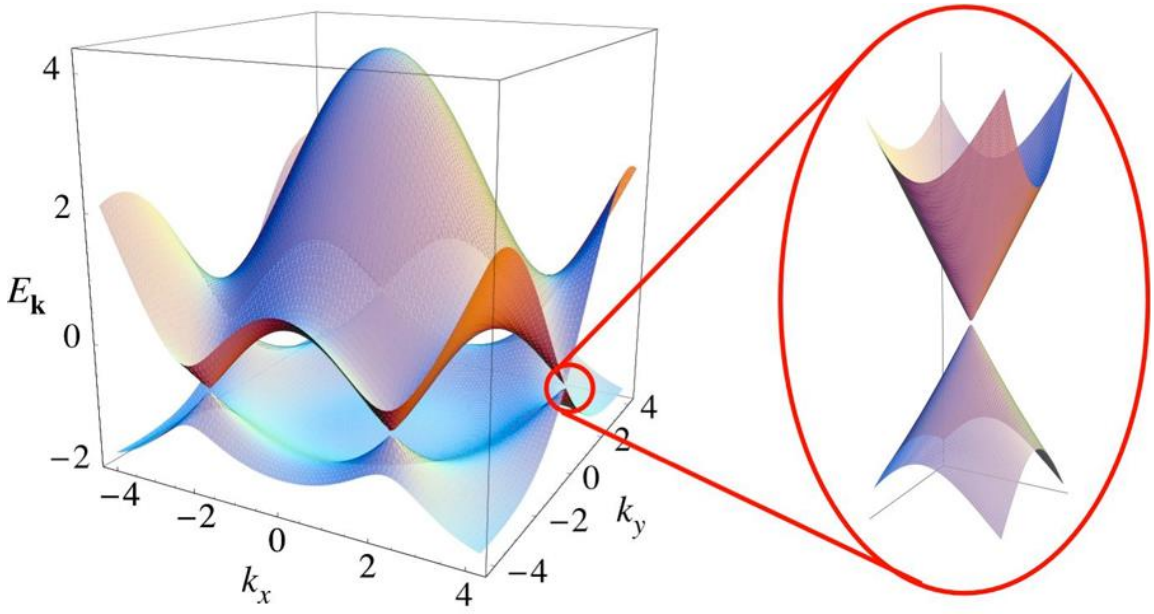

Figure 1.1. Band structure of graphene. Left: Energy spectrum (in unit of t) for finite values of t and t', with t = 2.7 eV and t' = -0.2t. Right: Zoom in of the energy bands close to one of the Dirac points. [Castro Neto, *et al*. *Rev Mod Phys* **81**, 109]]

Graphene has extremely small SOC with values about tens of μeV, this hinders the application for transistors. The method of hybridization with TMDs such as MoS_2[21], WS_2[22,23], WSe_2[21] to increase the SOC in graphene via proximity effect has been proved. Another approach is placing graphene on magnetic insulator, through which graphene will acquire both the magnetic exchange field and Rashba SOC.[24,25] With the presence of both effects, the anomalous Hall effect (AHE) has been experimentally observed.[24] Theoretical proposal of graphene/$BiFeO_3$[25,137] bilayer structure has shown that graphene opens a nontrivial gap at the Dirac point and forms a gapless topological edge states, enabling the realization of the quantized anomalous Hall effect (QAHE).

1.2 TMDs

TMDs are a class of materials with the formula MX_2, where M is a transition metal element from group IV (Ti, Zr, Hf and so on), group V (V, Nb, Ta), group VI (Mo, W), group VII (Mn, Tc, Re) or group X (Ni, Pd, Pt) and X is a chalcogen (S, Se or Te), as summarized in Fig. 1.2.[26] These materials form layered structures in the form X-M-X with strong in-plane bonding and weak out-of-plane interactions allowing for exfoliating into atomically thin layers.[27] The chalcogen atoms are in two hexagonal planes and separated by the metal atoms plane, as illustrated in Fig. 1.3. The electrical properties of TMDs vary in a broad range from metallic to semiconducting. There is a transition from an indirect band gap in the bulk to a direct gap in the monolayer, for example, the bulk indirect band gap of MoS_2 is 1.3 eV and it increases to a direct band gap of 1.8 eV in the single layer form.

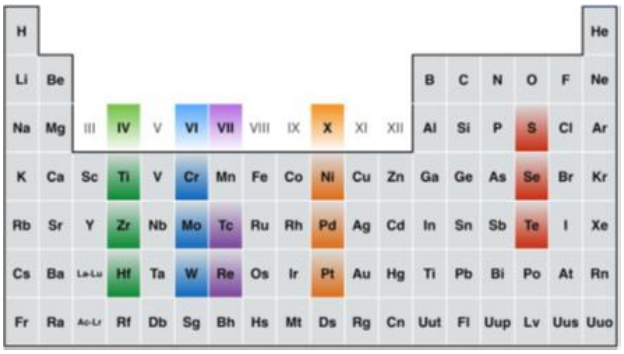

Figure 1.2. Periodic table with transition metal atoms (M) and chalogen atoms (X). [Qu, Yuanju, Hui Pan, and Chi Tat Kwok. *Scientific Reports* **6** (2016).]

Monolayer TMDs such as MoS_2, $MoSe_2$, WS_2 and WSe_2 lack inversion symmetry, which is different from graphene and bilayer MoS_2 being centrosymmetric.[28] The lack of inversion symmetry, together with confinement of electron motion in plane and heavy elements in the MX_2 lead to very strong SOC, with the valence-band splitting

ranging between 0.15 and 0.45 eV.[29] The strong SOC makes them promising candidates for spintronics devices. The spin-valley coupling at the valence-band edges in the monolayer of MoS_2 and other group-VI dichalcogenides suppresses spin and valley relaxation, which makes the selective photoexcitation of carriers with various combination of valley and spin indices realizable,[30-32] as shown in Fig. 1.4.[28]

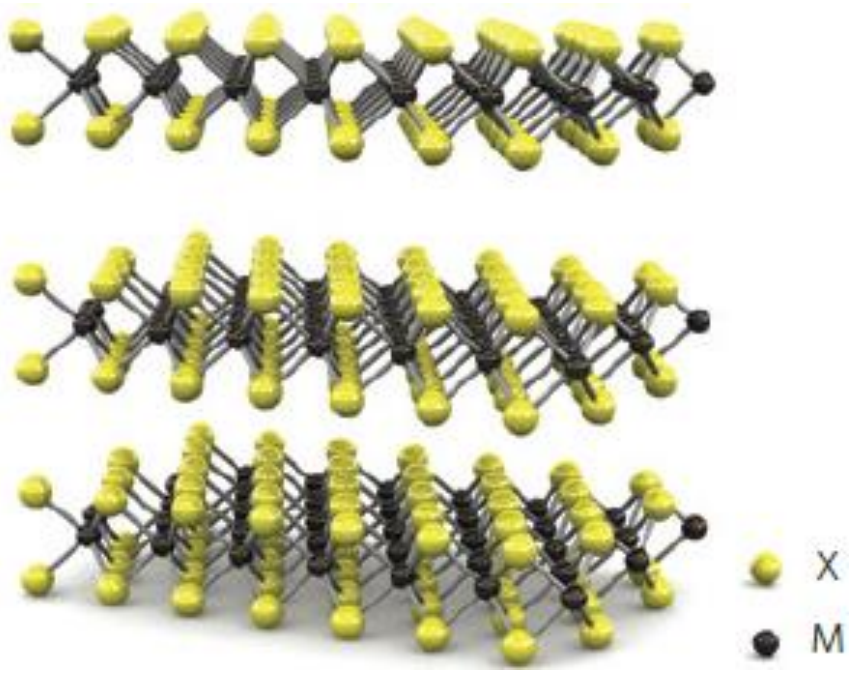

Figure 1.3. Three-dimensional schematic representation of a typical MX_2 structure. [Wang, Q. H., Kalantar-Zadeh, K., Kis, A., Coleman, J. N. & Strano, M. S. *Nature Nanotechnology* **7**, (2012).]

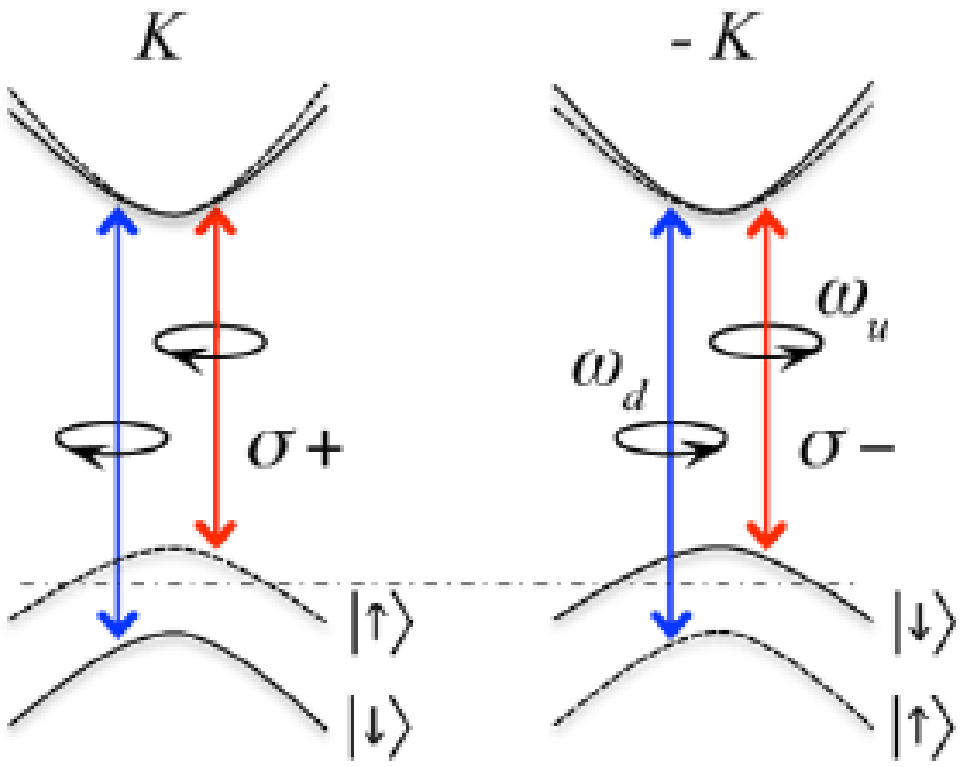

Figure 1.4. Valley and spin optical transition selection rules. [Xiao, Di, et al. *Physical Review Letters* **108** (2012)]

1.3 Ferromagnetic (FM) layered material

Recently, there is great interest in exploring the layered ferromagnetic materials due to the promising development in the functional van der Waals heterostructures.[33,34] If the layers composing of the crystal are held together by weak van der Waals (vdW) force, then they can be exfoliated into atomically thin layers by micromechanical cleavage using adhesive tape.[1,35,36] Two examples of this kind of material: $Cr_2Si_2Te_6$[37] with Curie temperature of 33K and $Cr_2Ge_2Te_6$[38] with Curie temperature 61K has been studied. The cleavage energy of these materials[39] is calculated to be 0.35-0.38 J/m^2, comparable to graphite (0.43 J/m^2) and MoS_2 (0.27 J/m^2).[40] Other similar layered ferromagnetic material

includes metallic Fe_3GeTe_2 with Tc = 220-230 K,[41-43] $CrSnTe_3$,[44] ferromagnetic few-layer-thick crystals of chromium tri-iodide[45] with Tc = 61K,[46] ferromagnetic $CrBr_3$ with Tc = 37 K,[47] and antiferromagnetic $CrCl_3$ with an ordering temperature near 17 K.[48,49]

The experimental progress in the device fabrication has enables exciting breakthroughs in the exploration of few-layers down to monolayer FM materials. The magneto-optic Kerr effect (MOKE) detection of magnetism in monolayer CGT[50] has been reported. Ferromagnetism has been experimentally confirmed in monolayer CrI_3 using MOKE.[45] The control of the spin and valley indices in monolayer WSe_2 using ultrathin CrI_3 has been demonstrated through a large exchange field effect.[33]

All these layered materials (graphene, TMDs, layered FM) are stacked together by the weak van der Waals (vdW) force and can be exfoliated into atomically thin layers. The electronic structures of TMDs and graphene have been found to be very sensitive to applied pressure.[86-88] Motivated by the same vdW nature of layered materials, it would be interesting to study the evolution of both the electronic and magnetic properties of CGT under an applied hydrostatic pressure. On the other hand, the proximity effects are very sensitive to the distance between the material and the adjacent materials or the substrate underneath. Hydrostatic pressure will be an efficient approach to decrease the interfacial distance and enhance the proximity effects in the graphene/TMDs heterostructure. In conclusion, pressure cell would serve as an effective tool to tune the interlayer distance of vdW materials and enhance the proximity effects in graphene heterostructures.

Chapter 2 Hydrogenation and Al_2O_3 tunnel barrier

Graphene is the first theoretically predicted 2D quantum spin Hall insulator or topological insulator.[51] But it requires very high mobility and extremely low temperature to overcome the impurity caused perturbation. The extremely small intrinsic SOC makes the realization of many interesting phenomena such as topological/quantum spin Hall states[52,53] and the spin Hall effect (SHE) practically impossible. From the application consideration, lacking a band gap hinder the applications in the transistors (cannot be switched off). Much efforts have been put on increasing the SOC in graphene by hydrogenation,[54,55] fluorination,[56] introducing adatoms[57,58] and coupling with TMDs[21-23] via proximity effect.

Graphene is an ideal two-dimensional (2D) material with high mobility, large Young's modulus[59] and low bending rigidity.[60] In graphene, the sp^2 hybridization forms the σ band. The unhybridized p-orbital is perpendicular to the plane and forms the π-band. The in-plane σ bond is very strong and this allows for large out-of-plane distortion. Due to this characteristic, hydrogenation of graphene is a promising approach to increase the SOC by converting from sp^2 to sp^3 bonds. The additional bonded hydrogen atom induces an electric field perpendicular to the planar structure and breaks the inversion symmetry. Here we present the work of increasing the SOC in graphene by controllable hydrogenation. Theoretically, hydrogenated graphene has been intensively studied because it offers valuable modifications of graphene properties depending on the coverage of graphene surface. In the high coverage regime, the insulating behavior was predicted[61-64] and later confirmed experimentally[54,65,66]. In this chapter, we study the

reaction of graphene with hydrogen atoms generated during electron beam initiated cross-linking of a HSQ (2%) film coated on graphene.

2.1 Device fabrication

The device fabrication starts with scotch-tape assisted exfoliation of graphene flakes on highly p doped 290-nm SiO_2 substrates. The single layer, bilayer and multilayer are firstly identified by the color contrast using optical microscope and the number of layers is confirmed by the Raman spectroscopy. The optical image of graphene flake before etching is shown in Fig. 2.1. A layer of MMA is spin-coated at a speed of 3600 rpm with a ramping rate of 5000 rpm/s followed by baking on a hot plate at 150 °C for 5 minutes. Then a layer of PMMA is spin-coated with the same recipe but baked at 180 °C for 5 minutes. To precisely control the pattern position and shape, a set of alignment marks are written using the electron beam lithography system (Leo SUPRA 55) around the graphene flakes. The alignment marks are developed using the solution with the ratio of MIBK (Methyl isobutyl ketone) and IPA (isopropyl alcohol) to be 1: 3 for 65 s or the solution with ratio of DI water and IPA to be 1:3 for 10 minutes depending on the precision requirement of the pattern. The developing rate of the latter solution is slower and gives better control of developing fine patterns, especially when the distance of two electrodes is small. It significantly decreases the risk of connecting two electrodes due to over develop since the undercut developed by the MIBK/IPA solution is wide. Then the Cr/Au (5nm/50nm) alignment marks are deposited with electron beam evaporation system (Temescal BJD-1800). To lift off, the device sits in acetone on a hot plate at

65 °C for overnight. Then different magnifications of optical microscope images of the graphene area with alignment marks are taken for the next step of etching and electrodes pattern design. Usually, the flakes will be etched into hall bar shape. Then the gold electrodes (50nm to 80nm) are deposited on the device. A typical SEM image of etched device is shown in Fig. 2.2.

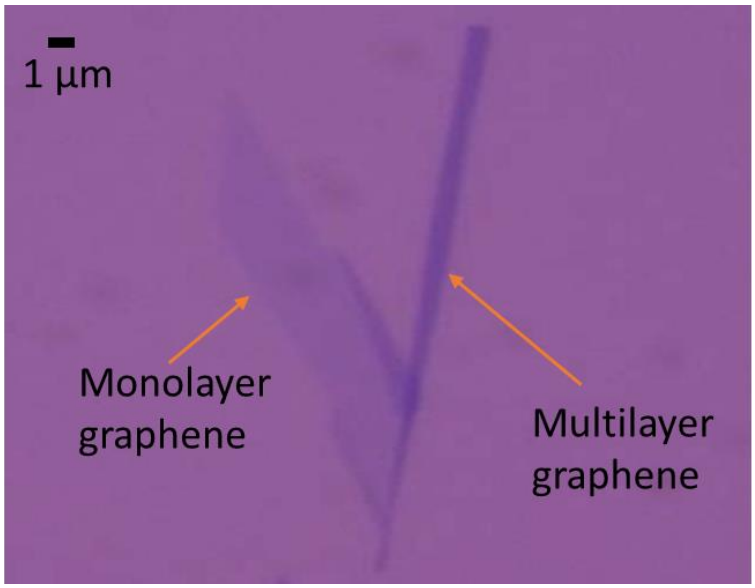

Figure 2.1. Optical image of the graphene flake with magnification 500 before etching. It is micromechanically exfoliated on SiO_2.

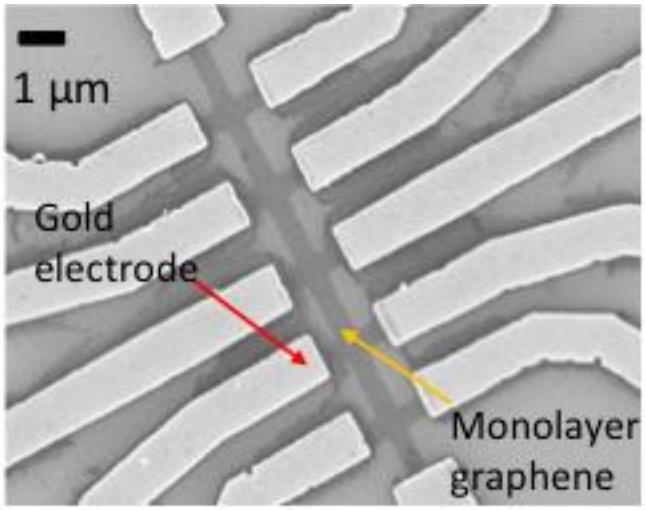

Figure 2.2. SEM image of graphene device. Graphene has been etched into hall bar with width 0.5 µm.

To hydrogenate graphene, HSQ resist is spin-coated on the device with a ramping rate of 5000 rpm/s and speed 5000 rpm and for 60 s. The thickness of HSQ film is about 32 nm after spin coating. Then the device is moved to a hot plate and the resist is baked at 250 °C for 2 min. The hydrogenation process introduces small amount of covalently bonded hydrogen atoms to the graphene lattice by the dissociation of HSQ resist with e-beam lithography. The electron beam breaks the Si-H bond in the HSQ resist and the released hydrogen atom rebind together with carbon atom, as shown in Fig. 2.3. After exposure with e-beam, the resist is developed with 2.3% TMAH (MF319) at RT for 70 s. HSQ is a negative resist, that is, the unexposed part will be developed away and exposed part will stay. Finally, we gently rinse the device with flowing DI water for 30 s.

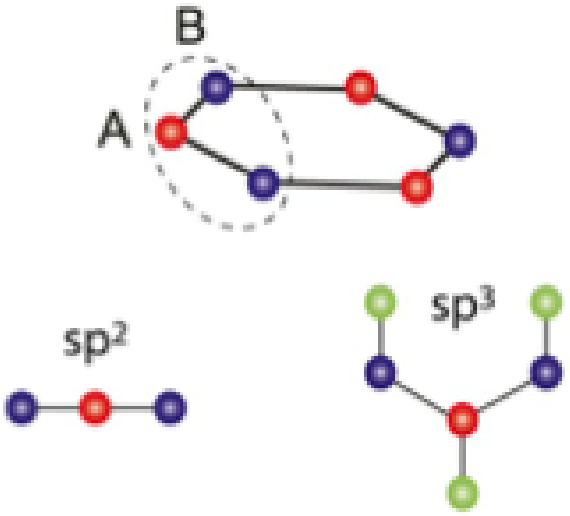

Figure 2.3. Schematic diagram to show the hydrogenation process. The released hydrogen atoms rebind together with carbon atoms and graphene structure transit from sp^2 hybridization to sp^3 hybridization.

2.2 Raman spectra

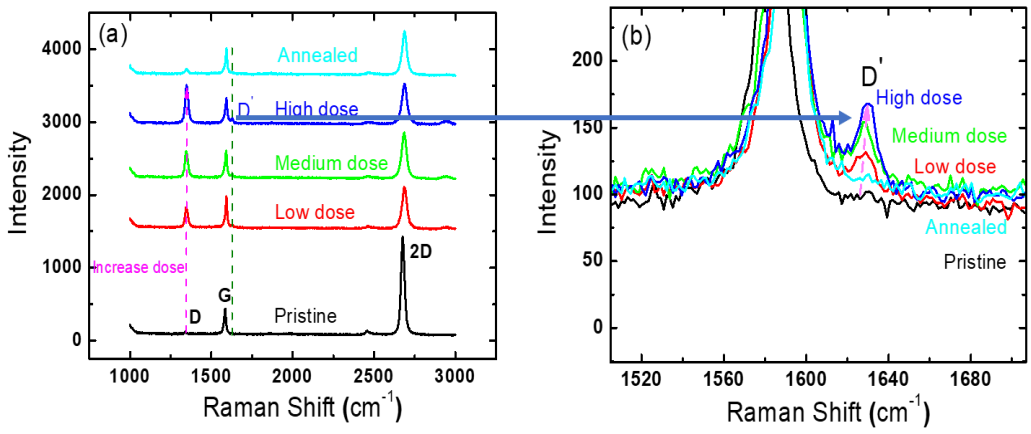

Figure 2.4. (a) Raman spectra of hydrogenated graphene. D-peak increases as the e-beam dosage on HSQ increases, which indicates an increase in the hydrogenation coverage. [I. Childres, *et al*. New developments in photon and materials research 1 (2013)] (b) Zoom in of the Raman spectrum in the range of 1500-1700 cm^{-1}. D' peak grows with increasing dose and recovers to the pristine state after annealing.

Raman technique is sensitive to detect the impurities in graphene, reflecting in the D-peak and D'-peak in Raman spectrum. We first characterize the change with Raman measurement while increasing the hydrogenation dosage gradually.

For the pristine graphene, there is negligible D-peak, indicating the absence of significant defects. At low dosage, there is a dramatically increase in the D-peak intensity, which means the impurities in graphene increases. This is an indicator that the hydrogenation has occurred. With increasing the dosage to medium and high, the D-peak keeps growing. After annealing, the D-peak decreases to a small value, which is just slightly stronger than that of the pristine state, as shown in Fig. 2.4 (a). In addition to the D-peak, there is a clear development of the D'-peak with increasing dose, which is shown in Fig. 2.4 (b). The D-peak and D'-peak are caused separately by intervalley and intravalley phonon and defect scattering, as illustrated in Fig. 2.5 (a), indicating the short-range scattering in graphene increases. The ratio of the intensities of the *D* peak to G peak can be used to estimate the defect density of the graphene flake[67] using the following equation:

$$n_D(cm^{-2}) = \frac{(1.8\pm0.5)\times10^{22}}{{\lambda_L}^4}\left(\frac{I_D}{I_G}\right) \qquad \text{(Equation 2.1)}$$

Here, n_D is the defect density in graphene, I_D is the intensity of D peak, I_G is the intensity of G peak and λ_L is the wavelength of the laser used in the Raman system (Horiba LabRam), which is 532 nm. The impurities density increases monotonically with increasing dose, as shown in Fig. 2.5 (b), indicating the successful hydrogenation.

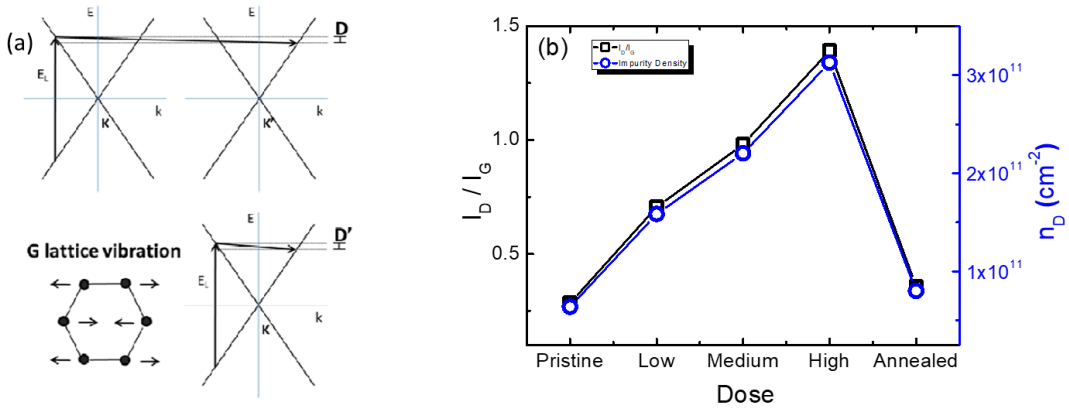

Figure 2.5. (a) Different scattering processes responsible for D-peak and D'-peak in the Raman spectrum. (b) D/G peak intensity ratio and calculated impurity density. The effect of hydrogenation as indicated by the D/G peak ratio is reversible upon annealing. SOC is expected to change accordingly.

2.3 Gate voltage dependence

To better understand the changes in the electronic transport property, we measured the gate voltage dependence for every different dose. Resistivity versus carrier density is plotted, as shown in Fig 2.6 (a). From pristine, low dose, to medium dose, the resistivity monotonically increases, which is consistent with the Raman spectra that more impurities are introduced. From medium dose to high dose, the resistivity slightly increases. After annealing, the resistivity decreases but is still larger than the pristine graphene, especially in the high-density region. It is clearer to see the decrease in mobility if we plot conductivity versus gate voltages, as shown in Fig 2.6 (b). In conclusion, mobility decreases with increasing dosage and annealing does not completely restore the device: some of the hydrogenation effects remain.

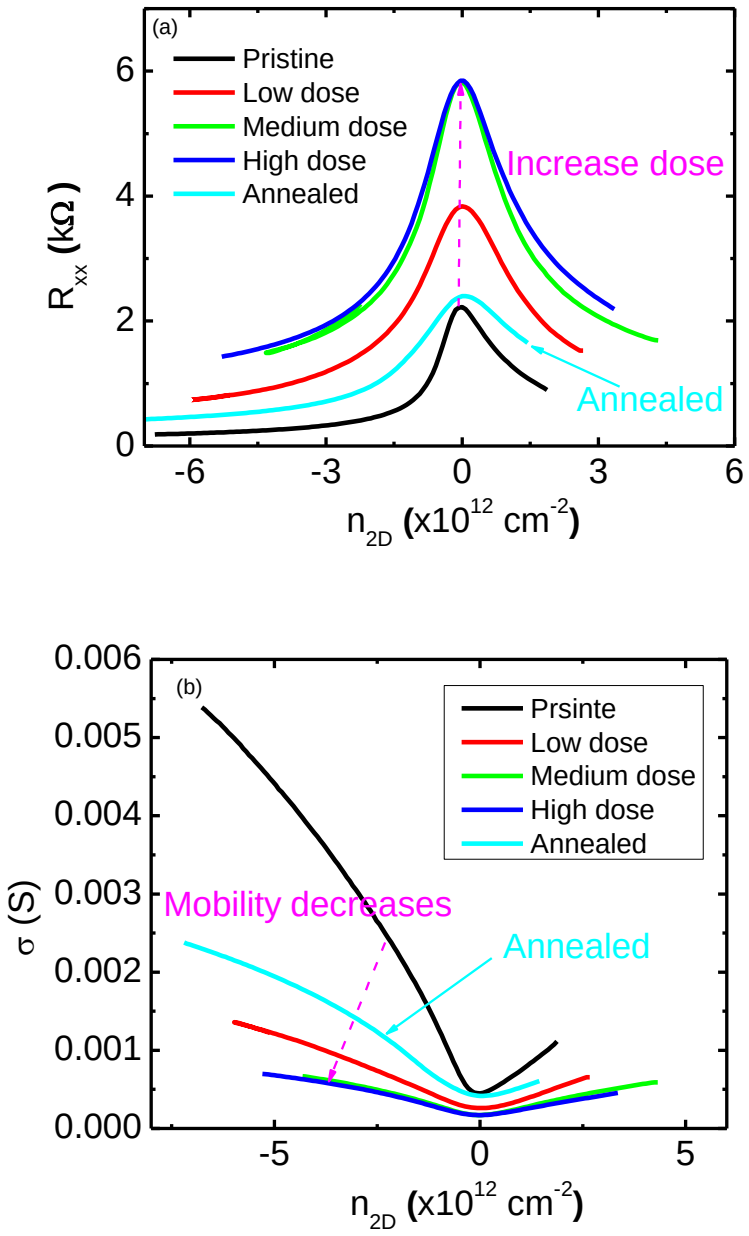

Figure 2.6. Comparison between different doses. (a) Resistivity for different doses. Resistivity increases as e-beam dose increases. Annealing undoes some hydrogenation effect. (b) Conductivity for different doses. Mobility decreases with increasing doses.

2.4 SHE/ISHE

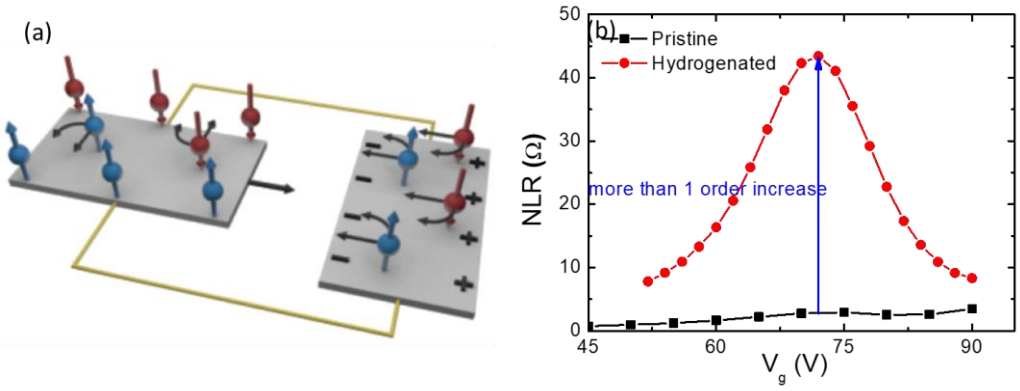

Figure 2.7. Non-local resistance. (a) Schematic diagram of spin Hall effect [Sinova, Jairo, *et al*. "Spin hall effects." *Reviews of Modern Physics* **87** (2015)]. (b) Comparison of non-local resistivity (NLR) between the pristine and hydrogenated graphene. The NLR in hydrogenated graphene is 1 to 3 orders of magnitude larger than pristine graphene.

To verify that the SOC in graphene is enhanced by hydrogenation, we conduct the non-local resistivity measurement: injecting current in one of the Hall pairs and detecting the non-local voltage signal in the adjacent Hall pair, as shown in Fig 2.2. SHE is the phenomenon that a flowing current in material with strong SOC will induce a transverse pure spin current on the lateral edge with spin polarization perpendicular to both the charge current and spin current, as shown in Fig. 2.7 (a). In the injection region, due to the SHE, a spin current flows along the graphene channel, while in the detection region, the propagating spin current converts to a charge current due to ISHE and the charge build up at the boundaries of the detection hall bar. The Non-local resistance (NLR) is defined as the voltage difference in the detection hall bar over the charge current in the injection region.[55] After hydrogenation, the NLR is 1 to 3 orders larger than the pristine graphene, as shown in Fig. 2.7 (b), which cannot be accounted for ohmic contribution since it only depends on the aspect ratio and the graphene resistivity. The detailed

explanation is in the next section. The NLR signal due to SHE is $R_{NL}/\rho = \frac{1}{2}\gamma^2 \frac{w}{\lambda_s} e^{-L/\lambda_s}$.[68] Here γ is the spin Hall angle, w is the width of the graphene channel and λ_s is the spin diffusion length. If R_{NL}/ρ is plotted as a function of different lengths, as shown in Fig. 2.8, one can extract out the λ_s and γ. There are only two data points, as shown in Fig 2.7, so it is not possible to do a good fitting. From these two data points, we can get $\lambda_s = 1.5\ \mu m$, which is a typical value for graphene devices. The calculated γ is 0.45, which is anomalously large for graphene, suggesting that the hydrogenated graphene behaves differently from the pristine graphene. There are two artifacts in the NLR signal, one is ohmic contribution and the other one is spurious signal originating from the measurement setup, as discussed in the section 2.5 and 2.6.

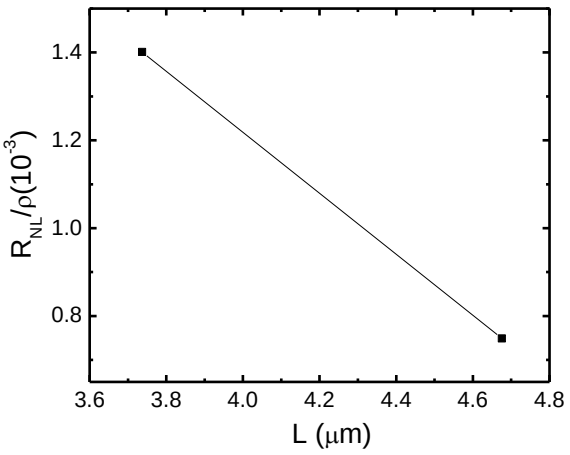

Figure 2.8. NLR as a function of length. There are only two data points, so it is not effective to do the fitting.

2.5 Ohmic contribution

The ohmic contribution[68,69] for a perfectly uniform rectangularly shaped graphene channel with length L and width W can be expressed as the following equation: $R_{ohmic} =$

$\rho e^{-\pi L/W}$, as shown in Fig. 2.9 (a). It decays exponentially with aspect ratio and the value is about 0.08 Ω when the aspect ratio increases to 3, as shown in Fig. 2.9 (b). The calculated ohmic contribution is small with value less than 1 Ω while the measured NLR is about 45 Ω in this specific device. The ohmic contribution is negligible compared with NLR, as shown in Fig. 2.9 (c). The above calculated ohmic contribution is only true for a perfectly uniform rectangularly shaped, there is possibility that the channel can be non-uniform so that the equation is not applicable, inducing large spurious non-local signal. So, there are two possibilities: small ohmic and non-uniformity from the discussion here.

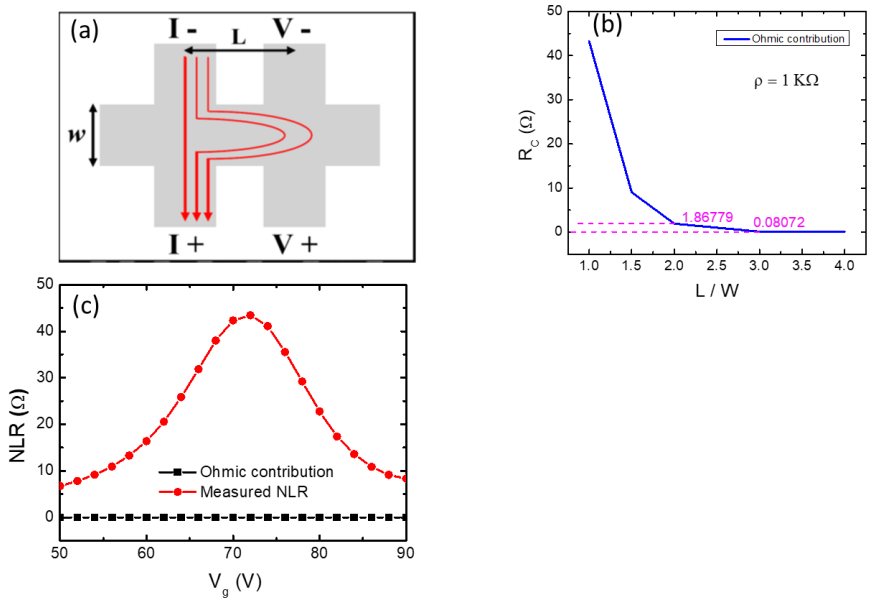

Figure 2.9. Ohmic contribution. (a) Schematic diagram of the ohmic contribution. Its magnitude depends on the aspect ratio of the device. [Mihajlović, G., *et al. Physical review letters* **103** (2009)] (b) Dependence of calculated ohmic contribution on the aspect ratio. (c) Comparison between NLR and ohmic contribution. NLR in hydrogenated graphene is 1 to 3 orders of magnitude larger than ohmic contribution from perfectly uniform rectangular graphene channel, indicating the dominant role in hydrogenated graphene.

2.6 Spurious signal

Measurement artifacts may appear when using typical lock-in amplifier (SR830) setup.[70] For a typical nonlocal measurement, the spurious signal came from the common mode voltage V_{CM} at the current injection side of the Hall bar (marked by the red dot in Fig 2.10 (a)). The input impedance R_{input} of lock-in amplifier is about 10 MΩ to the ground. Resistance difference at the two nonlocal leads could produce a spurious voltage difference at the input of lock-in amplifier: $V_{NL}^{s} = \frac{V_{CM}R_A}{R_{input}+R_A} - \frac{V_{CM}R_B}{R_{input}+R_B} \approx (R_A - R_B)\frac{V_{CM}}{R_{input}}$. Here, R_A and R_B are the total resistance from the red dot in Fig 2.10 (a) to the input of the lock-in amplifier including graphene resistance, contact resistance at the nonlocal electrodes, and resistance of the voltage leads, which is on the order of 1 MΩ. Typically, V_{CM} ~ 1 mV = 1 KΩ (graphene resistance) × 1μA (source current amplitude) and the difference between R_A *and* R_B is ~ 10 KΩ, this will induce a spurious signal on the order of ~ 0.1 μV. This is very small compared with NLR signal, which is about 40 μV in the device shown in Fig. 2.9. The spurious signal cannot be the dominating one unless the contact resistance is very large, resulting the large value of $(R_A - R_B)$. If the value of $(R_A - R_B)$ goes up to 100 KΩ, then the spurious signal can go up to 1 μV.

The spurious voltage V_{NL}^{s} can be eliminated by replacing the lock-in amplifier with large input impedance of the voltage meter such as Keithley 2182A nanovoltmeter (R_{input} > 10 GΩ) as shown in Fig 2.10 (a). For the current source, the Keithley 6221 precision current source operating in delta mode serves as a suitable candidate.

In addition, if the current polarity is flipped, the spurious voltage signal does not change sign. The sign is only determined by the sign of $(R_A - R_B)$. However, the non-local voltage signal caused by the SHE/ISHE changes sign as the current polarity is flipped, as shown in Fig 2.10 (d). This contrary response can be used as a criterion to distinguish the real NLR from the spurious signal, but it cannot be used to exclude ohmic contribution.

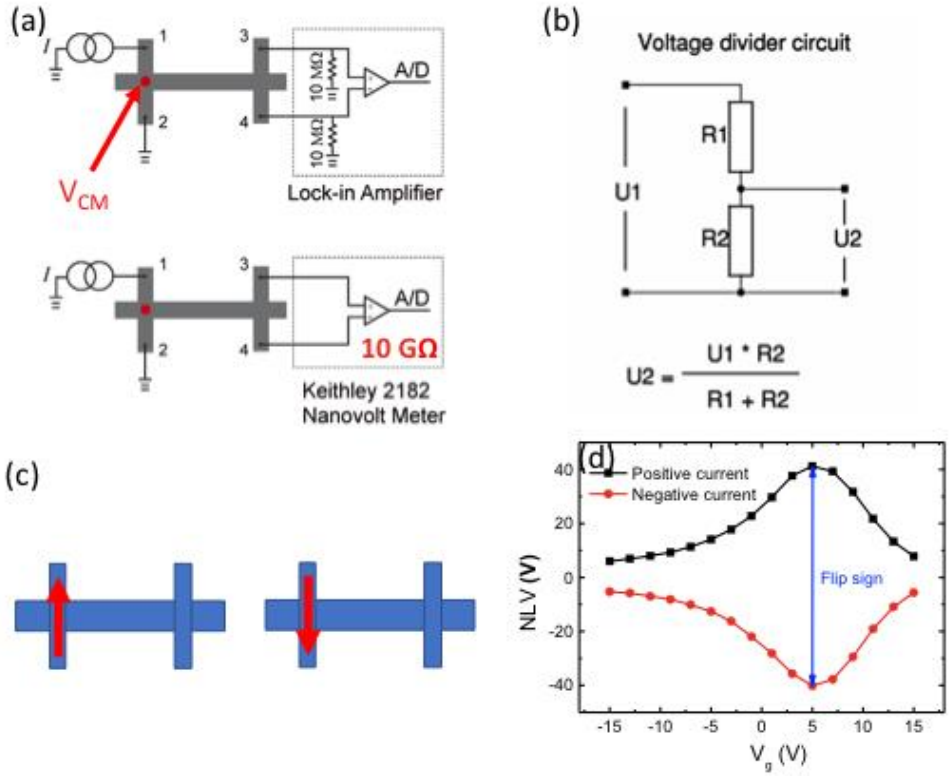

Figure 2.10. Spurious signal. (a) Schematic diagram to show the origin of spurious signal caused by lock-in amplifier [M. Sui, *et al. Nat. Phys.* **11** (2015)]. (b) The voltage drop between the red dot and pin 3 can be understand as the voltage divider model. (c) The schematic diagram to show the opposite current polarity. (d) For opposite current polarity. The positive and negative currents give opposite sign of signal, which supports that the NLR signal originates from SHE.

2.7 Partially hydrogenated graphene

The mobility decreases with increasing hydrogenation dose, which will shorten the spin lifetime and lowers the NLR signal. Since the SHE/ISHE only happen in the hall pair region and spin current propagates in the graphene channel, leaving the channel region as pristine state should in principle increase the NLR signal compared with fully hydrogenated as it increases the spin lifetime in the propagating process, as shown in Fig. 2.11.

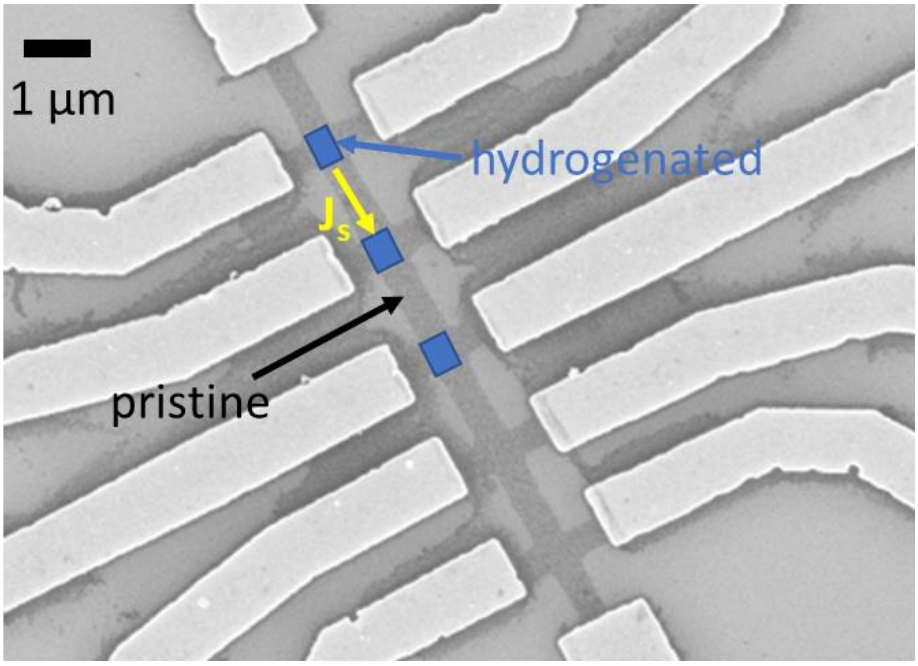

Figure 2.11. SEM image of the graphene. The blue square region is the hydrogenated region while the channel region is preserved as pristine.

2.7.1 Gate dependence of the pristine and partially hydrogenated graphene

As shown in Fig. 2.12, after hydrogenation, there is an additional shoulder peak showing up by the main peak. The hydrogenation process is the reaction of covalently

bonding of hydrogen atoms with the carbon atoms, resulting in the n-doping of graphene. From Fig. 2.6, the resistance of graphene increases upon hydrogenation. Hence, the more n-doped and higher resistance peak around zero volt in Fig. 2.12 is the hydrogenated region while the less n doped and shoulder peak is the pristine region.

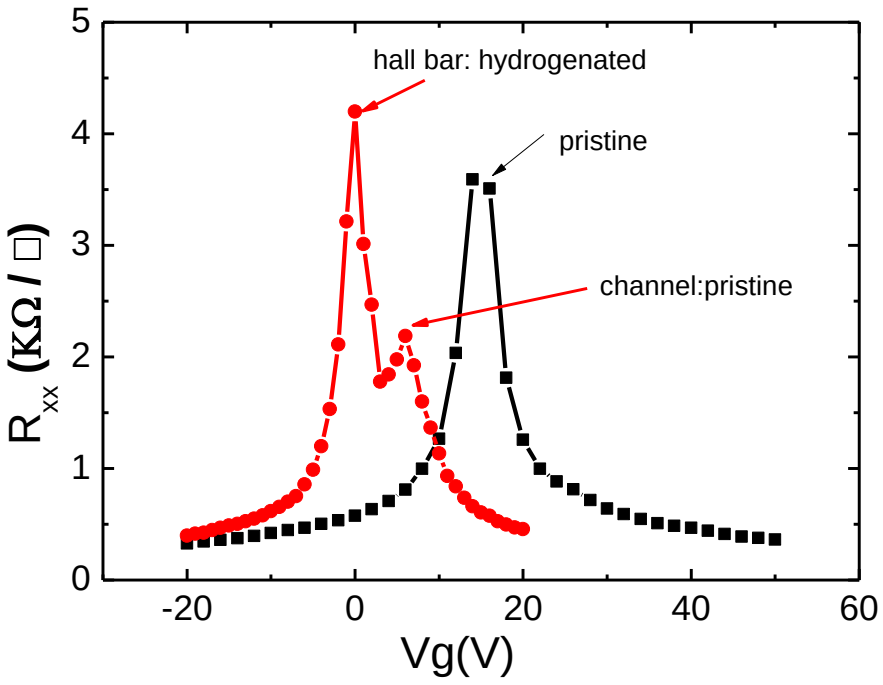

Figure 2.12. Gate voltage dependence of pristine graphene and after hydrogenation. The main peak around zero is dominated by the hydrogenated graphene while the shoulder peak around 8V is dominated by the pristine graphene.

2.7.2 MR of pristine and hydrogenated region

Before hydrogenation, the graphene shows WL, which is typical in pristine graphene in the presence of strong intervalley and intravalley scattering. After hydrogenation, the pristine dominated channel shows suppressed WL while the

hydrogenated region turns into WAL, as shown in Fig. 2.13, indicating the enhanced SOC in graphene.

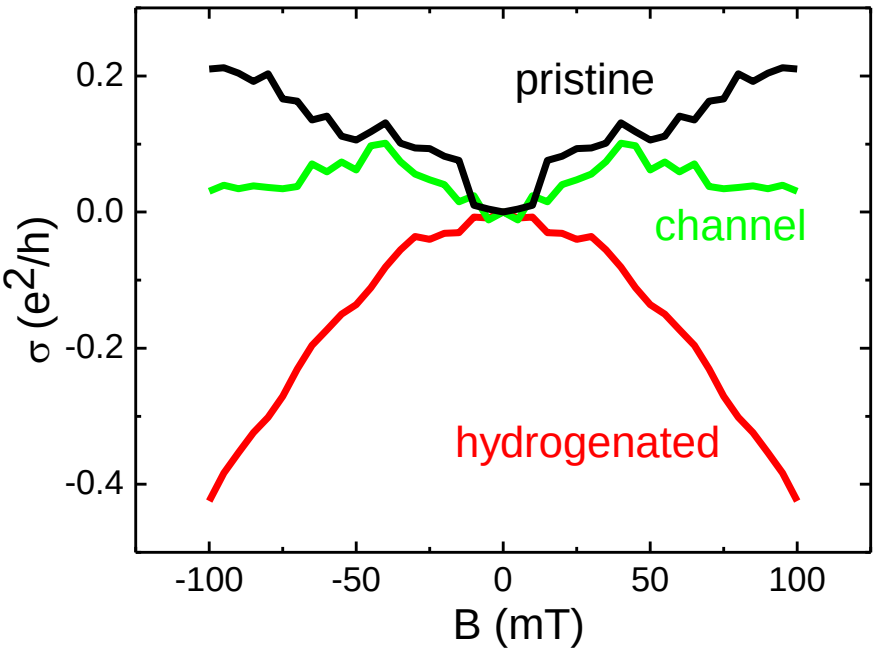

Figure 2.13. MR comparison before and after hydrogenation.

In conclusion, hydrogenation has been successfully demonstrated by Raman spectroscopy and NLR measurements. Raman D-peak is a clear indicator of increased defects in hydrogenated graphene. Hydrogenated graphene has much larger NLR compared with that of the pristine graphene. The enhanced NLR could arise from stronger SHE/ISHE given by strengthened SOC due to broken inversion symmetry or non-uniformity caused by defects. However, the anomalously large spin Hall angle is not expected from carbon-based materials. In addition, Kaverzin, A.A. *et al* reported that no

modulation of the NLR is observed when an in-plane magnetic field is applied and argued against the spin Hall model,[134] leaving the huge NLR signal as an open question.

2.8 Al_2O_3 tunnel barrier and graphene spin valve

Electrical spin injection is a necessary condition for graphene spintronics. For graphene spin valve device, a current source is injected between the electrodes E1 and E2,[94] where E2 serves as the spin injector. After spin injection, the spin current will diffuse towards E3, then the spin is detected as the voltage difference between E3 and E4, as shown in Fig. 2.14. There are two types of junctions, the first type is the transparent junction, where the ferromagnetic electrodes are in direct contact with the graphene, but there is conductivity mismatch problem,[71-73] causing the inefficiency of spin injection. The second type is the tunnel junction, where a thin insulating layer is inserted to solve the conductivity mismatch problem to produce a large spin valve effect. The quality of the inserted tunnel barrier material is critical for spin injection. It must be flat and homogeneous with a thickness in the 1 nm range.[76] Growing on high quality ultra-thin dielectrics while preserving the high quality of graphene is challenging and previous attempts have severe wetting difficulties.[135,136] Here we produce the atomically smooth Al_2O_3[74,75] deposited by a sputtering system, which simplifies the process and have a satisfactory yield. The detailed device fabrication steps are as followings:

Step 1: Sputter 0.6 nm Al on graphene with Ar flowing pressure 5.5 mTorre, power 5% for 13 s.

Step 2: Oxidize at atmospheric pressure of O_2 for 30 min.

Step 3: Spin coat with ebeam resist.

Step 4: Define electrodes with ebeam lithography (EBL).

Step 5: Deposit FM contacts with molecular beam epitaxy (MBE) system.

Al_2O_3 tunnel barrier is grown over the entire sample. It can therefore serve as both a tunnel barrier and a protective layer for the graphene. We first characterize the film surface with AFM. Fig. 2.15 shows an AFM image of 1 nm of Al_2O_3 on top of a single layer graphene. The rms roughness is about 0.117 nm and there are no observable pinholes at thickness 1 nm. This suggests that sputtered aluminum with post oxidation could be an excellent tunnel barrier candidate.

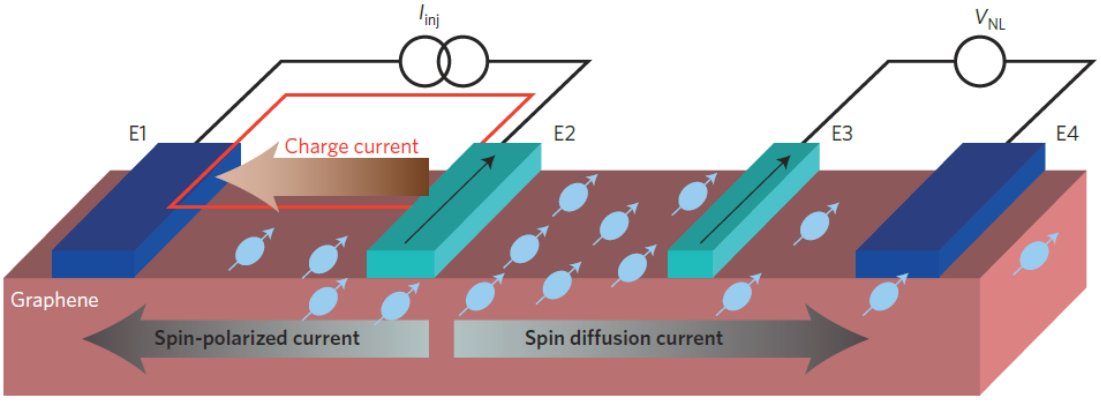

Figure 2.14. Spin injection and transport in graphene spin valve device. [Han, W., Kawakami, R. K., Gmitra, M. & Fabian, J. Graphene spintronics. *Nature Nanotechnology* **9** (2014).]

To check for possible sputtering-induced defect formation, Raman spectroscopy is performed before and after Al_2O_3 deposition, as shown in Fig. 2.16. A relatively small D peak (~30% of G peak magnitude) appears, which indicates the presence of fewer sputtering-induced defects in graphene layer compared to previous studies[76,77] because of the precise control of deposition rate and the oxidization in high purity of O_2 for half an hour.

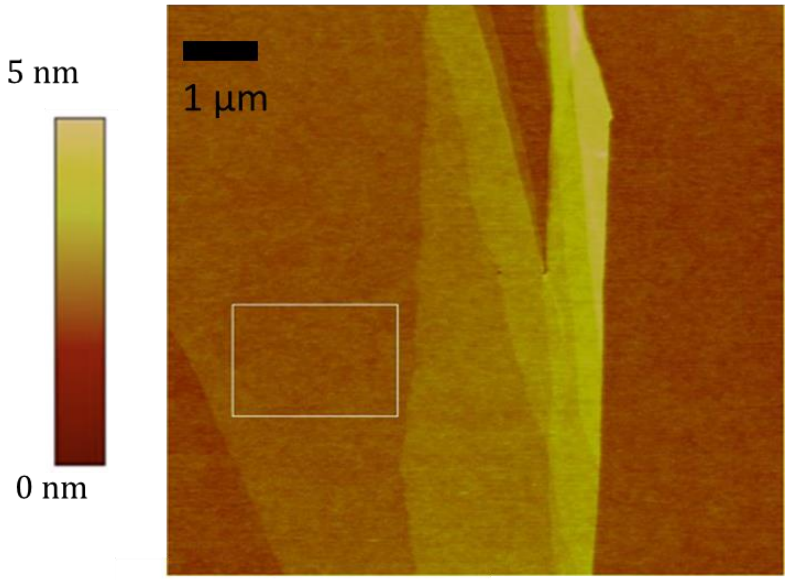

Figure 2.15. AFM image of 1 nm Al_2O_3 on graphene. The Al_2O_3 is smooth without observable pinholes.

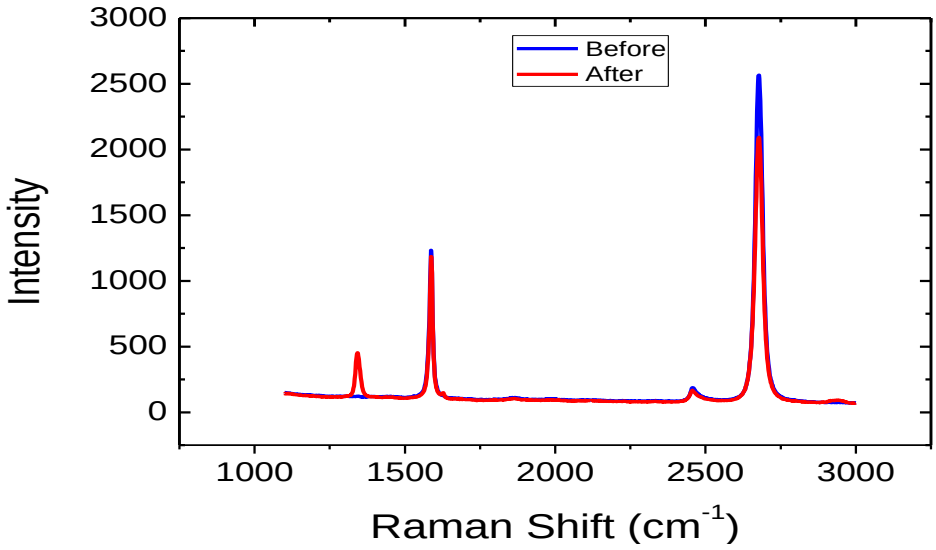

Figure 2.16. Raman spectra of graphene before (blue) and after (red) deposition of 1 nm Al_2O_3. There is a relatively small D peak appearing after deposition.

We characterized the electrical properties of the 1nm Al_2O_3 by measuring the gate dependence and three terminal differential contact resistance dV/dI. First, the 4-probe resistance is measured as a function of gate voltage to determine the charge neutrality point and field effect mobility of the graphene. The gate dependence as shown in Fig. 2.17 (a) is a typical for graphene with a 1 nm Al_2O_3 tunnel barrier. The charge neutrality point is at V_G = 15V with a relatively small hole doping. The calculated carrier density at zero gate voltage is $1.08\times10^{12} cm^{-2}$ (holes) using the capacitance model. The extracted mobility from the slope of the gate dependent conductivity σ is μ_e = 3005 cm^2/Vs for electrons and μ_h = 948 cm^2/Vs for holes. The tunneling property of the 1 nm Al_2O_3 is characterized by measuring the three terminal dV/dI at V_G = 0V. The measurement is performed using lock-in with an AC current of 1 μA at 211 Hz injected between contacts E1 and E4 and measuring voltage between E2 and E3. Fig. 2.17 (b) shows typical curves that exhibit a cusp-like behavior as a function of DC bias.

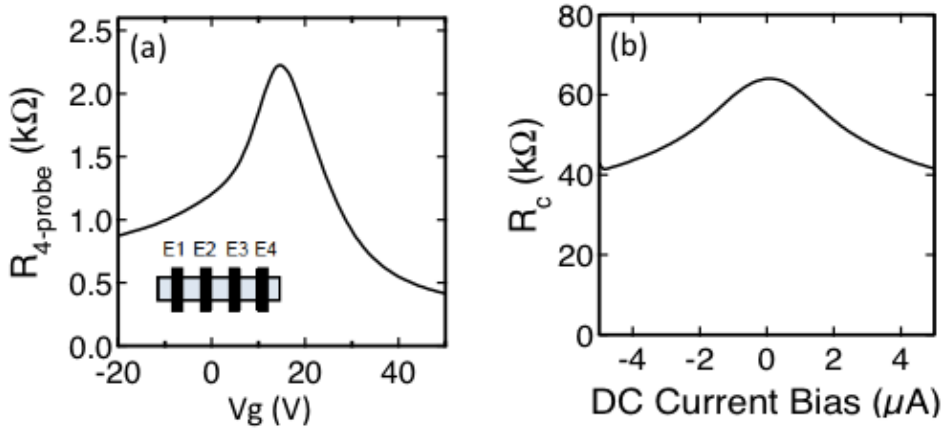

Figure 2.17. Electrical properties. (a) Gate dependence of 4-probe resistance of a graphene spin valve. (b) Three terminal differential contact resistance dV/dI of Al_2O_3/graphene junction.

Finally, we characterize the quality of Al_2O_3 by investigating spin transport in graphene spin valve. An AC injection current of 1μA rms at 11 Hz is injected between electrodes E1 and E2 (injector), generating a non-local voltage V_{NL} measured between electrodes E3 and E4. Spin transport measurements is performed by ramping an in-plane magnetic field to achieve parallel and antiparallel alignments of the injector and detector magnetizations. For Hanle spin precession measurements, an out of plane magnetic field is applied to have parallel and antiparallel alignments of the injector and detector magnetizations, as shown in Fig. 2.18. At room temperature, the size of the nonlocal magnetoresistance (ΔRNL) is ~ 25 Ω with average contact resistance R_C of 58 kΩ. Hanle spin precession measurements with an out-of-plane magnetic field are performed to extract the spin lifetime and spin diffusion length. The spin lifetime is about 685 ps using the traditional model.[78]

In conclusion, the atomically smooth tunnel barrier Al_2O_3 is developed with a simplified and efficient sputtering method. The Raman spectra and AFM image show good quality of the tunnel barriers and is confirmed by the electrical and spin transport measurements.

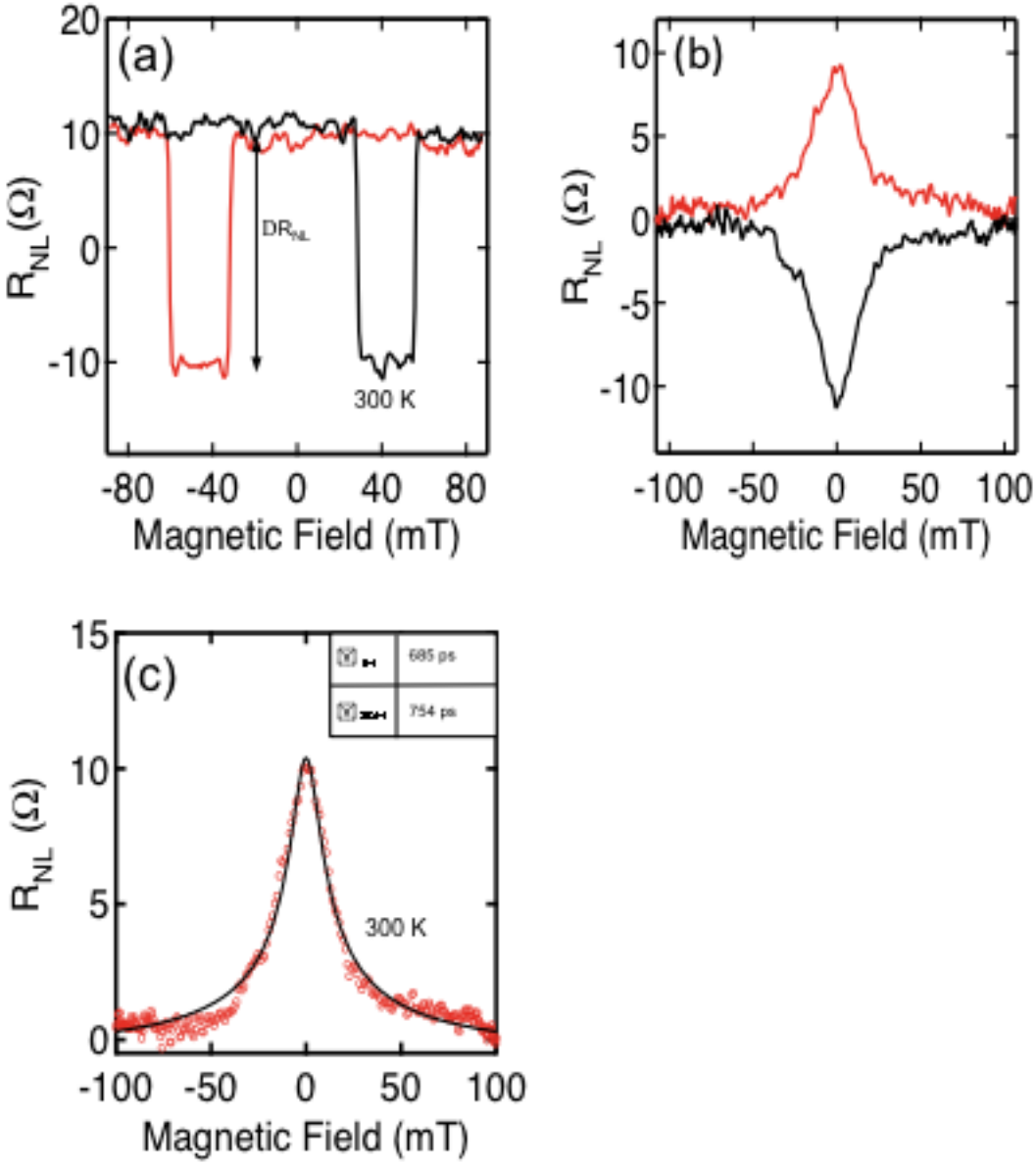

Figure 2.18. Spin transport properties. (a) Non-local MR of a graphene spin valve with Al_2O_3 tunnel barrier for in plane magnetic field swept upward(black) and downward(red). (b) Hanle spin precession of a graphene spin valve with Al_2O_3 tunnel barrier for parallel (red) and antiparallel (black) magnetizations of the injector and detector ferromagnets. (c) Fitting of parallel minus antiparallel Hanle curves using the traditional model which doesn't explicitly take spin absorption into account and the spin absorption model.[79-81] [Amamou, Walid, *et al*. *APL Materials* **4** (2016)]

Chapter 3 Introduction of pressure cell and setup

3.1 Introduction of pressure cell (Note: The following paragraphs and figures are used with permission from Almax easyLab.)

The pressure cell used here is Almax easyLab Pcell 30. The easyLab Pcell 30 module has been specifically engineered to enable end users to perform AC transport measurements under high-pressure up to 3 GPa, low temperatures down to 2 K and high magnetic fields up to 14 T assembled with Quantum Design Physical Properties Measurement System (PPMS). First part is the Pcell 30, as illustrated in Fig. 3.1. The way the cell is pressurized is by applying a known force on a series of tungsten carbide pistons. In turn, the PTFE cap, where the sample is sitting surrounded by the transmitting medium, has its volume reduced and hence the pressure increases. Safety is the first priority! Remember to read throughout the user's manual and follow the safety procedures to protect yourself and the equipment. The second part is the Ppress hydraulic system, as shown in Fig. 3.2. It facilitates the applying pressure process and ensures the safety for the end users. The third part is the Pcell 30 components and mounting platform, including Pcell body, locking nuts, tungsten carbide pistons, liquid transmitting medium, anti-extrusion rings & disks, puck mounting sock, Pcell mounting puck, extraction tools and lubricating grease, as shown in Fig. 3.3.

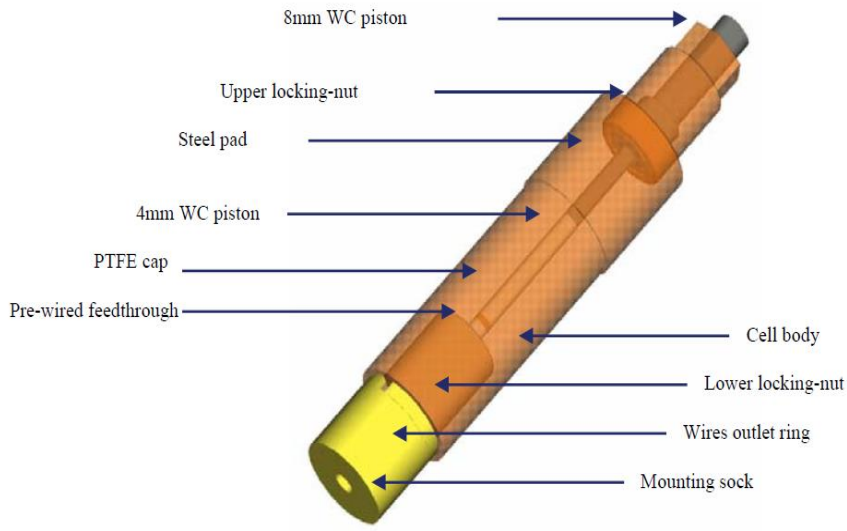

Figure 3.1. 3D modeling view of the Pcell 30.

Figure 3.2. EasyLab Ppress hydraulic press and its components.

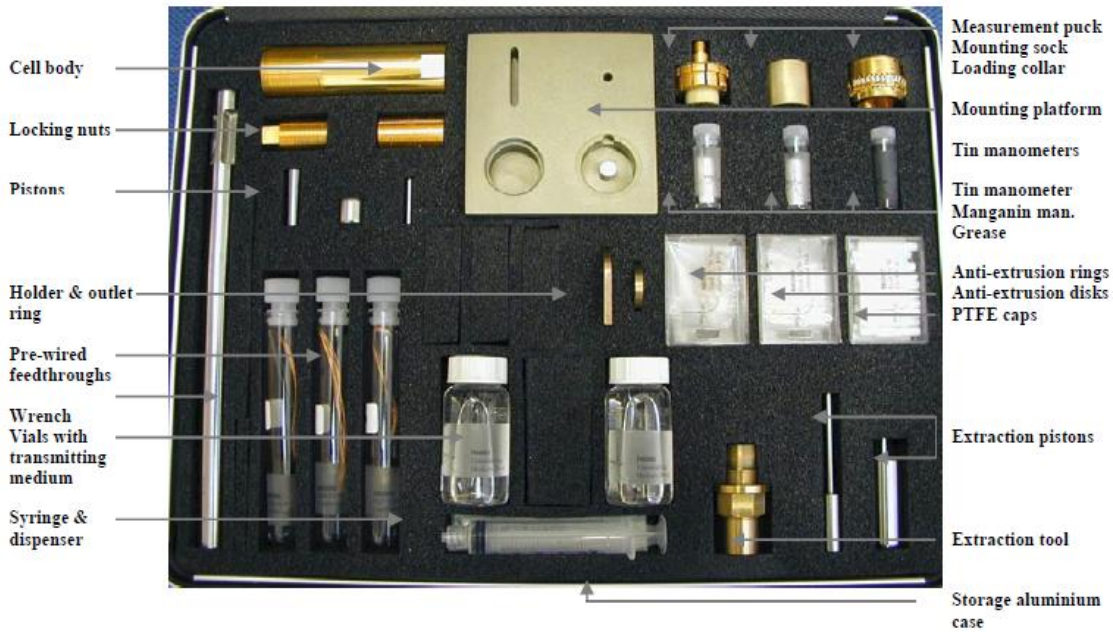

Figure 3.3. Pcell 30 components and mounting platform.

3.2 Brief steps of mounting process and applying pressure

These are highlighted and summarized important steps of mounting devices and applying pressure process. For full and detailed steps, please read throughout the user's manual and contact easyLab for assistance.

3.2.1 Setting up the lower part of the Pcell 30

For the safety and the successful application of pressure, ensure that the channel of the Pcell 30 body is clean from dust or remaining debris from previous measurements. Check that the anti-extrusion disk and ring can slide through the channel of the pressure cell. Using the syringe and dispenser, inject the pressure-transmitting medium into the PTFE cap by starting with the tip of the dispenser at the bottom and gradually raising it as the liquid is injected. It is important to avoid trapped air bubbles inside the PTFE cap at

this stage. If some bubbles appear, a gentle stir with the tip of the needle should dissipate them. Pentane & iso-pentane is composed of a very volatile medium. You should pay attention that when you insert the sample holder the liquid is overflowing. Ensure that air has not been trapped in the PTFE cap. Push the feedthrough inside the pressure cell channel as far as possible. Particular attention must be paid not to damage the delicate wires whilst sliding them through the locking-nut. A guiding tube can be used to help guiding the wires. Insert the wiring outlet ring (M02005) and screw into place the cell mounting sock (M02004). Wrap the protective tubing of the wires around the mounting sock (you can use some PTFE or Kapton tape in order to keep the tube into position). Screw the electrical connection puck (A05000) onto the mounting sock and connect the sample leads onto the gold-plated pads of Channel 1 as per the ACT option.

3.2.2 Setting up the upper part of the Pcell 30

On the circumference of the anti-extrusion disk, put a thin layer of lubricating grease and slide it inside the channel. Repeat the operation with the 4 mm WC piston (M02010). The presence of lubricating grease is important to reduce the friction force in particular at very high pressures above 20 kbar, as in the case of the Pcell 30. Sit the steel pad (P00016) on the top of the 4 mm WC piston and close the upper part of the pressure cell by tightening by hand the upper locking-nut. The hand tightening will allow identifying possible leakages inside the pressure cell. More than 2 full turns is likely to indicate that the PTFE cap is not leak tight. To test the device, open top of the protection

shield, plug the connection lead to the measurement puck. Connect the Lemo plug onto the PPMS testing station and the testing leads to a digital multimeter accordingly.

3.2.3 Applying pressure

The way the cell is pressurized is by the application a known force on a series of tungsten carbide pistons. In turn, the PTFE cap, where the sample is sitting surrounded by the transmitting medium, has its volume reduced and hence the pressure increases. This process is shown in Fig. 3.4.

Start by applying a small amount of force equivalent to 300 PSI of oil pressure, corresponding to a force of 0.3 ton. By using the 13 mm spanner (P00014), screw the upper locking nut through the opening of the interfacing sock whilst measuring the number of turns performed with the spanner (Note: There is no need to over-tighten the locking nut as this could damage the cell. In particular, at low pressures, you might run the risk of the cell turning inside its cradle). It is important to note the number of turns you are actually making in order to calculate the piston displacement inside the Pcell 30. The window opening has an angle enabling 1/6 (60 degrees) of a full rotation of the locking nut. Based on the geometry of this nut, one can calculate that one turn corresponds to an actual piston displacement of 0.166 mm. Increase the oil pressure by steps of 300 PSI and note the piston displacement by screwing the upper locknut for each applied force. Once the required applied force has been reached, tightly screw (without over tightening), the locking nut. Release the Ppress hydraulic press ram gradually down to 0 PSI. It is important to let the hydraulic ram release the pressure slowly to avoid any

undue mechanical stress during the release of the applied force onto the Pcell 30. It is recommended you leave the Pcell 30 for another 5 minutes on the Ppress to ensure that it has a good mechanical stability.

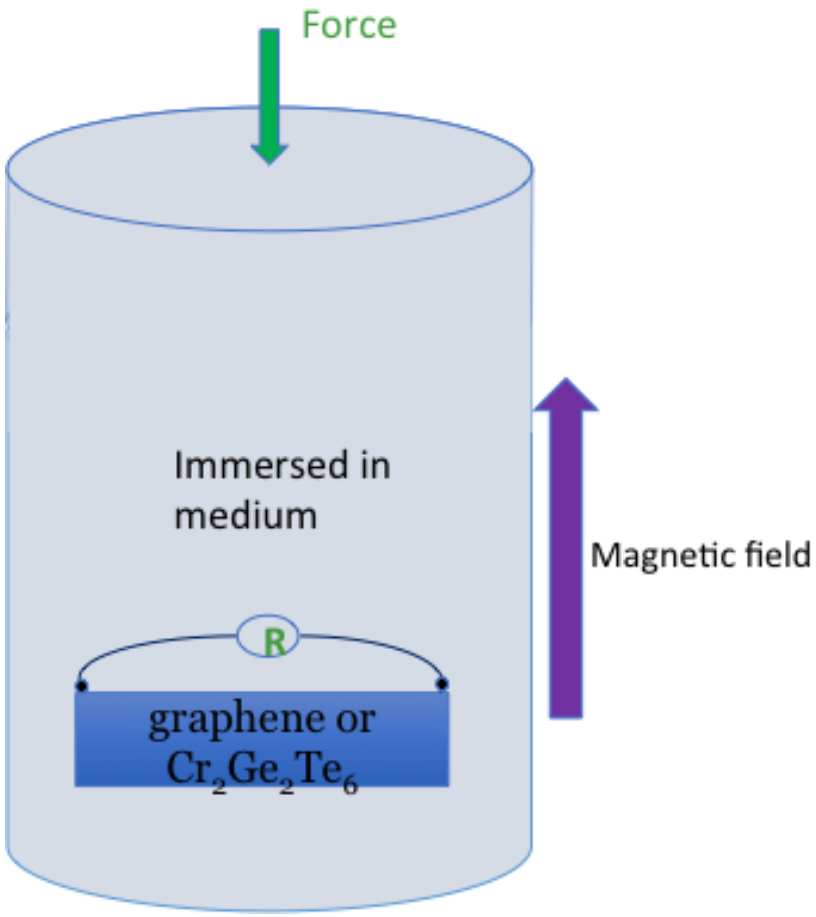

Figure 3.4. Schematic diagram to show the applying pressure process.

3.2.4 Decreasing the pressure

To decrease the pressure in the cell, set-up the Ppress as before. Particular attention should be paid to the vertical positioning of the Pcell onto the interfacing sock. Indeed, if the Pcell is lowered too much, the 8 mm piston will not have room to lower its position and you will not be able to decrease the pressure. A suitable starting value is to

position the top face of the upper locking nut half way through the sock's window. Increase smoothly and slowly the oil pressure and the applied force on the Pcell 30 until you reach the previous oil pressure. Then with the 13 mm spanner try to unscrew the upper locknut. If this cannot be done, then gradually increase the pressure until the upper locking nut has been freed. Once the upper locking nut has been freed, unscrew the locking nut by three to four complete turns. Then slowly release the hydraulic force until you have reached the target oil pressure. Re-tighten the upper locking nut (without over tightening). You can then slowly release the hydraulic ram as previously explained. Note: The exact control of the pressure is more difficult to achieve when releasing the pressure. This is largely due to the friction forces and associated backlashes, which may vary from set-up to set-up.

Chapter 4 Effects of pressure on the magnetic anisotropy of ferromagnetic insulator $Cr_2Ge_2Te_6$

Magnetoresistance of a $Cr_2Ge_2Te_6$ bulk crystal is measured under applied hydrostatic pressures up to 2 GPa. Upon the application of hydrostatic pressure, we observe an induced transition of easy axis from c axis to ab plane. Furthermore, we see a reduction of the bandgap of $Cr_2Ge_2Te_6$ by approximately 30% once the applied pressure reaches 2 GPa. We verify that the MR change originates from anisotropic magnetoresistance by measuring the temperature dependence of MR below and above Curie temperature under different applied pressures. The application of hydrostatic pressure on van der Waals layered materials is expected to serve as a unique and powerful technique to fine tune the interlayer spacing, which could strongly affect its magnetic and electronic properties.

Layered ferromagnets are interesting materials among the van der Waals (vdW) material family. Recently, there has been great interest in exploring 2D crystals with intrinsic magnetism which break the Mermin-Wagner theorem[82] due to its magnetic anisotropy. The intrinsic magnetism of CGT was shown in a recent report by Gong et al. to remain down to the monolayer limit, and Huang et al. demonstrated that monolayer chromium triiodide (CrI_3) is an Ising ferromagnet with out-of-plane spin orientation.[45,50] These materials provide great opportunities for van der Waals engineering their novel interface phenomena and opens up new possibilities for applications such as ultra-compact spintronics. Applying pressure on materials is a clean and efficient method to

study its physical properties without introducing impurities or other uncontrollable variables. The data can be collected in one sample by applying different pressures as opposed to doping and avoiding the possibility of variations between different samples. An applied pressure will induce a change in the distance between atoms, which alters the interactions between atoms, and thus change the macroscopic properties of the material. The lattice constant will reduce in proportion to the compressibility; hence the volume of the crystal can be varied. This is even more interesting in the case of vdW materials as the layers are weakly bonded to one another and thus pressure can have the effect of increasing the interlayer interaction of the material. The intrinsic parameters such as the Curie temperature Tc,[83] the saturation magnetization Ms[84] and the cubic magnetocrystalline constant K_1[85] can be expressed as a function of the volume under an applied hydrostatic pressure on the investigated sample. The atomically-layered 2D ferromagnetic insulator CGT[38] is an interesting material to investigate its physical properties which strongly depend on the interactions between atoms. The electronic structures of TMD and graphene have been found to be very sensitive to applied pressure,[86-88] motivated by the same vdW nature of layered materials, so it would be interesting to study the evolution of both the electronic and magnetic properties of CGT under an applied hydrostatic pressure.

4.1 Sample information and measurement setup

We use single crystalline CGT, which is synthesized by the flux method.[89,90] Our CGT sample is cleaved via scotch tape to a size of approximately 2 mm×1 mm×0.01 mm. Indium is applied to the ends of the CGT sample and then connected to gold wires to

perform the MR measurements. The gold wires are then connected to the feedthrough wires using indium. To avoid the electrical short problem between wires, the gold wire to feedthrough wire connection area is coated with epoxy (Permatex PermaPoxy) and left in ambient atmosphere for at least 24 h to be fully cured. The sample is then measured inside a high-pressure cell module (Almax easyLab Pcell 30) assembled with a physical property measurement system. The sample is immersed in the medium of pentane & iso-pentane with mix ratio of 1:1. To protect the sample from reacting with the medium, one layer of PMMA is coated on the sample.

Fig. 4.1 is an illustration of the crystal structure of CGT. The interlayer distance is about 7 Å and the in plane interatomic distances are as followings: Te-Te: 0.377 nm, Cr-Te: 0.2749 nm, Cr-Cr: 0.39420(5) nm, Ge-Te: 0.3876(7) nm or 0.2578(4) nm and Ge-Ge: 0.24592(6) nm. The bulk CGT has a relatively high Curie temperature of ~ 61 K and a band gap of ~ 0.2 eV.[38] The magnetism is carried by the chromium (Cr) atoms with each atom carrying about 2.23 μ_B. This value is slightly lower than the theoretical value of high spin configuration state of Cr^{3+} (3 μ_B /Cr atom), which might be the results of some nonmagnetic impurities in the sample. Due to its weak vdW attraction between layers, it can be exfoliated down to a few layers or even monolayer.

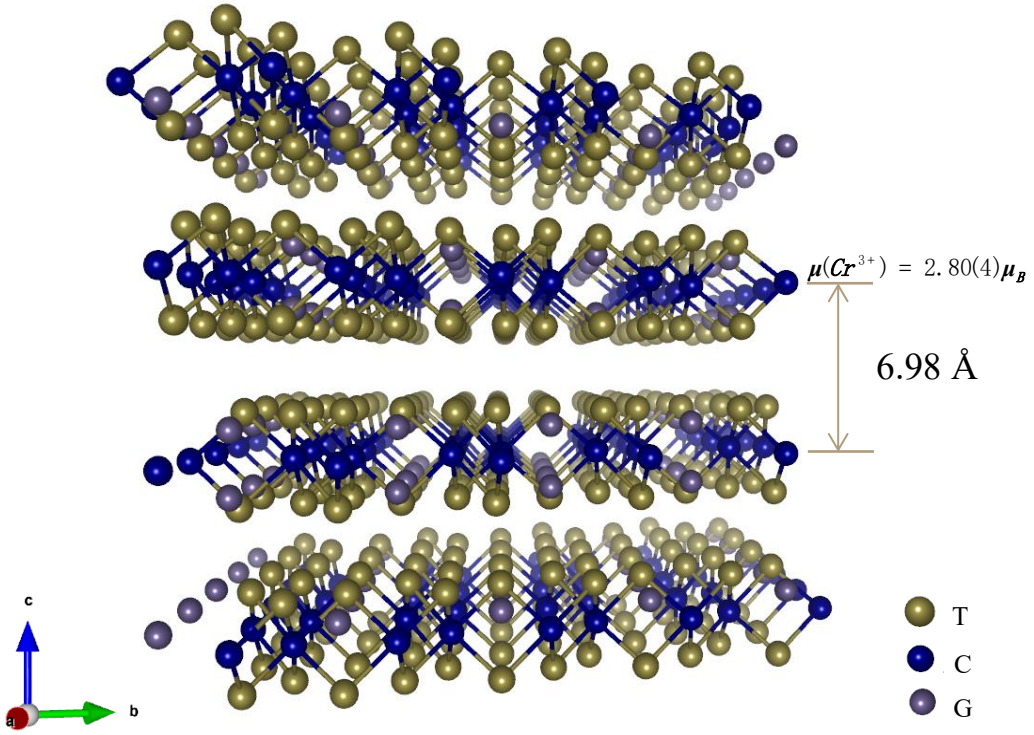

Figure 4.1. Crystal structure of CGT from side view. [Xing, Wenyu, *et al.* "Electric field effect in multilayer Cr2Ge2Te6: a ferromagnetic 2D material." *2D Materials* **4.2** (2017).]

Fig. 4.2 (a) is the magnetic-field-dependent magnetization measured at 5K when magnetic field is parallel to c-axis and along ab plane. The saturation field along c axis is smaller than along ab plane, indicating the easy axis is along c axis. From our measurements, we conclude that the saturation field $4\pi M_{eff}$ is about 0.5 T. The lack of detectable remnant magnetization indicates the soft ferromagnetic nature in CGT.[91] The MR of magnetic field along ab plane has a clear AMR feature while MR of magnetic field along c axis has no observable AMR feature, as shown in Fig. 4.2 (b). Since the

easy axis is along c axis, there is magnetic moment rotation from c axis to magnetic field in ab plane during the process of increasing magnetic field in plane, resulting in the AMR. For magnetic field along c axis, though there maybe magnetic moments flipping from antiparallel to parallel to magnetic field direction, the resistance doesn't change, hence there is no observable AMR feature. This is another evidence that easy axis is along c axis.

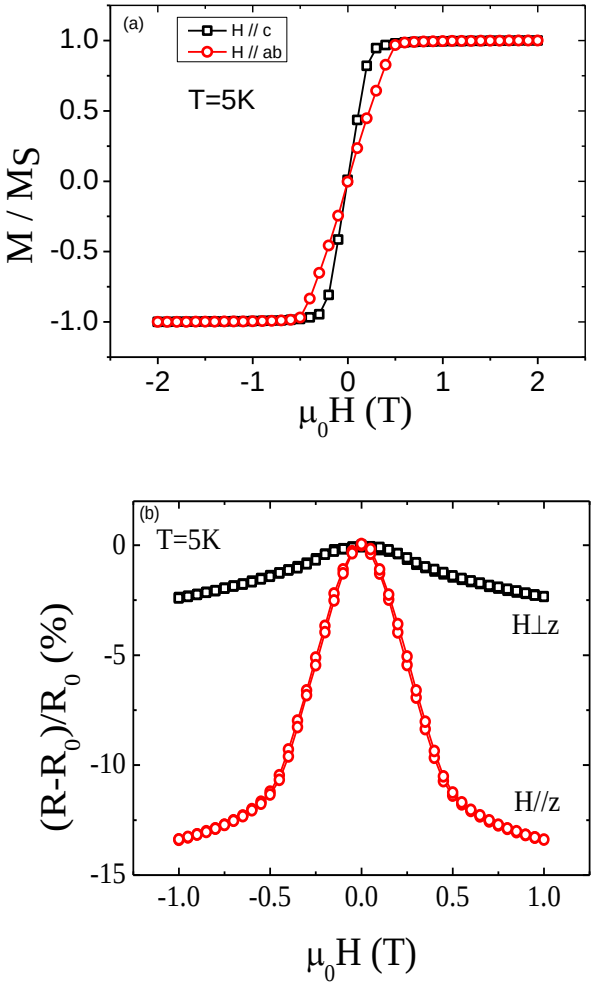

Figure 4.2. Magnetic properties at zero pressure. (a) Magnetic-field-dependent magnetization measured at 5K when magnetic field is parallel to c-axis and along ab plane. (b) MR when field is c axis and along ab plane.

4.2 Reduced band gap under pressure

The electrical transport properties of CGT are characterized by measuring the temperature dependence of resistance under zero and 2 GPa pressure from 300 K to 100 K, as shown in Fig. 4.3. At zero applied pressure, as the temperature decreases, the sample's resistance increases monotonically, which is consistent with the semiconductor properties of CGT. At 100K, the resistance under zero pressure is about 20 times larger than the resistance under 2 GPa pressure. The difference becomes even larger as we lower the temperature: at 70K, the resistance under zero pressure is about 40 times larger than the resistance under 2 GPa pressure; at 15 K, this ratio goes up to 375. The resistance can be fitted with the thermal activation model with a constant energy band gap E_g, as described by $R = R_0 \exp(\frac{E_g}{2k_B T})$, where k_B is the Boltzmann constant and T is the temperature. The reason to fit in the 300 K to 100 K temperature range is that the lnR vs 1/T deviates from the linear behavior below 100 K. From the exponential fits, we obtain a band gap of 0.19 eV under zero pressure, which agrees with the theoretical value of about 0.2 eV.[92] Under 2 GPa, the band gap is reduced by 0.066 eV, to 0.124 eV. This pressure induced decrease of band gap is similar to the previous report of hydrostatic pressure on black phosphorus,[93] which is due to the fact that direct band gap is mainly determined by the out-of-plane pz-like orbital of phosphorus and further reduced by the interlayer coupling in the bulk crystal. Thus, the pressure-induced strengthen of interlayer coupling can reduce the direct band gap of black phosphorus.

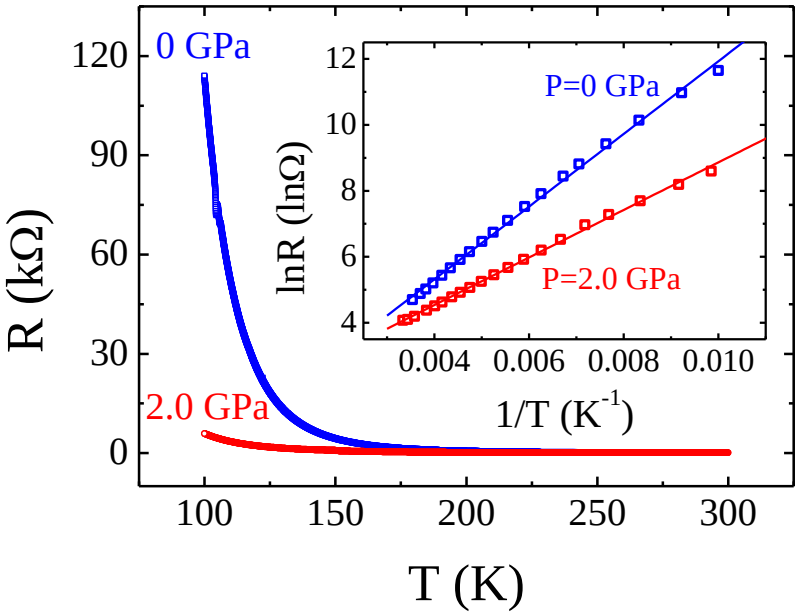

Figure 4.3. Temperature dependence of resistance under zero pressure and 2 GPa. Inset is the linear fitting of lnR vs 1/T under zero pressure and 2 GPa.

4.3 MR under different pressures

In conducting ferromagnets, the electrical transport properties show anisotropy between the states of magnetization parallel to and perpendicular to the current direction. For the AMR measurement under different pressures, the external field is perpendicular to the sample plane. Fig. 4.4 summarizes the anisotropic magnetoresistance (AMR) at 15K under zero pressure and 2 GPa pressure. At zero pressure, there is no observable AMR because the easy axis is along the c axis, and thus the external field along the c axis would not rotate the direction of magnetic moment. At zero pressure, the M vs. H data shows the net magnetic moment to be zero at H=0, suggesting the magnetic structure are multidomain structure. If we neglect the domain wall scattering, when the external field

is larger than the saturation field, all the domains will point in the same direction as the external field. But in this process, resistance is an even function of the direction of M parallel to H and M antiparallel to H states, so the resistance will not change. The MR signal at zero pressure is only magnetic field-dependent, and it does not saturate above Ms and continues to decrease with the applied magnetic field. At zero pressure, from the angle rotation data, we know $\rho_{\perp}$ (M perpendicular to the current) is larger than the in-plane resistance $\rho_{//}$ (M partially parallel to the current). As the pressure is increased up to 2 GPa, there is a clear presence of AMR signal. This means at this pressure an increasing magnetic field will rotate the magnetization, indicating the easy axis of CGT changes from c axis to ab plane upon 2 GPa pressure applied. There are two components in the MR data. The first part is magnetic-field dependent and it does not saturate above Ms. The second part is the AMR, which is related to the orientation of the magnetic moment, and saturates above Ms. There may be domains in-plane, and domains can point to several orientations along equivalent crystallographic directions. When the magnetic field is applied, the in plane spins begin to rotate to the direction of the applied magnetic field along c axis. Similar behavior is also observed at 50 K, which is close to the Curie temperature. The difference is the saturation field at 50 K is much smaller than 15 K.

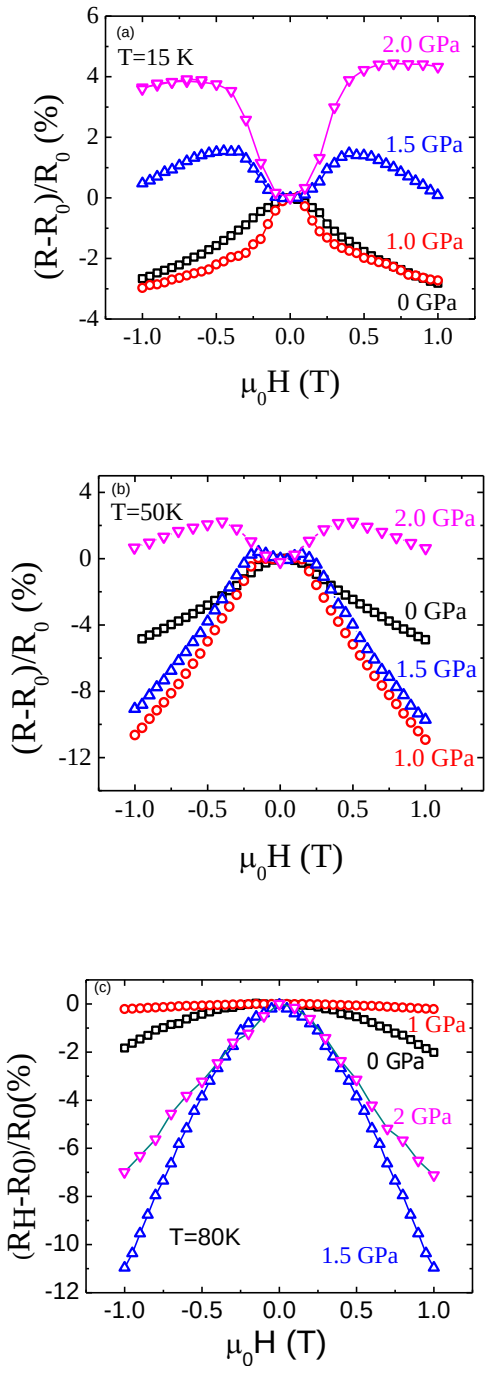

Figure 4.4. MR at different pressures. (a) Comparison of MR at 15 K under zero pressure, 1 GPa, 1.5 GPa and 2 GPa at 15 K. (b) Comparison of MR at 50 K under zero pressure, 1 GPa, 1.5 GPa and 2 GPa. (c) Comparison of MR at 80 K under zero pressure, 1 GPa, 1.5 GPa and 2 GPa.

4.4 Temperature dependence of MR

Fig. 4.5 shows the temperature dependence of AMR under the pressure of 2 GPa. With temperature approaching Curie temperature, AMR decreases. However, at 50K, which is close to the Curie temperature, AMR is still very clear. While at 60K or above, the AMR cannot be observed. The signal at this temperature and higher temperature is only due to the magnetic field-dependent background MR, showing the MR is consistent with the AMR nature.

In summary, we successfully employed the technique of applying large hydrostatic pressures up to 2 GPa to a bulk crystal of CGT and observed a reduction of its band gap and a transition of easy axis from c axis to ab plane by fine tuning its interlayer distance. This opens up new possibilities for exploring new magnetism in the atomically layered material by applying pressure. From the heterostructure point of view, it will also benefit the proximity effect by bringing the material closer to the substrates such as in the graphene/magnetic insulator[24] and graphene/TMD structures.[22]

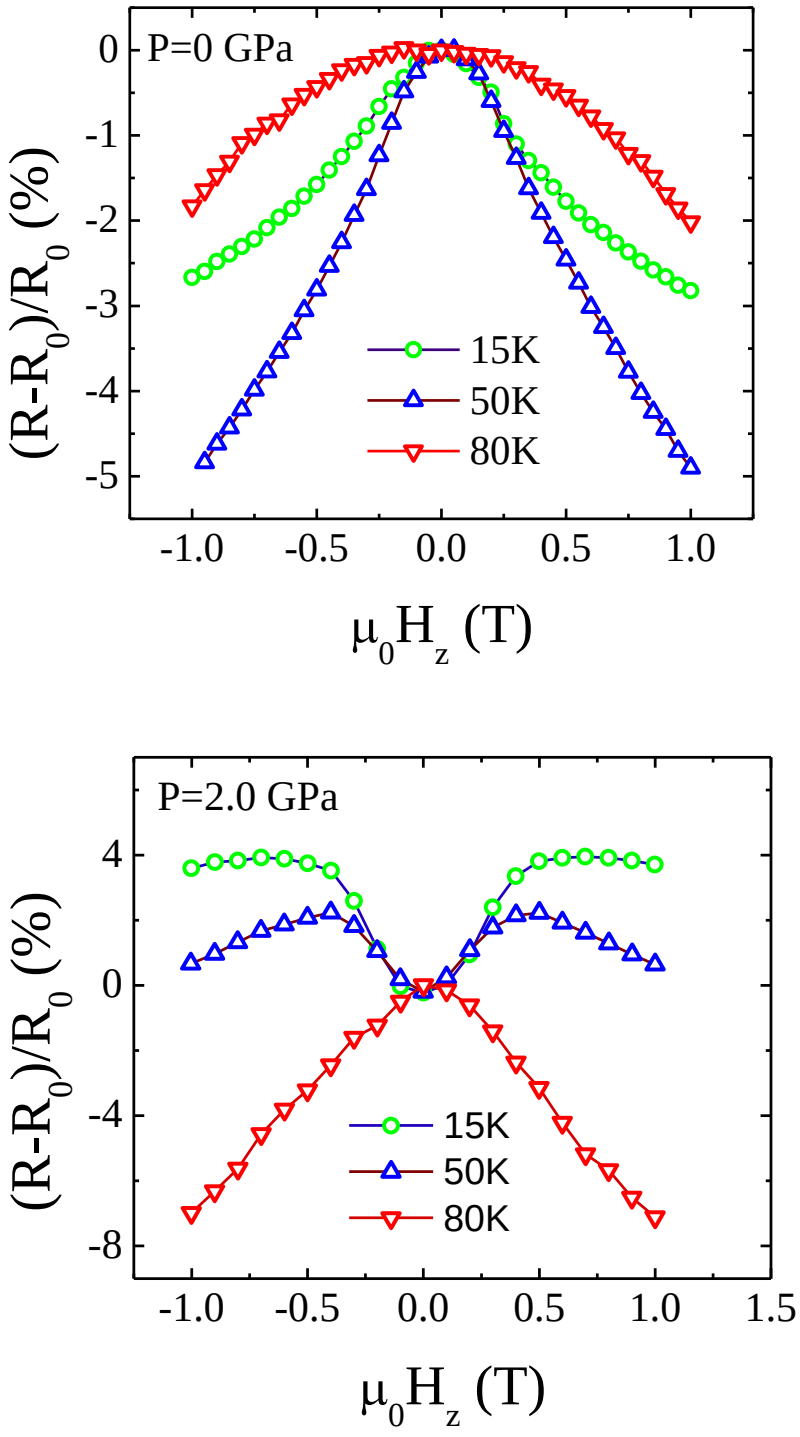

Figure. 4.5. Temperature dependence of MR under zero pressure and 2 GPa.

Chapter 5 Pressure effects on graphene/WSe_2 device

Electrical spin injection.[73,95,96] is a necessary condition for graphene spintronics.[94] Graphene has extraordinary high mobility and small SOC, which is favored in charge and spin transport efficiency. But lacking a band gap hinders the applications in the transistors (cannot be switch off). For TMD, the breaking of inversion symmetry together with high intrinsic SOC originated from the d orbitals of the heavy metal atoms[29] leads to the spin-valley coupling at the valence-band edges.[28] As a result, their band structure[97] allows for a valley-resolved optical spin excitation by circularly polarized light.[28,30,31] In addition, the Fermi level can be tuned by a transverse electric field perpendicular to the layered plane to cross the TMD's conduction band, creating a system of coupled massless Dirac electrons and conventional 2D electron gas[98] in graphene/TMD heterostructure. Combining the gate tunability and high mobility of graphene with the strong SOC and optical properties of 2D TMD provides a good platform to study interesting and unique physics and the potential application in optoelectronics.

5.1 Introduction of WAL and WL in graphene

5.1.1 The effects of scattering in graphene on MR

The quantum correction to the conductivity of 2D systems due to electron interference has been studied for a long time. This phenomenon of WL has become a tool to determine the processes responsible for electron dephasing due to inelastic electron scattering or scattering by magnetic impurities.[99]

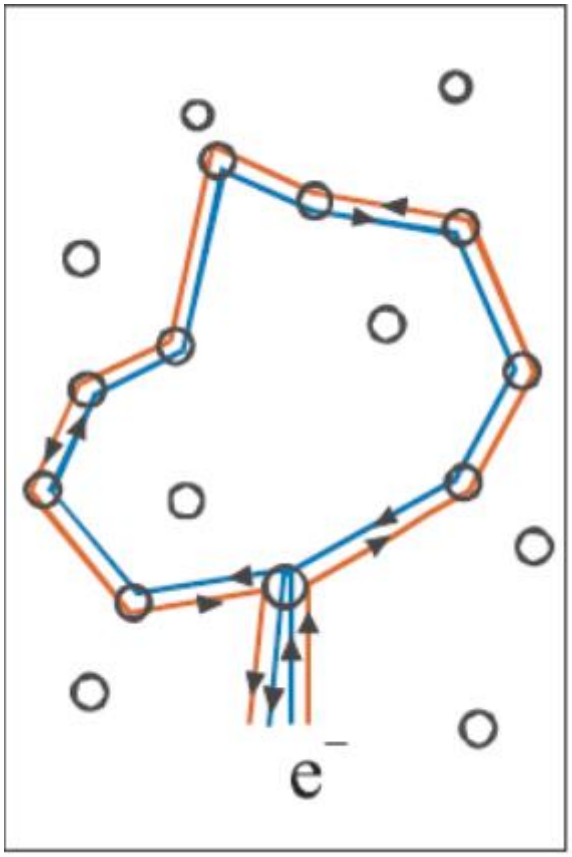

Figure 5.1. Phase coherence process. The trajectories of an electron scattered by impurities that give rise to a quantum correction to the conductance. [Tikhonenko, F. V., *et al*. "Transition between electron localization and antilocalization in graphene." *Physical Review Letters* **103** (2009).]

Fig. 5.1 shows how an electron scattered by impurities can interfere on a closed trajectory when it is treated as a wave. To understand the concept of phase interference in graphene, let us start with the quantum corrections in conventional 2D systems. Two electron waves propagate in opposite direction around the trajectory and interfere at the point of intercept. If the two paths are identical, the phase of the two waves are the same and the interference is constructive, resulting in the increase of the probability for electrons to scatter back and the decrease in electrical conductance compared with its classical Drude model value. By applying a magnetic field perpendicular to the 2D

system, we add a phase difference to the two waves and destroy the interference. This results in an increase of the conductance compared with the conductance at zero magnetic field - positive magnetoconductance (MC). In graphene, the unique Berry's phase π of the pseudospin adds a phase difference to the two interfering trajectories,[100] so that they meet in anti-phase and destructive interference occurs. This should result in an increase of the conductance due to quantum interference compared with the Drude model value and a negative magnetoconductance.[101] This WAL effect is very different from that observed before in 2D systems with strong SOC where the two waves meet in antiphase because of spin flips in scattering by impurities since the SOC in graphene is known to be weak due to the low mass of carbon atoms.[102]

In graphene, WL does not follow the standard convention that it is only controlled by inelastic and spin-flip processes. The quantum correction depends not only on the dephasing time τ_φ but on elastic scattering times τ_i and τ_*.[103] Charge in graphene are chiral, that is, they have an additional quantum number (pseudospin). Graphene's band has two valleys, and quantum interference of electrons in one valley can be suppressed by scattering on the defects with the size of the lattice spacing, as well as dislocations and ripples. Such defects produce an effective random magnetic field which destroys the interference. The combined effect of this intravalley scattering is characterized by the time τ_*. Elastic scattering that breaks the chirality, resulting in the suppression WAL. Another elastic scattering process called intervalley scattering will restore the suppressed interference. Intervalley scattering by sharp defects (such as the edges of the sample) that are able to scatter electrons between the two valleys is characterized by the time τ_i. As the

two valleys have opposite chirality and warping, intervalley scattering is expected to negate the chirality breaking and warping effects by allowing interference of carriers from different valleys.[100,101,103] So it restores the WL in graphene as the conventional WL in 2D system. While small τ_* suppresses interference within a valley, small enough τ_i restores it by mixing the two valleys, which have opposite chirality. In graphene, the intervalley is strong and the intervalley scattering time is shorter than the dephasing time, the quantum correction to the conductivity has the WL sign.

The WL and WAL in single layer graphene can be expressed in following equation[101]: $\Delta\sigma(B) = \frac{e^2}{\pi h}\left[F\left(\frac{B}{B_\varphi}\right) - F\left(\frac{B}{B_\varphi+2B_i}\right) - 2F\left(\frac{B}{B_\varphi+B_*}\right)\right]$ Eq. (5.1)

In bilayer graphene, the equation is as following equation:

$$\Delta\sigma(B) = \frac{e^2}{\pi h}\left[F\left(\frac{B}{B_\varphi}\right) - F\left(\frac{B}{B_\varphi + 2B_i}\right) + 2F\left(\frac{B}{B_\varphi + B_*}\right)\right] \quad \text{Eq. (5.2)}$$

Here $F(z) = \ln(z) + \psi\left(\frac{1}{2}+\frac{1}{z}\right)$, $\psi\,(x)$ is the digamma function, $\tau_{\varphi,i,*}^{-1} = \frac{4De}{\hbar}B_{\varphi,i,*}$, τ_φ^{-1} is the dephasing rate and D is the diffusion coefficient. The theory assumes that the momentum scattering rate τ_p^{-1} is the highest in the system and comes from charged impurities, and does not affect the electron interference. In the absence of intravalley and intervalley scattering in a defect-free graphene layer, $\tau_{i,*} \to \infty$, $\Delta\sigma$(B) is totally controlled by the third term. Negative MC corresponding to the weak antilocalization. In the opposite case of strong intravalley and intervalley scattering (small τ_i and τ_*), both negative terms are suppressed and the first (positive) term dominates, which corresponds to WL.

5.1.2 Temperature and carrier density dependence of MR

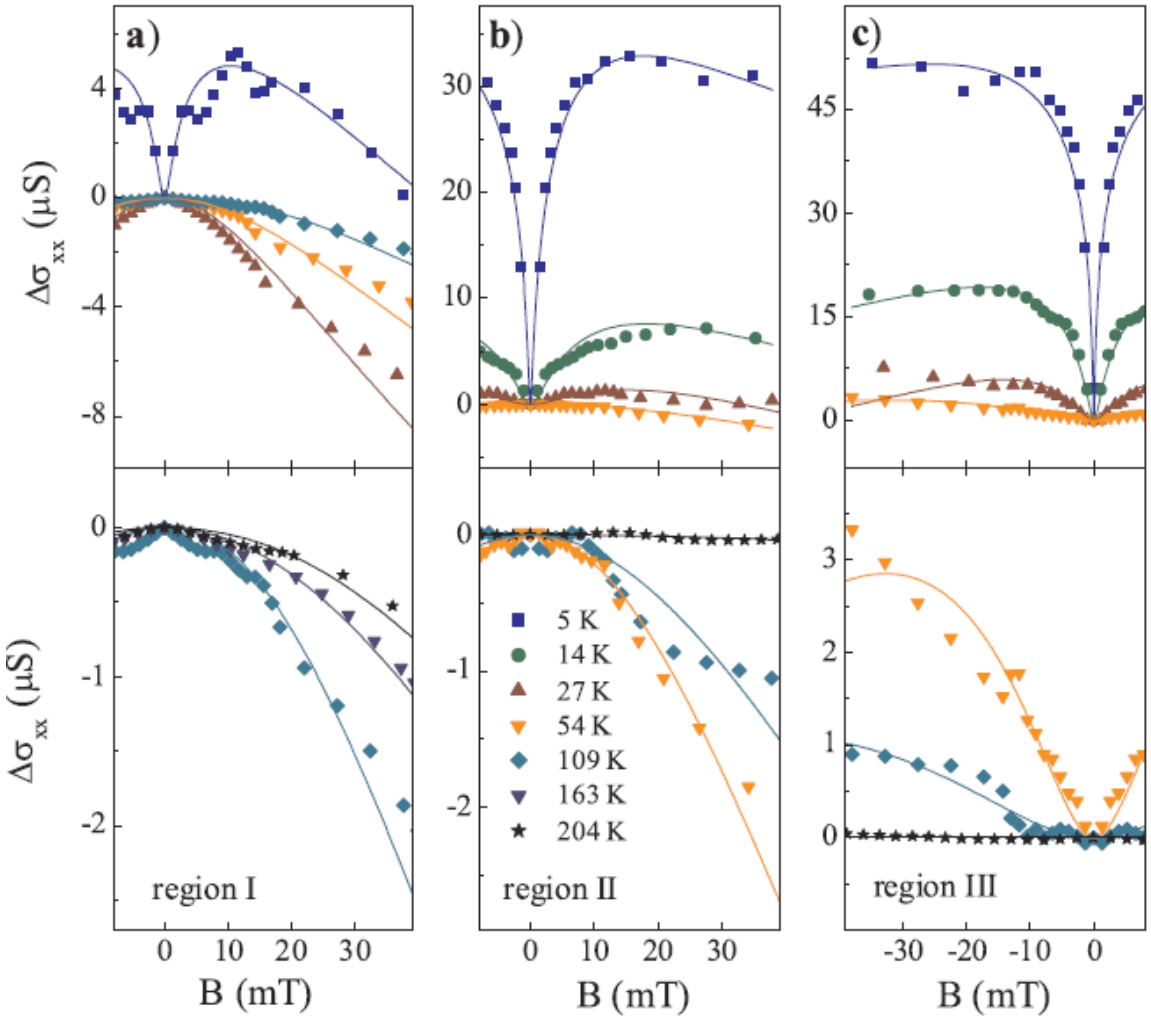

Figure 5.2. Temperature and carrier density dependence of MR. (a), (b), (c) Evolution of MR with increasing temperature in three different carrier density regions. The density in I, II and III are about $2.5\times10^{11}\,cm^{-2}$, $1\times10^{12}\,cm^{-2}$ and $2.2\times10^{12}\,cm^{-2}$. [Tikhonenko, F. V., *et al*. "Transition between electron localization and antilocalization in graphene." *Phys Rev Lett* **103** (2009)]

The width of the dip in small B is mainly controlled by τ_φ, while the bending of the curve at larger B is determined by τ_i and τ_*. Elastic times τ_i and τ_* are essentially temperature independent but inelastic time τ_φ strongly decreases with increasing temperature. The intervalley scattering is stronger at high carrier density. The favorable

conditions for the observation of negative MC (WAL) are small ratios τ_φ / τ_* and τ_φ / τ_i. This can be realized by increasing the temperature (which decreases τ_φ) and by lowering the carrier density (which increases τ_i). There is a transition from WL to WAL at some temperature around 14~27K depending on the carrier density because dephasing time decreases and it becomes smaller than the intervalley scattering time. The WAL width continues to increase with increasing T, until at T ~ 200K the dependence becomes flat again when antilocalization disappears due to rapid dephasing of the electron trajectories. This temperature is much higher than the disappearance temperature of quantum correction in conventional 2D systems, which is due to intensive electron-phonon scattering.[104] In graphene, however, electron-phonon scattering is expected to be weak.[105,106] When approaching Dirac point, the electron-electron interaction is enhanced,[103] resulting in the increase in the dephasing rate. Therefore, the WAL peaks simultaneously weaken and broaden before they finally flatten out when the dephasing rate exceeds the spin relaxation rate near the Dirac point.

5.1.3 SOC effects on the WAL and WL in single layer and bilayer grapheme

When the SOI is introduced, Eq. 5.1 is modified by replacing $B_{i,*}$ with Rashba SOC term B_R and total SOC term B_{soc} assuming the SOC scattering rate is much stronger than the intervalley and intravalley scattering rate.

$$\Delta\sigma(B) = -\frac{e^2}{2\pi h}\left[F\left(\frac{B}{B_\varphi}\right) - F\left(\frac{B}{B_\varphi+2B_R}\right) - 2F\left(\frac{B}{B_\varphi+B_{SOC}}\right)\right], \qquad \text{Eq. (5.3)}$$

$$B_{\varphi,R,SOC} = \frac{\hbar}{4De}\,\tau_{\varphi,R,SOC}^{-1}, \qquad \tau_{SOC}^{-1} = \tau_R^{-1} + \tau_{KM}^{-1}$$

The spin relaxation rates τ_R^{-1} and τ_{KM}^{-1} due to Rashba SOC and Kane Mele type SOC are related to the momentum scattering rate τ_p^{-1} by $\tau_R^{-1} = 2\frac{\lambda_R^2}{\hbar^2}$ [107]and $\tau_{KM}^{-1} = 2\frac{\lambda_I^2}{\hbar^2}\tau_p$.[108]

If a strong Rashba SOC is introduced, graphene acquires an additional π phase in the wave-function, resulting in destructive interference and WAL to emerge.[109] At the lowest temperatures, the SOC leads to WAL, as in the typical case, but only if graphene has broken z → -z symmetry, due to a substrate or deposits, which is the Rashba type SOC. In contrast, for a z → -z symmetric system, which is Kane Mele type SOC, SOC leads only to a saturation in the size of the WL correction rather than WAL. If Rashba SOC is present, it tends to induce WAL in both monolayer and bilayers - as in semiconductors and metals – but, if intrinsic SOC prevails, it results in a suppression of weak localization. Bilayer has Berry's phase 2π. The intrinsic term tends to suppress WL. As in the monolayer, when the Rashba term is neglected, the influence of the intrinsic SOC may be absorbed into a modified definition of the inelastic dephasing rate as $\tau_\varphi^{-1} \rightarrow \tau_\varphi^{-1} + \tau_{KM}^{-1}$, it suppresses WL, mimicking saturation of the dephasing time. Unlike monolayer graphene, however, chiral quasiparticles produce WL in bilayers, and no crossover to WAL is visible, even when the combined effective dephasing rate $\tau_\varphi^{-1} + \tau_{KM}^{-1}$ is relatively large. The Rashba term tends to drive WL towards WAL as in conventional materials and monolayer graphene. In conclusion, in the absence of symmetry breaking, $\tau_\varphi << \tau_*, \tau_i$, the chirality of electrons in monolayer and bilayer graphene would be manifest as WAL and WL behavior, respectively.

However, in typical graphene samples, sources of symmetry breaking including trigonal warping, random-bond disorder (due to bending of graphene sheet) and

dislocation/antidislocation pairs will tend to suppress WL (in the regime $\tau_* << \tau_\varphi << \tau_i$), so that weak localization can only be observed in the presence of strong intervalley scattering, $\tau_i << \tau_\varphi$. At low temperature, WL in graphene may be sensitive to the presence and nature of SOC, resulting in WAL-as in semiconductors and metals-in both monolayer and bilayers if the SOC is of the Rashba type, $\tau_{BR} << \tau_\varphi$. This would be distinguishable from the presence of intrinsic SOC, which would lead to suppressed weak localization once $\tau_{KM} << \tau_\varphi$. In conclusion, WL and WAL serve as sensitive probe to different kinds of scattering and SOC at low temperatures.

5.2 Vdw heterostructures

Building heterostructures of different 2D materials is an effective approach to incorporate exceptional properties due to proximity effects. For examples, it has been experimentally demonstrated that graphene on TMDs can serve as a new platform for optospintronics.[98] Owing to the much smaller Fermi level fluctuations[110] than single layer graphene, bilayer graphene allows a more precise (sub meV) control of chemical potential.

There have been intensive efforts to enhance the SOC by decorating graphene with adatoms, which is predicted by Kane and Mele[52] as a precursor of topological insulators.[111-113] Though the approach is promising, vdW heterostructures provide more robust control in the view of technological reproducibility of devices. Graphene on WSe_2 is a special case due to the predicted band inversion that was proposed to lead to novel topological properties.[114]

5.3 Device fabrication process

Step 1: A polydimethylsiloxane (PDMS) stamp is placed on a glass slide and treated with O_2 plasma in an inductively coupled plasma (ICP) chamber with 200 W for 2 minutes. Then, the stamp is coated with 15% polypropylene carbonate (PCC) dissolved in anisole and baked on a hot plate at 90 °C for 5 minutes.

Step 2: A flat piece of WSe_2 which has been exfoliated on a p-Si/SiO_2 wafer is first located via optical microscopy and then the wafer is placed on the adhesive surface of our material transfer stage. The glass slide with PDMS/PPC is placed, polymer side facing down, in a micromanipulator above the transfer stage. The micromanipulator is then lowered until the PCC comes into contact with the WSe_2 flake. The temperature of the transfer stage is then raised to above 60 °C to soften the PPC film so that it anchors to the WSe_2 flake. The stage is then cooled down, and, once the temperature is below 45 °C, the micromanipulator is raised quickly such that the PDMS/PCC layer is no longer in contact with the SiO_2 substrate. The desired WSe_2 flake will be picked up with the PCC in this step with a yield greater than 95%.

Step 3: The p-Si/SiO_2 wafer that contained the WSe_2 flake is removed from the transfer stage and replaced with a p-Si/SiO_2 wafer containing a previously mechanically exfoliated bi-layer graphene flake. We mainly employed optical contrast based on the pixel RGB value to index the number of layers in a flake[46] and confirmed the number of layers by Raman. The glass slide with the PDMS/PPC/WSe_2 stack is then positioned such that the WSe_2 is directly above the graphene flake. The material transfer stage can then be

rotated until the graphene flake is in the desired position for transferring the WSe_2 flake. The stage temperature is raised to above 110 °C and then the PDMS/PPC/WSe_2 stack is lowered slowly until it is in complete contact with the graphene flake. The glass slide is then retracted. The PDMS/PPC comes up with the slide leaving behind the WSe_2.

Step 4: Once the desired WSe_2/graphene heterostructure has been formed the device is etched with O_2 in the ICP chamber to remove the parts that do not contain bi-layer graphene. The contacts to the device are then patterned with electron beam lithography and 50 nm of Au is deposited via electron beam evaporation to the exposed graphene.

Step 5: To protect the WSe_2 from degradation due to air exposure and the device from the pressure cell medium, a flake of h-BN is transferred on top of the device. For this step h-BN is exfoliated onto a glass slide that has a strip of tape that is coated elevacite acrylic resin 2550 that is dissolved in methyl isobutyl ketone. The device on the p-Si/SiO_2 wafer is put back onto the material transfer stage and the desired h-BN flake on the glass slide is positioned on the micromanipulator above the device. The glass slide is then lowered until the h-BN flake is brought into contact with the device. The stage is then heated to 70 °C and then the glass slide is retracted. When the glass slide losses contact with the device, the h-BN flake along with the polymer layer is left behind. The device is then put into an acetone bath and rinsed with IPA to remove the polymer before measurement.

These procedures can be concluded in Fig. 5.3, the final heterostucture is BN/WSe_2/BLG/SiO_2 (from up to bottom).

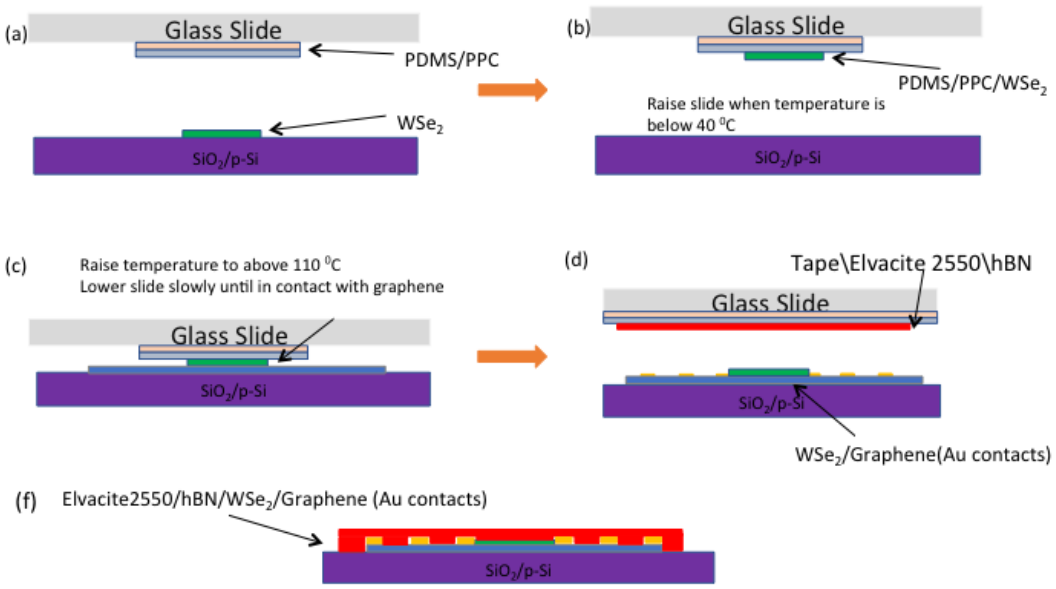

Figure 5.3. Steps of building BN/WSe_2/BLG/SiO_2 heterostructures (from up to bottom).

5.4 Mounting on the pressure cell

For study of pressure effects on graphene devices, one big flake of BN is transferred on top to protect from reacting with medium. The medium used here is mixture of pentane and iso-pentane with ratio 1:1. It is composed of a very volatile medium. Particular attention is needed when you insert the sample holder, ensuring that the liquid is overflowing. Ensure that air has not been trapped in the PTFE cap. When the device is ready, it cutted into a small size because of the limited space of the PTFE cap with inner diameter of 2.9 mm and it will deform inwardly reducing its inner diameter by approximately 0.1 mm. Therefore, it is recommended to have sample with a maximum section size of 1.5 mm to avoid any damage to it. Each feedthrough comes with twisted pair of 0.1 mm copper wires. Two manometers (room temperature-manganin and low temperature-tin) are mounted as standard in 4 wires configuration. The remaining two

pairs, are used for the sample connection. But we made some modifications of the feedthrough. Firstly, the manometers are removed to save space for more connections to the graphene devices. For four-terminal resistance measurement, we need at least six connections, four for resistance measurement, one more for hall measurement and the last one for gating of the device. Because of the difficulties of connection, we hope to have as more connections as possible. If one of them is not good, we don't have to take out the device and remount it. Not only because it is very time consuming but also it is dangerous because that device could break down due to its fragility to the static charge. The most difficult part is the connections to the graphene device. The connections should be robust to the medium environment and pressure up to 2 GPa. The user-friendly wire bonder cannot be used here. The connections are done by hand with silver epoxy under microscope. Extreme patience and caution is needed to have good connections and avoid the shorts between two electrodes. Here thin insulating wires are used to prevent the shorting problem between wires. For the insulating wires, only the head of the wire is conducting while the body is coated with some insulating material. The challenge is how to make good connections between the insulating wire and the feedthrough wire with very small contact area. We have tried three materials, silver epoxy, silver paint and indium. Usually, silver epoxy is good conducting material but it needs baking. High power heat lamp is used to bake the silver epoxy. Silver paint is also an option but it is not stable in the medium and cannot tolerate high pressure. The best choice is indium, which is conducting and strong enough. After that, the insulating wire-to-feedthrough

wire connection area will be coated with some epoxy or torr seal to enhance mechanical strength and for better insulation between wires.

5.5 Graphene under high pressure

5.5.1 Device structure

Let us first look at the device schematic diagram to have a better understanding of the shifting of the Dirac point. Fig. 5.4 shows the device heterostructure BN/WSe_2/bilayer graphene/SiO2 from bottom to up.

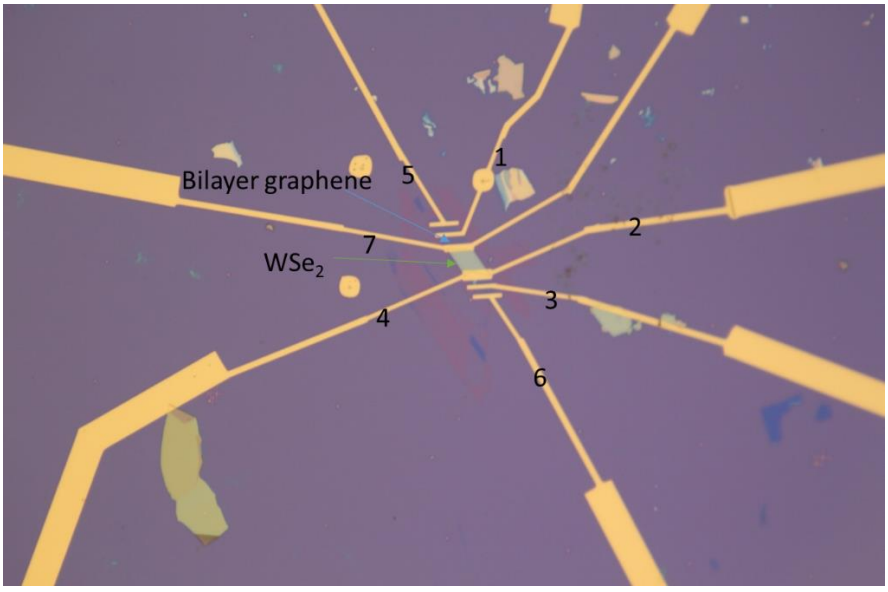

Figure 5.4. Optical image of WSe_2/graphene device on SiO_2 substrate. The magnification is 200 and a large flake of BN will be transferred on the device to protect reaction with medium.

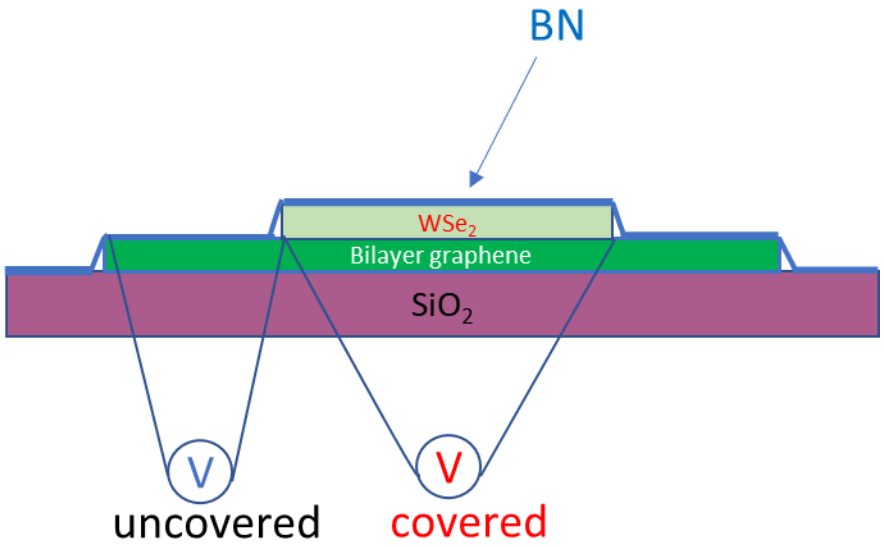

Figure 5.5. Device schematic diagram.

5.5.2 Gate dependence at low temperatures

Two-terminal resistance is measured between contacts 1 and 4, which is the sum of the covered and uncovered part. We monitor temperature dependence of resistance by measuring the gate dependence during cooling down, as shown in Fig. 5.6. From the gate dependence, there is a clear main Dirac point around zero, which means graphene is slightly electron doped. This peak comes from the charge neutral point of the covered part since the channel length is about three times of the uncovered part. Hence, the resistance is dominated by the covered part. The gate dependence is not symmetric about the Dirac point, there is a 'shoulder' feature at the electron side around 21 V. Since we measure both the covered part and uncovered part, it is natural to assume the 'shoulder' is the second Dirac point from the uncovered part. There is convincing evidence to show

our assumption is right in the next section. The resistance at the Dirac point in the covered part increase monotonically while there is no significant increase in the uncovered part. From 25 K to 2 K, the covered part increases by 38% while the uncovered part only increases by 4%, as shown in Fig. 5.7. The value of the Dirac point of the covered region is only slightly negative, so we can cover it in the full temperature ranging from 2K to 300K, as shown in Fig. 5.8. The resistance increases by 250% from 300K to 2K.

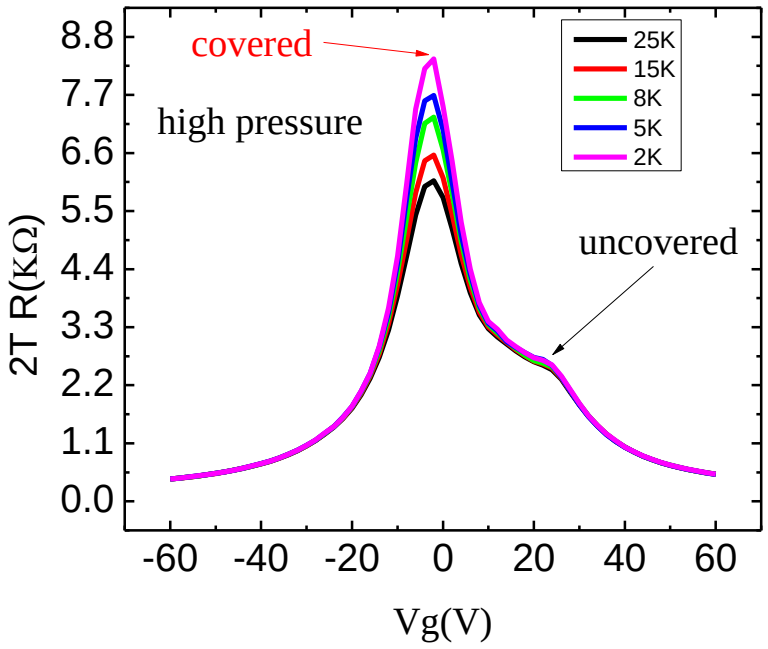

Figure 5.6. Gate voltage dependence at different temperatures under high pressure.

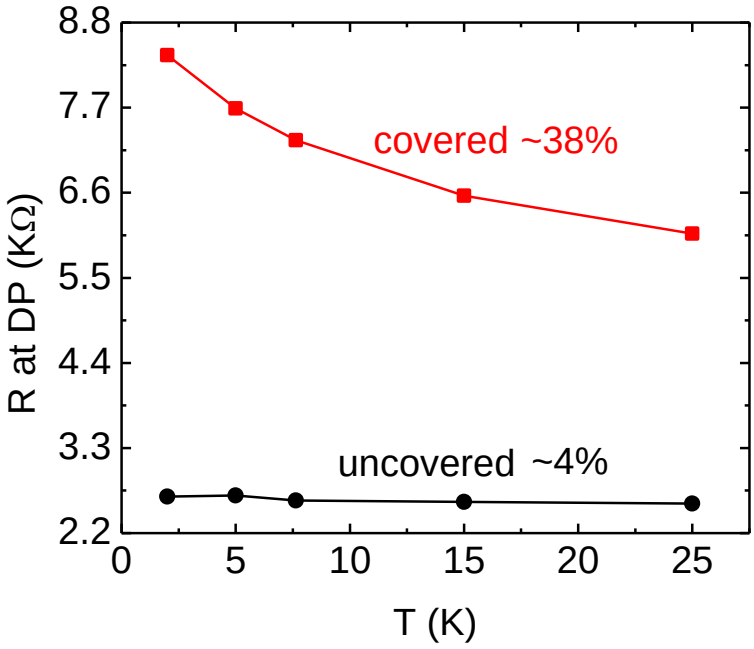

Figure 5.7. Temperature dependence of Resistance at Dirac point for the covered and uncovered part in the temperature range from 2K to 25K.

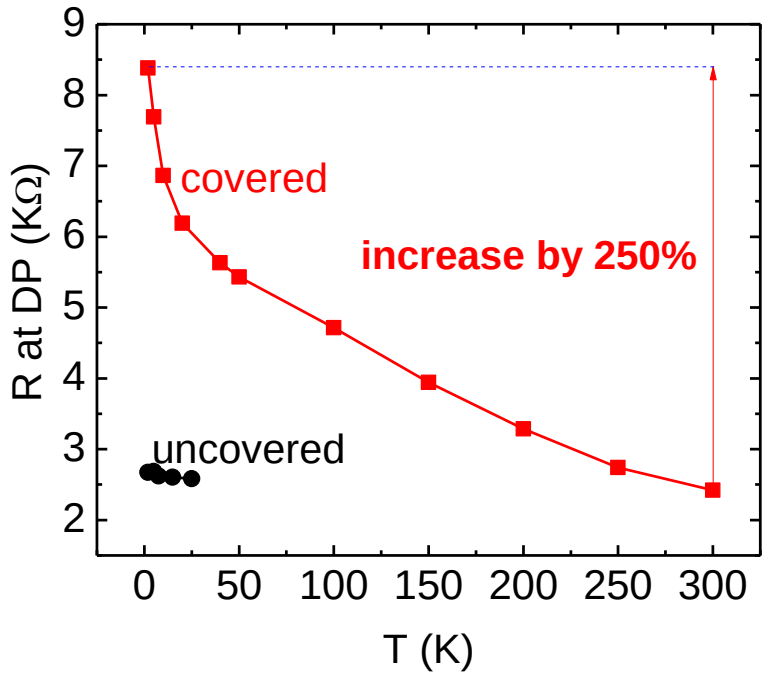

Figure 5.8. Temperature dependence of Resistance at Dirac point for the covered and uncovered part. The full temperature of the covered part ranges from 2K to 300K.

5.5.3 MR at 2K

At three different gate voltages V_g = -60V, 0V and 60V, which covers the full density ranging from -4.5×10^{12} cm^{-2} to 4.5×10^{12} cm^{-2} in the covered part and -3.0×10^{12} cm^{-2} to 6.0×10^{12} cm^{-2} in the uncovered part, MR shows WL without detectable WAL signal, as shown in Fig. 5.9. This is contradictory to my colleague's work[22] and previous work.[21] This doesn't mean SOC is not enhanced in the cover region. It is immersed in the stronger WL signal because the total resistances of both regions are measured. The detailed explanation is in section 5.5.2.

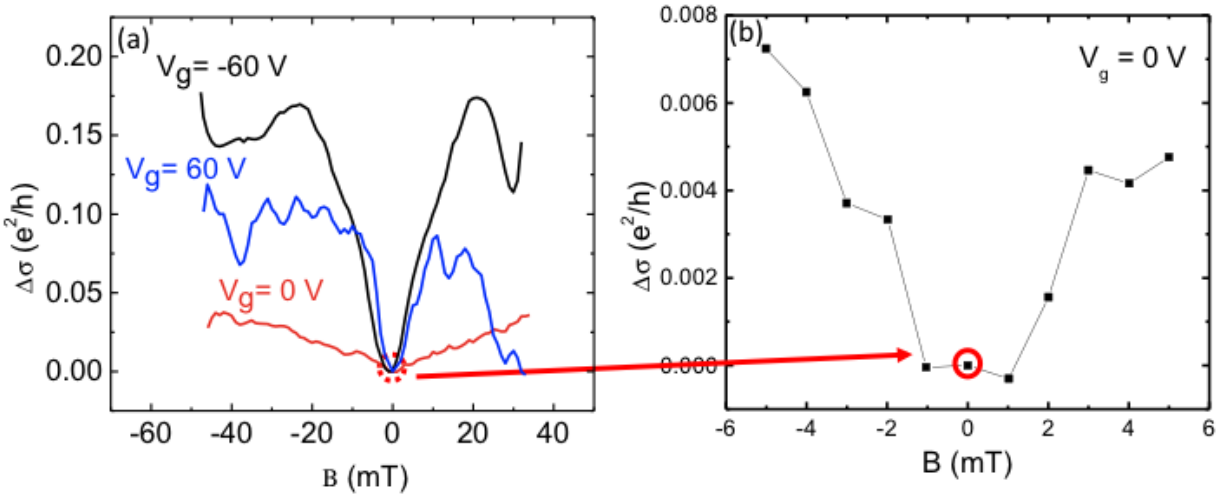

Figure 5.9. (a) MC at different gate voltages -60V, 0V and 60V at 2K. (b) Zoom in the low field range at Vg = 0V.

5.6 Back to zero pressure

When the device is released from pressure and demounted from the pressure cell, we have much more freedom to do the connections. There are six contact leads connected to the graphene device, allowing for four terminal resistance measurements without

contact resistance. Now the covered part and uncovered part are measured separately, as shown in Fig. 5.10. From the heavily hole doping of uncovered part graphene, which has contact with SiO_2 and boron nitride (BN), we can tell that graphene has good contact with SiO_2. But it is more hole doped compared to high pressure, which may be caused by the fact that BN bounces back after releasing pressure and has worse contact with graphene. As we know, BN is a flat and clean substrate for graphene and the position of charge neutral point of graphene on BN is usually close to 0 V. For the covered part, its doping still depends both on WSe_2 and SiO_2. WSe_2 usually makes graphene electron doped, as shown in Fig. 5.11, where the structure is WSe_2 underneath graphene and in opposite order with Fig 5.10. Hence, the doping of graphene is only determined by WSe_2, resulting in slightly electron doped in graphene. The electron doping is the same with the covered part under high pressure, which pressure could decrease the distance between graphene and WSe_2, enabling better contact and the doping of graphene is more affected by WSe_2. After releasing pressure, the Dirac point of the covered part shifts from slightly n-doped to p-doped, indicating worse contact with WSe_2. In conclusion, the position of the Dirac point serves as an indicator of pressure effects and the pressure effects could be mimicked as the ‘spring’ model.

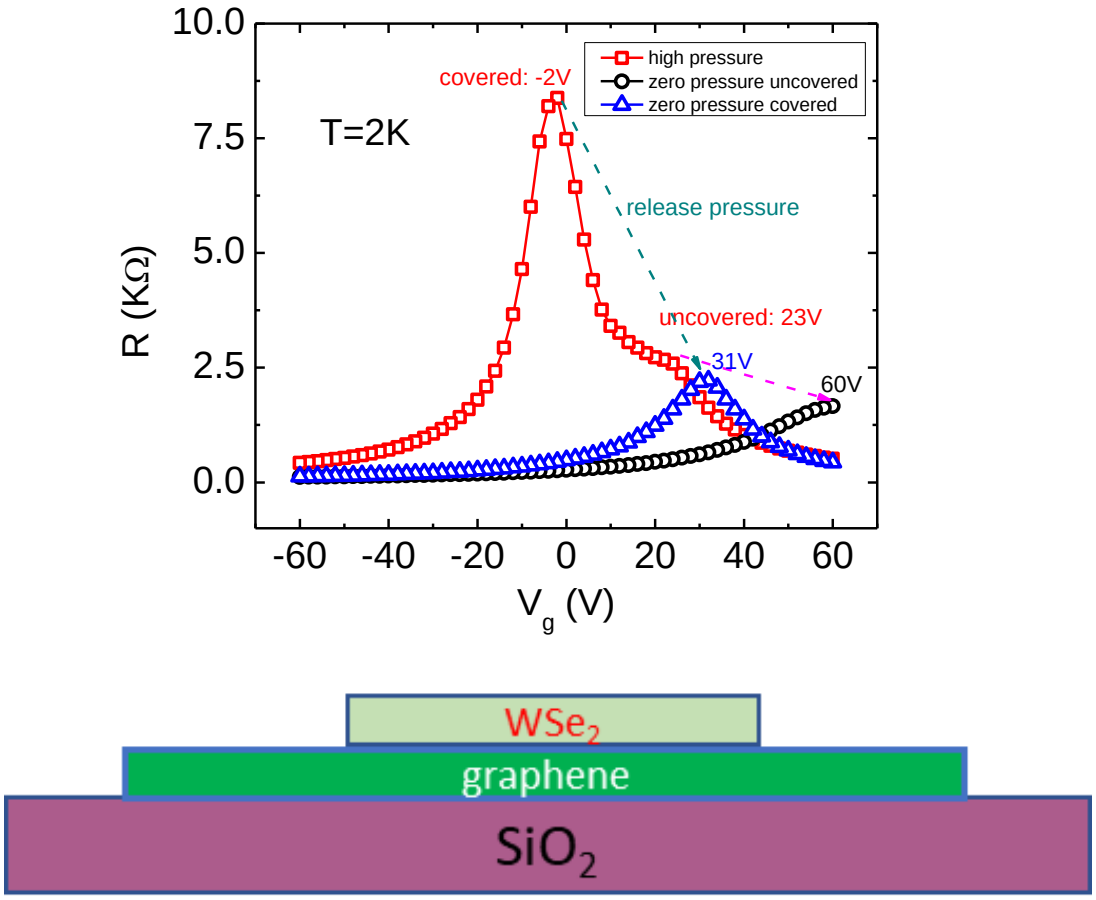

Figure 5.10. Comparison of the gate dependence between the covered and uncovered part at high pressure and no pressure. The position of Dirac point of the covered part shifts from -2V to 31V, while the uncovered part shifts from 23V to 60V.

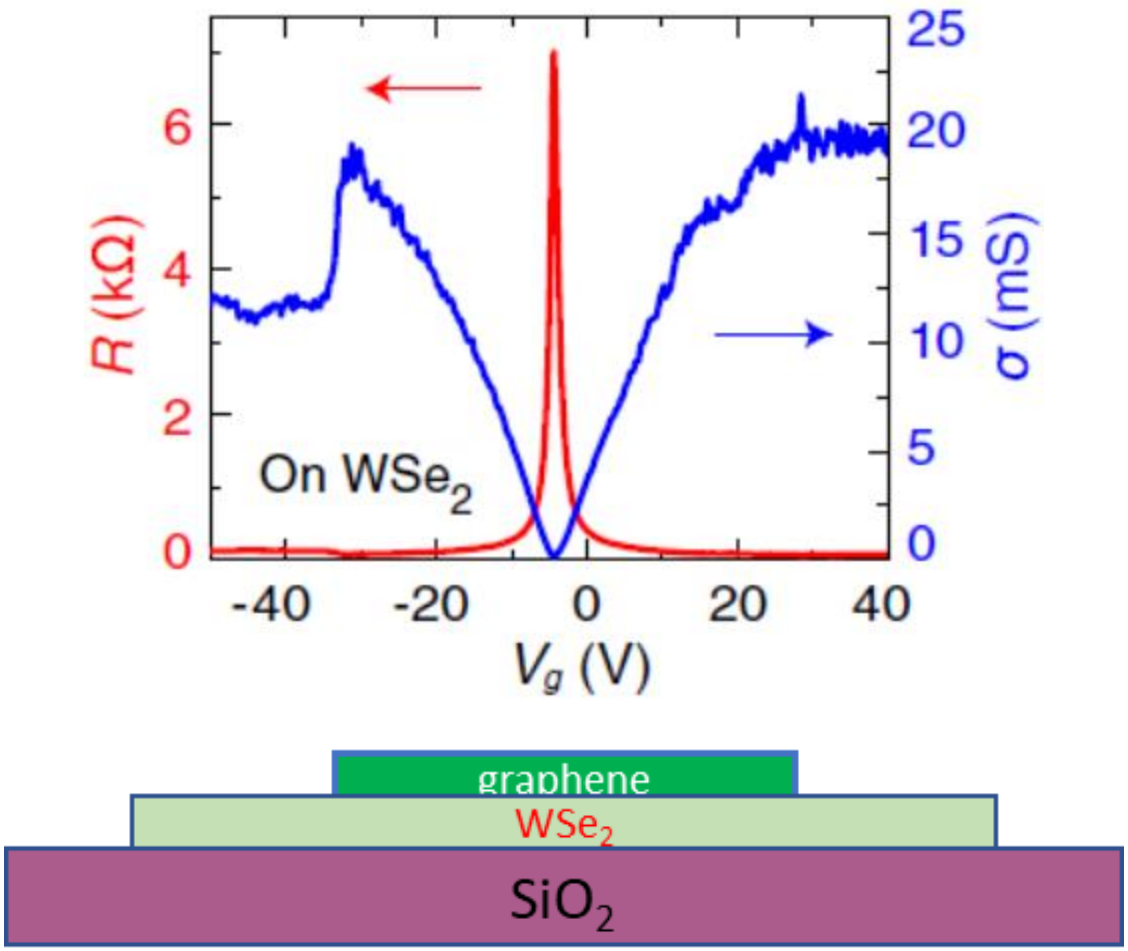

Figure 5.11. Gate dependence of graphene on WSe_2 [Wang, Zhe, *et al*. "Origin and magnitude of 'designer' spin-orbit interaction in graphene on semiconducting transition metal dichalcogenides." *Physical Review X* **6** (2016)], the device structure is in opposite order with Fig 5.9, which is WSe_2 on graphene.

To estimate the mobility in the covered and uncovered parts, the conductivity versus gate is plotted, as shown in Fig 5.11. By fitting the slope value and using the capacitance model, the mobilities are estimated as $\mu = 1.02\times10^4$ $cm^2/V\cdot s$ in the covered region and $\mu = 3.283\times10^3$ $cm^2/V\cdot s$ in the uncovered region. The capacitance value of the 290 nm SiO_2 is estimated as $C = 7.5\times10^{10}$ cm^2/V.

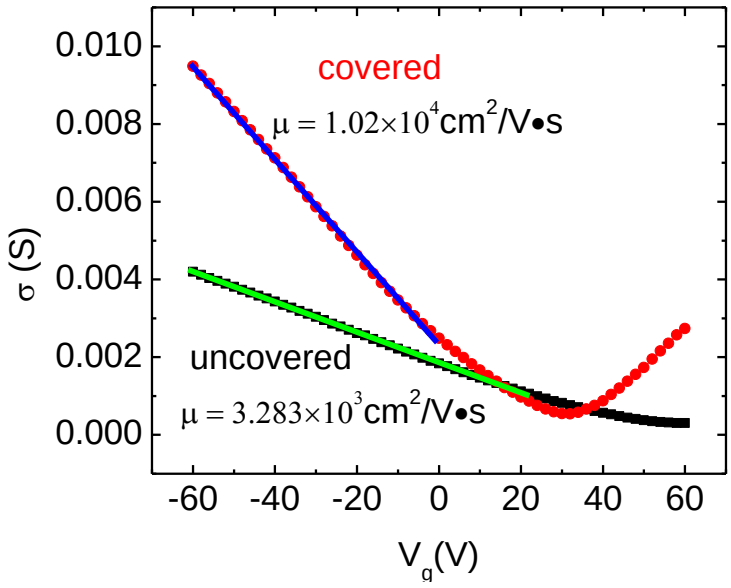

Figure 5.12. Gate voltage dependence of the conductivity. The aspect ratio of the covered part and uncovered are 1.2 and 0.5, separately. Mobility is extracted out by fitting the slope in the linear region.

5.6.1 Separation of the contribution from the covered and uncovered parts

We measure the gate dependence of the covered and the uncovered part separately and plot together with the sum of them. Simultaneously, the two-terminal resistance between 1, 4 is measured, as shown in Fig. 5.4. The magenta one is the total two terminal resistance of the covered and uncovered part and again there is a 'shoulder', as shown in Fig. 5.13. The blue one is the sum of four terminal resistance of uncovered part and covered part. They match very well and the 'shoulder' position is right on the position of the charge neutral point of the uncovered part. This provides unambiguous evidence that the 'shoulder' feature is the Dirac point of the uncovered part under the high pressure. The contact resistance is estimated by subtracting the blue one from the

magenta one, which is very small about 40 Ω and keeps constant away from Dirac point, as shown in Fig. 5.14.

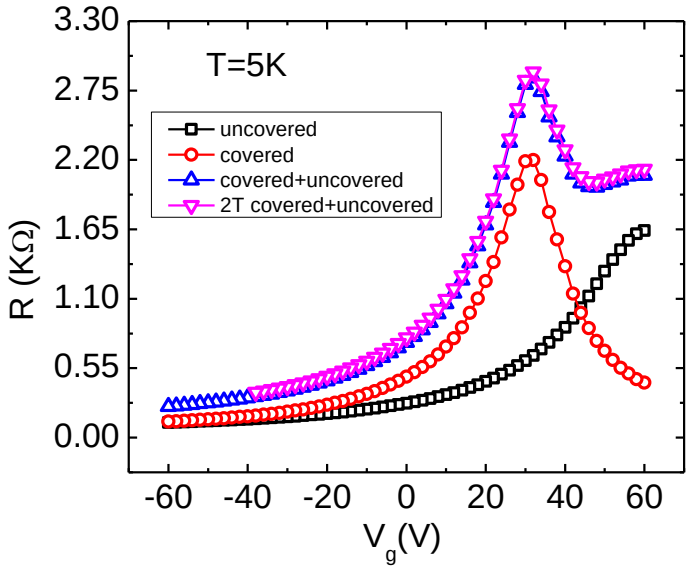

Figure 5.13. Comparison between two-terminal and four-terminal measurements

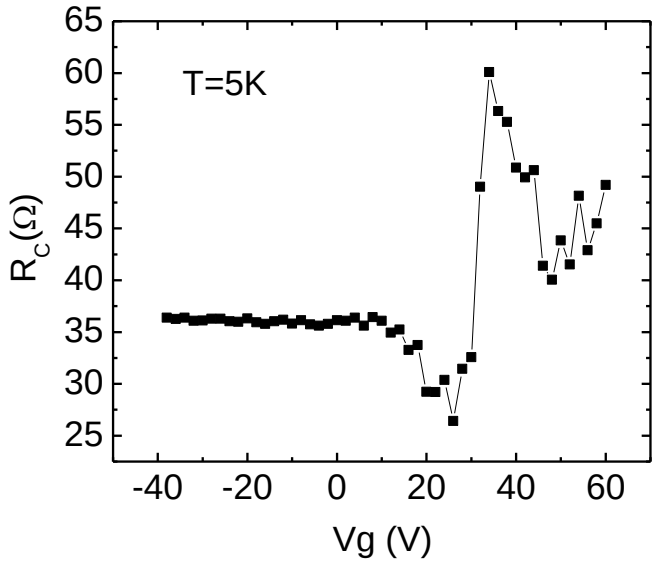

Figure 5.14. The gate voltage dependence of contact resistance. It is extracted out by subtracting four-terminal resistance from the two-terminal resistance.

5.6.2 Comparison of MR between the covered and uncovered parts

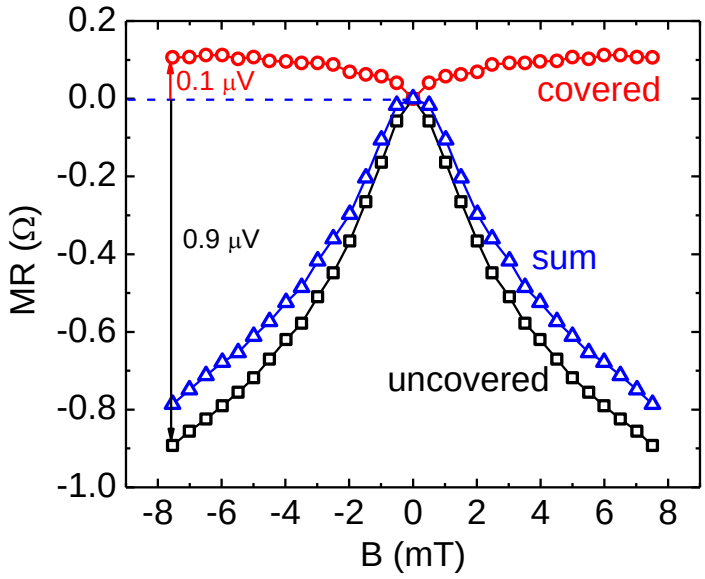

Figure 5.15. MR comparison between the covered part and uncovered part at Vg=-60V. The WL signal is about eight times magnitude larger than the WAL signal.

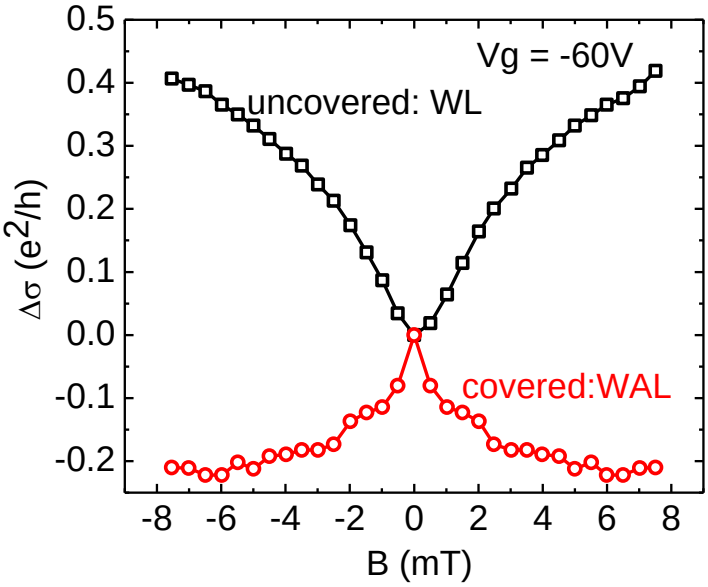

Figure 5.16. MC comparison between the covered part and uncovered part. Covered part shows WAL while uncovered part shows WL.

For the MR measurement at 2K, the covered part shows clear WAL while the uncovered part shows WL, as indicated in Fig. 5.15. This is strong evidence that the spin orbit coupling in graphene is enhanced by proximity effects with WSe_2, which is consistent with my colleague's work with graphene/WS_2 heterostructure.[29] It worth noting that bilayer graphene has Berry's phase 2π from psuedospin, which doesn't lead to WAL. The occurrence of WAL in bilayer graphene provides unambiguous and more direct evidence of the interfacial induced SOC than monolayer graphene.[21] If we add these two-opposite signs of signal around zero magnetic field, the sum still behaves as WL. This is because WL signal is about eight times of magnitude larger than the WAL signal, dominating the signal if we measure the sum of the covered and uncovered part, which is the case under high pressure as shown before. The fact that WAL is not observed under high pressure does not mean the absence of induced SOC in the covered part. It is immersed in the much larger WL signal from the uncovered region.

5.6.3 Dephasing length difference in the covered and uncovered regions

To get better insight on the covered part and uncovered part, we do the WAL fitting in the covered region and WL fitting in the uncovered region. The MC equation for bilayer graphene with SOC is $\Delta\sigma(B) = -\frac{e^2}{2\pi h}\left[F\left(\frac{B}{B_\varphi}\right) - F\left(\frac{B}{B_\varphi+2B_{BR}}\right) - 2F\left(\frac{B}{B_\varphi+B_{SOC}}\right)\right]$ assuming that the intervalley and intravalley scattering is much larger than the SOC scattering strength, which is the same as in the single layers. Here B_{BR} is the Rashba SOC term and $B_{SOC} = B_{BR} + B_{KM}$, which is the sum of Rashba SOC and KM

SOC. The MC for bilayer graphene without SOC is $\Delta\sigma(B) = \frac{e^2}{\pi h}\left[F\left(\frac{B}{B_\varphi}\right) - F\left(\frac{B}{B_\varphi+2B_i}\right) + 2F\left(\frac{B}{B_\varphi+B_*}\right)\right]$, which has the opposite sign in the third term compared with the single layer equation. The fitting works well and the extracted phase coherence lengths are 1.296 μm for the covered region and 0.755 μm for the uncovered region. These values are in a reasonable range and agree with the previous work.[21] The phase coherence length in the covered part is longer than the uncovered part. Phase coherence length is related with diffusion constant and transport time as $L = \sqrt{D\tau}$. Diffusion constant $D = \frac{\mu E_F}{2e}$.[115] Here, μ is mobility, E_F is the Fermi level and e is the electron's charge. In bilayer graphene, $E_F = \hbar v_F\sqrt{\pi n}$ [116]and $v_F = \frac{\sqrt{\pi n}}{0.033 m_e}$.[117] Hence, E_F is proportional to carrier density. As a result, L is proportional to $\sqrt{\mu n \tau}$. Consequently, $\frac{L_{covered}}{L_{uncovered}} = \sqrt{\frac{\mu_{covered} n_{covered} \tau_{covered}}{\mu_{uncovered} n_{uncovered} \tau_{uncovered}}} =$ 1.721. The Rashba SOC strength calculated from the fitted SOC scattering time is about 1 meV and the KM SOC is negligible. The reason is that the out-of-plane inversion symmetry is broken, which is the Rashba type SOC.

5.7 Pressure dependence of insulating behavior

After releasing pressure, not only the positions of the Dirac point shift but also the insulating behavior in the covered region weakens a lot. To better understand the change in insulating behavior of the covered part, the temperature dependence of the covered and the uncovered part at zero pressure and high pressure is plotted together, as shown in Fig. 5.18. For the covered part, under high pressure, there is clear insulating behavior in the

temperature dependence of resistance in the full temperature range from 300K to 2K, especially in the low temperature range from 50K to 2K. When the pressure is released, the steep slope disappears. While in the uncovered part, there is no such insulating trend and there is no significant difference under high pressure and no pressure. Comparison between the black and red one shows that only the covered with WSe_2 region behaves insulating behavior. Comparison between the black one and blue one shows only under high pressure, the insulating behavior is significant. These two comparisons suggest the insulating behavior is an outcome of high pressure together with the proximity effects from WSe_2. As we know, TMD could hybridize with graphene and increase the SOC in graphene up to a few meV.[21,22] The MR for the covered part at zero pressure shows WAL because of the enhancement of SOC in graphene, which is consistent with previous reports.[21,22] As we know, proximity effect is very sensitive to the distance between the material and the adjacent material.[25] If graphene is pressurized to be closer to WSe_2, the proximity induced SOC will increase. The strong SOC could open a gap and cause the peculiar insulting behavior in graphene. In principle, we should be able to observe stronger WAL in the covered part, but it is just immersed in the WL background when we measure the total channel of the covered and uncovered part together.

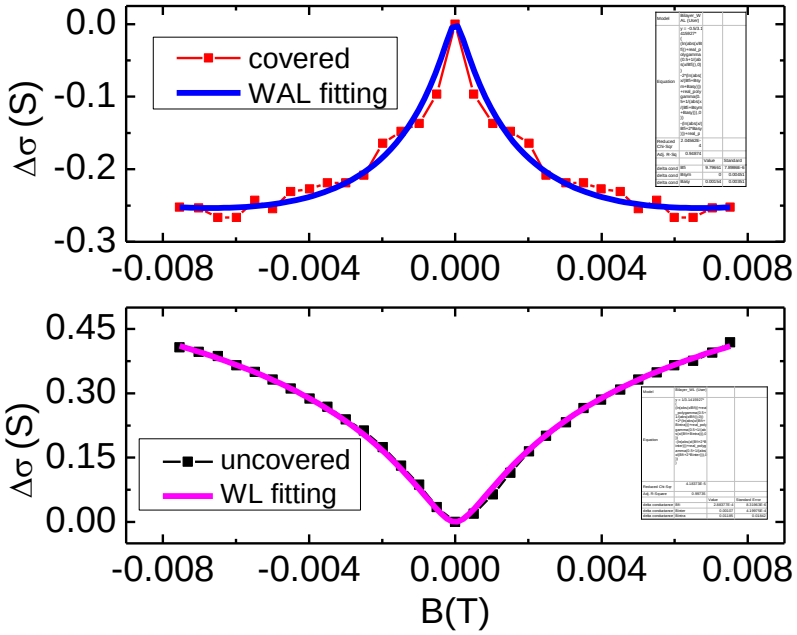

Figure 5.17. WAL fitting in the covered region and WL fitting in the uncovered region. The red square and black square points are experimental data and blue and magenta are the fitted curves. The gate voltage is -60V.

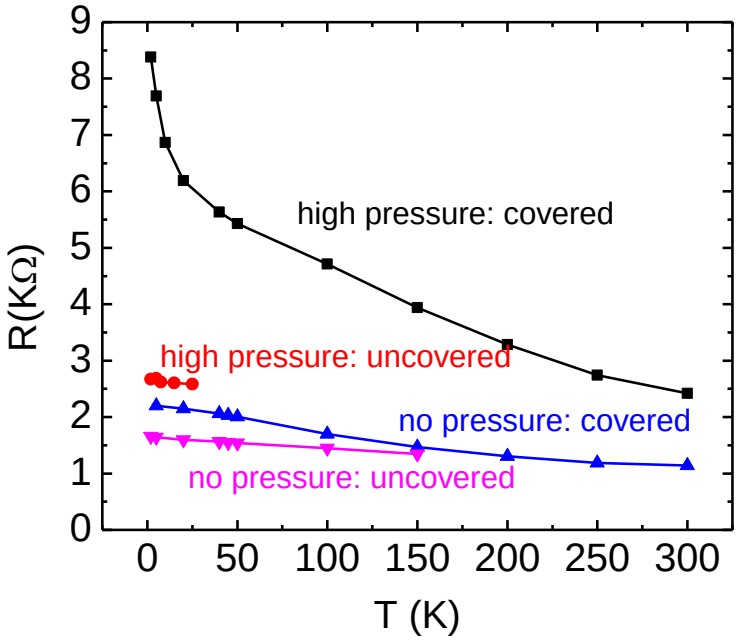

Figure 5.18. Temperature dependence of the covered and uncovered part at zero pressure and high pressure.

5.8 Pressure dependence of MR

To study the pressure effects on the MR, MR at different carrier density under zero pressure and high pressure are measured, as shown in Fig. 5.19. Keep in mind that MR here contains the covered and uncovered region. However, it is dominated by the uncovered region since its MR magnitude is much larger than the covered region. There are two- opposite physical process: uncovered part shows WL (negative MR) while covered part shows WAL (positive MR), the WL is suppressed by the WAL. Under small pressure, the suppression of WL caused by the WAL from the covered part is not strong enough and the total MR behaves prominent WL. However, under high pressure, the WL is completely suppressed at Vg= ± 60 V. Only at Vg=0 V, which is close to Dirac point and WAL from the covered part is very small because of the stronger dephasing, the WL recovers. The significant suppression of WL under high pressure indicates the proximity effect between graphene and WSe_2 is enhanced by pressure.

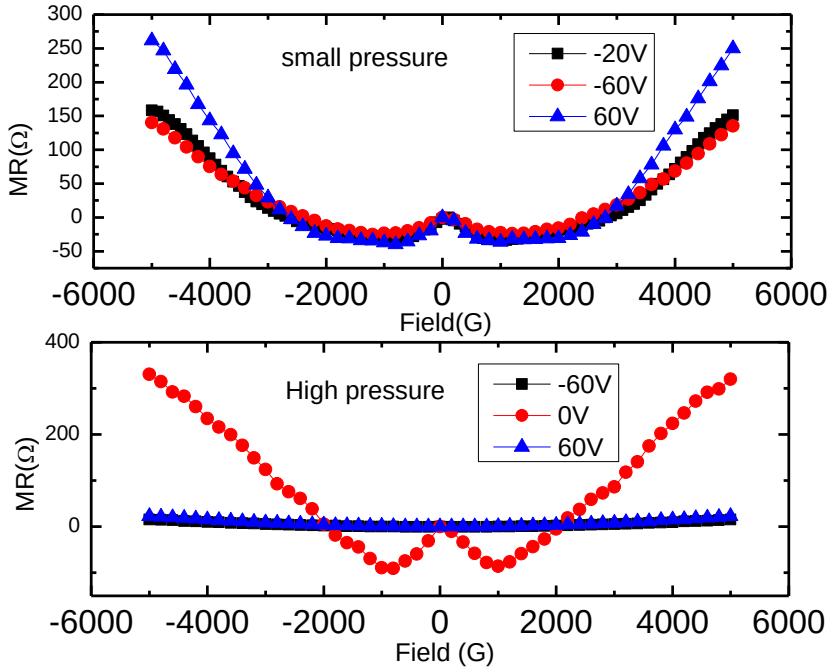

Figure 5.19. MR comparison under small pressure and high pressure.

5.9 Unusual carrier density dependence of WL

We observed the unusual carrier density dependence: higher carrier density-weaker WL, which is opposite with the conventional trend for WL in graphene, as shown in Fig. 5.20. From -60 V, -40V, -20V, -10V to 0V in the hole region, the WL gradually grows. In typical MR measurement in graphene, the WL and WAL at lower carrier densities are both weaker because of the stronger dephasing process due to the stronger electron-electron interaction.

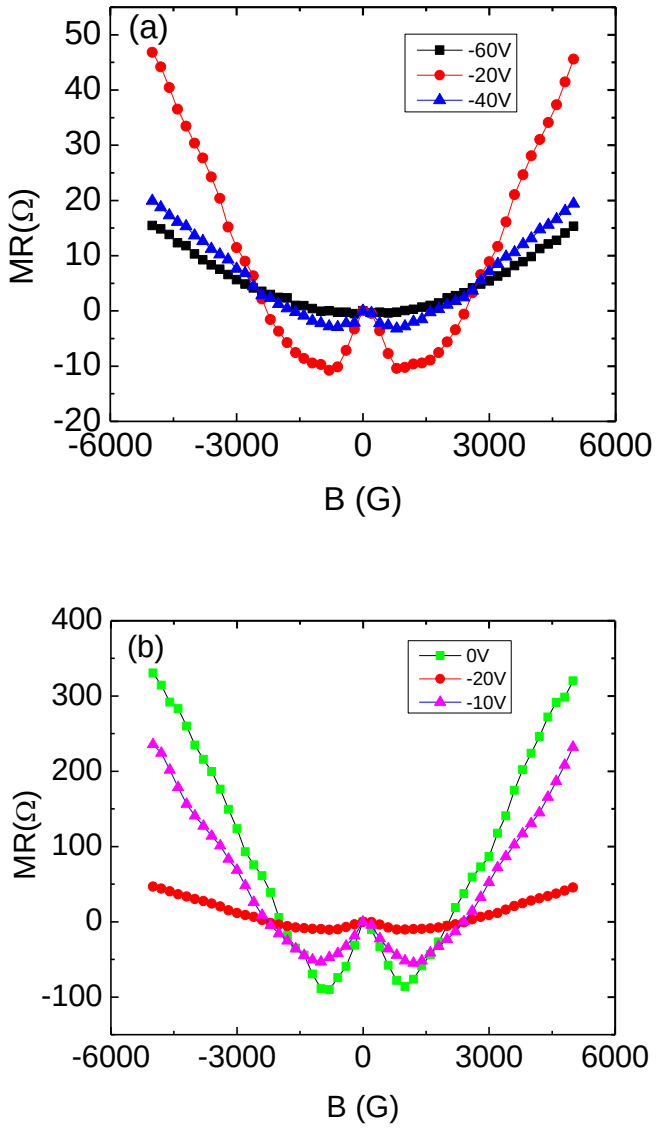

Figure 5.20. MR at different gate voltages. (a) MR at gate voltage -60V, -40V and -20V. (b) MR at gate voltage -20V, -10V and 0V.

Remember the MR is the sum of the covered part and uncovered part. The explanation is as followings: The WAL has the same conventional trend: weaker at lower carrier density. When approaching the Dirac point, the suppression of WL caused by the

WAL from the cover region becomes weaker and so is the WL. But since covered part dominates in the resistance, the net effect is stronger WL.

5.10 Remounting on the pressure cell

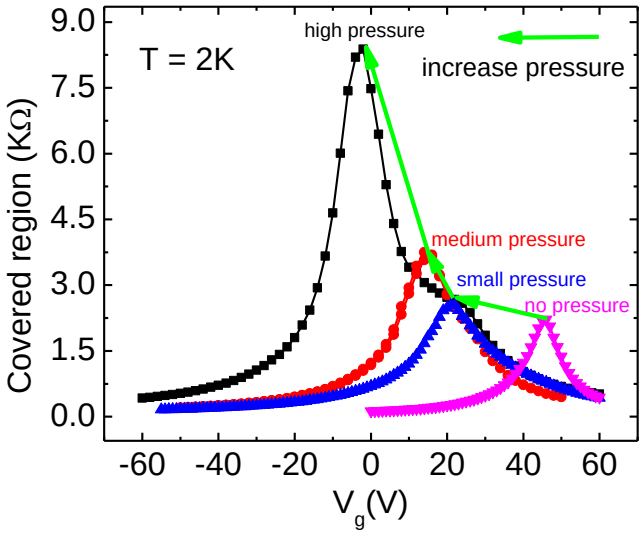

Figure 5.21. Gate voltage dependence for the covered part under different pressures at 2K.

To check if the pressure effects are reversible, we remount the device in the pressure cell and gradually increase the pressure to another two pressures: small value and medium value. We carefully redo the connections and have more working connections, enabling the four-terminal resistance measurement under small pressure and medium pressure. To investigate the pressure effects, gate dependence for the covered part under different pressures are plotted together in Fig. 5.21. Graphene is very sensitive to the charge impurities in the substrates.[118] If the effect of pressure on graphene is having better contact with the substrate or the neighboring TMD material, the doping of

graphene changes, resulting in the shifting of the position of the Dirac point. The covered part graphene becomes less p-doped with increasing pressure, which is consistent with the previous hypothesis that graphene becomes more n-doped by having better contact with WSe_2.

Graphene is p-doped at zero pressure, behaving as the typical doping type on SiO_2 substrate. For graphene covered with WSe_2 part, one layer is in contact with SiO_2 while the other layer is in contact with WSe_2. Usually, the charge impurities and defects on SiO_2 makes graphene p doped while WSe_2 substrate makes graphene n doped.[21] These two substrates have opposite doping on the graphene and the overall doping is determined by the dominating one. Under small pressure, there is clear shifting of the Dirac point from 46V to 21V at 2K, indicating better contact between graphene and WSe_2 since WSe_2 is an electron donor. When the pressure is increased to a medium value, the position of the Dirac point keeps shifting closer to zero from 21V to 15V, suggesting the distance between graphene and WSe_2 is even smaller. However, graphene still behaves hole doped. Once the pressure is increased to a high value, there is clear shifting in position of the Dirac point from positive voltage 15V to slightly negative voltage -2V, which means the doping of graphene changes from hole doped to electron doped. Under high pressure, the doping of graphene is dominated by WSe_2.

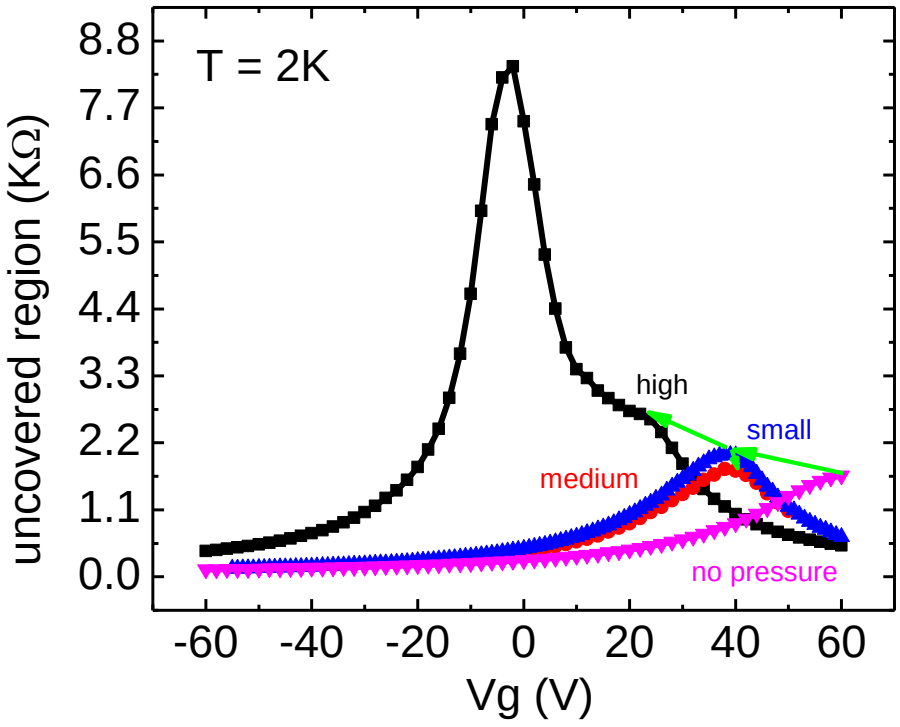

Figure 5.22. Gate voltage dependence for the uncovered part under different pressures at 2K.

For the uncovered part, the gate dependence under different pressures is shown in Fig. 5.22. Under small pressure, graphene become less hole doped. We can understand the shifting this way. For bilayer graphene, one layer is in direct contact with SiO_2 while the other layer is in contact with BN but not in direct contact because there are gold electrodes in between. Pressure will press BN downward to have better contact with graphene, hence, the charge neutral point moves closer to zero because BN is clean and flat substrate. From 1st pressure to 2nd pressure, there is no significant shifting of the Dirac point, which means graphene is already in good contact with both BN and SiO_2. Only when the pressure is increased to a high value, graphene can have even better

contact with BN. Another indicator is the curvature of the gate dependence, the mobility in the hole side increases from zero pressure to small pressure, which is also the outcome of better contact between graphene and BN.

5.11 Temperature dependence of two regions

Under small and medium pressure, there is striking difference in the temperature dependence of resistance, as illustrated in Fig. 5.23. For the covered part, the resistance at Dirac point is increasing monotonically with decreasing temperature. However, in the uncovered part, there is no observable increase. That is, the covered part behaves insulating behavior while the uncovered part has no such trend. This is consistent with the previous measurement when the device is at high pressure and back to zero pressure, confirming that the insulating behavior of graphene is caused by pressure and WSe_2. And we noticed the insulating behavior is not as strong as under high pressure, indicating the pressure-dependent nature, as it will be discussed more in the next session 5.11.

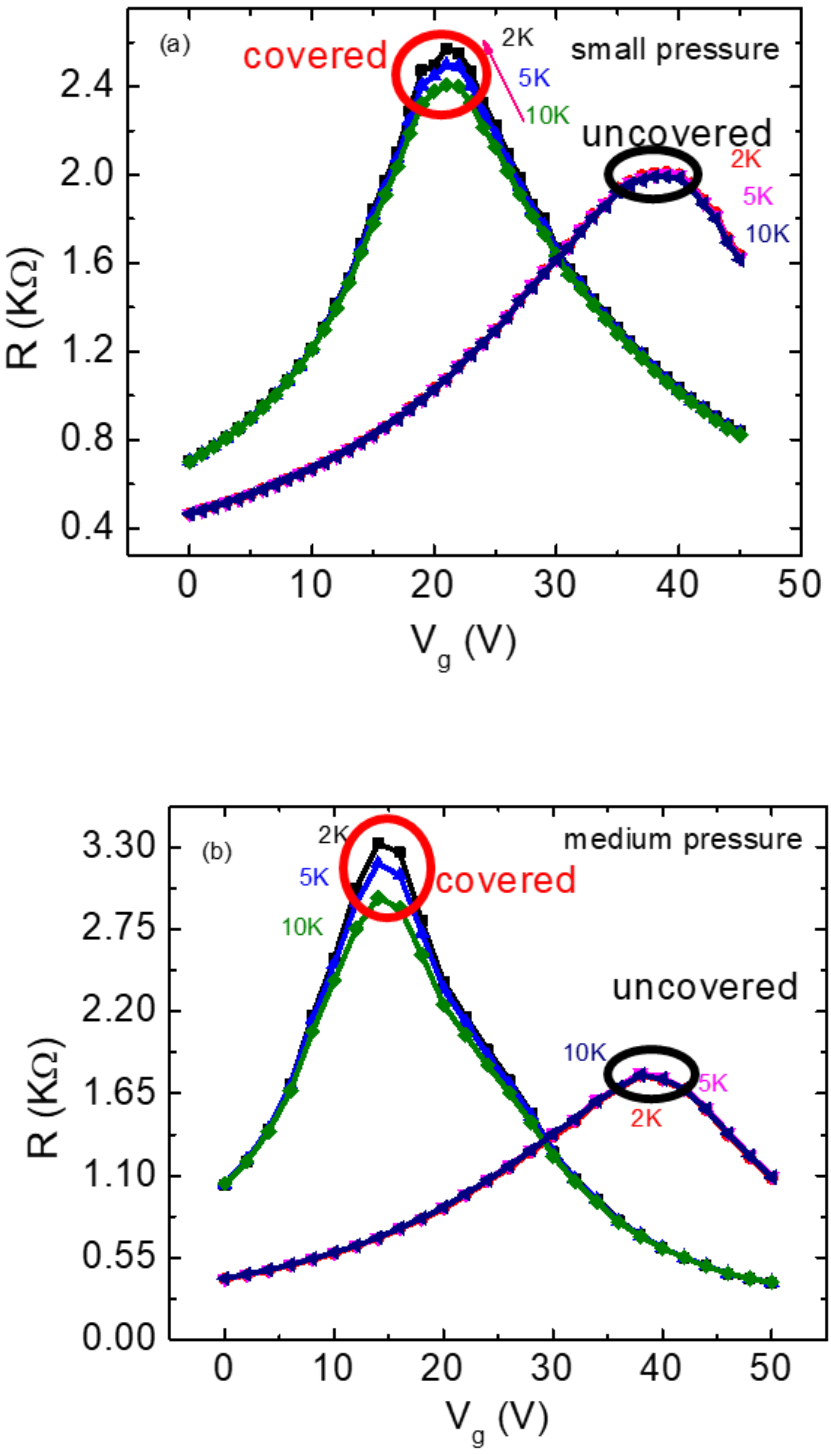

Figure 5.23. Gate dependence for covered and uncovered part at different temperatures.

5.12 Temperature dependence at Dirac point under different pressures

To better study the origin of the insulating behavior, the temperature dependence of the resistance at Dirac point for the covered part under different pressures is plotted, as shown in Fig. 5.24. The insulating behavior becomes stronger with increasing pressure. While for the uncovered part, there is no clear insulating behavior under all pressures, as shown in Fig. 5.25, indicating that pressure and TMD are the prerequisites of the insulating behavior.

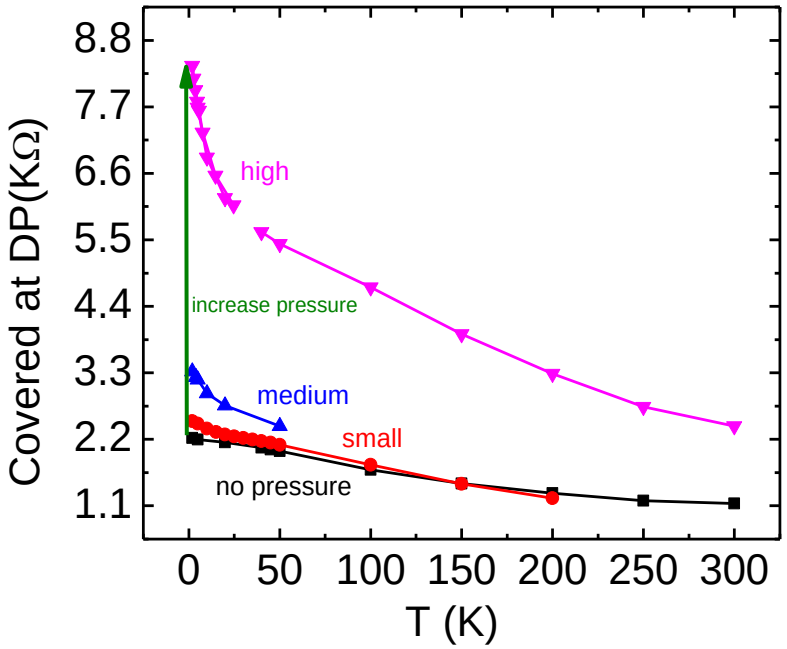

Figure 5.24. Temperature dependence of the covered part under different pressures.

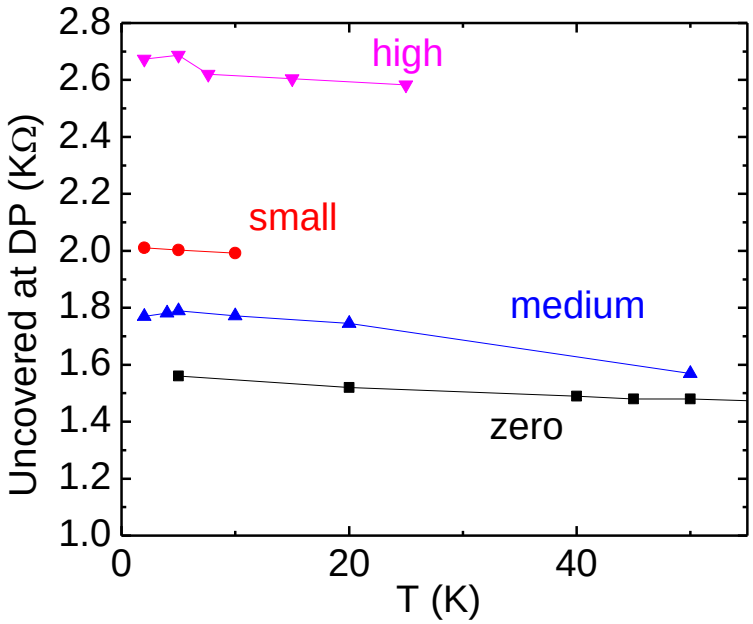

Figure 5.25. Temperature dependence of the uncovered part under different pressures.

5.13 Band gap value

To extract the bandgap values, the linear fittings are done on the lnR vs 1/T curves at no pressure and high pressure separately. The fitted slope value is $\frac{E_g}{2k_B}$, where E_g is the band gap value and k_B is the Boltzmann constant. The band gap value increases from 13.48 meV to 29.85 meV once the high pressure is on, suggesting stronger proximity effects from WSe_2.

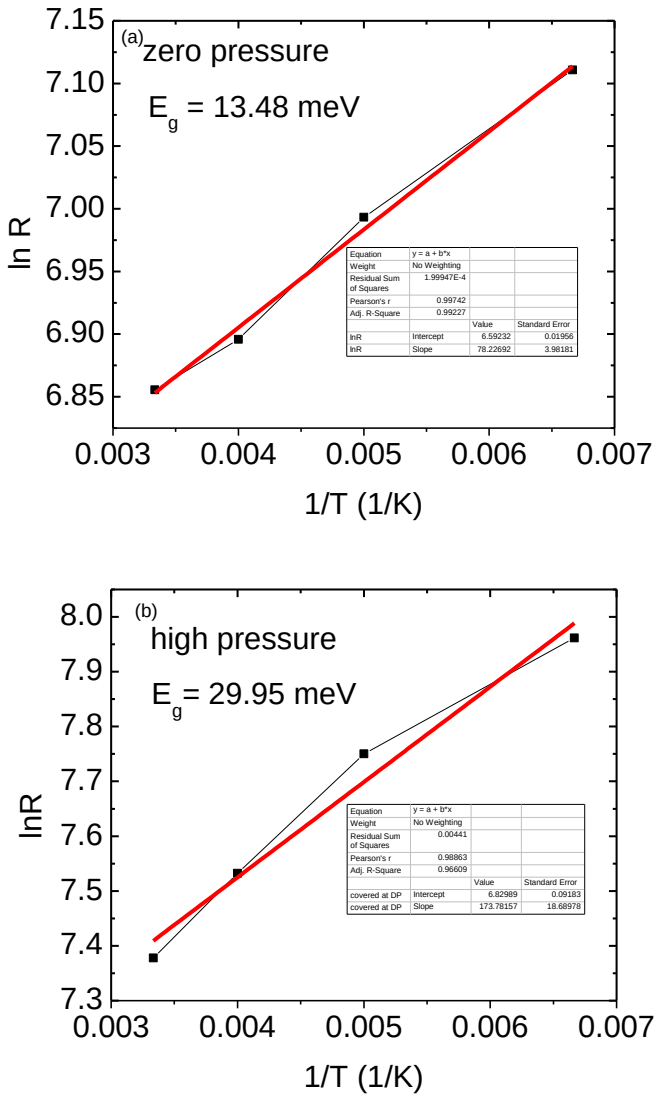

Figure 5.26. lnR vs 1/T at zero pressure and high pressure. The band gap values are extracted out from the slope by linear fitting. The value under high pressure is more than double than the no pressure.

5.14 Explanation for the insulating behavior (First hypothesis)

It was proved that strain can open a band gap in a metallic carbon nanotubes (CNTs) and will dramatically change the electronic band structure of CNTs.[119-121] The band gap

in a semiconducting CNT can be modified with about 100 meV per 1% stretch.[119] It is reasonable to predict that the uniaxial strain can open a gap in graphene[122] since the two carbon sublattices of graphene are inequivalent under strain and it will break sublattice symmetry.[123-125] As an example, a band-gap opening is predicted for graphene growth on hexagonal boron nitride substrate due to the breaking of sublattice symmetry.[123] The method of strain induced band-gap opening would be more efficient compared to other methods, such as electric field tuning on bilayer[126] or molecule adsorption.[124] It is possible that hydrostatic pressure could induce a strain in graphene plane, especially when the heterostructure is not flat along graphene plane. The uneven force on BN may act on the graphene and stretch out graphene in plane. The covered part with WSe_2 will have more sublattice asymmetry because the heavy atoms W are distributed on the graphene and there is a lattice mismatch between graphene and WSe_2. The elongation in one direction caused by strain will cause the shrinking on the perpendicular direction. It would help to have an estimation on the order of strain. The Young's modulus for bilayer graphene is about 2.0 ± 0.5 TPa by Raman spectrum analysis[127] and is in the same order of 1 TPa by simulation.[128] The applied hydrostatic pressure is in the order of 1 GPa, resulting in the strain in the magnitude of $\sim \frac{1\,GPa}{1\,TPa}$ = 0.1%. If each layer of bilayer graphene is subjected to different strengths of homogeneous strains, the perpendicular electric fields across the two layers can be generated without any external gate potential.[129] The effect originates from the asymmetric generations of pseudoscalar potential in each layer of strained bilayer graphene, which alter their work functions significantly.[130] Specifically, each layer in bilayer graphene experiences a different

magnitude of homogeneous strain because only the top layer is pinched by the metallic leads and WSe_2. Consequently, the work function of the two asymmetric strained layers are different, generating a net charge transfer between these two layers. The strain-induced electric fields will break the symmetry in the onsite energy of the top and bottom layer.[131,132] We want to extract the band gap value by electronical transport measurement but it worth noting that the increase in resistance could be much smaller than the expected band gap value due to the extrinsic conduction through defects and carrier doping from charge impurities in the sample.[133] That means the band gap value will be underestimated.

5.15 Explanation for the insulating behavior (Second hypothesis)

We found our experimental results can be explained by a very recent theoretical proposal. For the BLG on monolayer WSe_2, it is found that the built-in electric field not only induces an orbital band gap of about 10 meV but also generates the proximity spin-orbit splitting of the valence band at K about 2 meV. Fig. 5.27 (a) shows the atomic structure for graphene on WSe_2. Fig. 5.28 (b) shows the fine structure in the low energy bands around K, the SOC of the valence band is about 2 meV, which is about two orders of magnitude greater than in the conduction band. The reason is the valence band is formed by the non-dimer B_1 in the bottom layer adjacent to WSe_2 while the conduction band is formed by the non-dimer A_2 in the top layer, as shown in Fig 5.27 (b). Proximity effects are very sensitive to the distance, it is naturally weak for the top layer. The proximity effects will build up a transverse field pointing from WSe_2 to BLG (we define

this direction as positive). The amplitude of the electric field and the induced band gap relies on the atomic distance between bottom layer graphene and WSe_2. As calculated before, the band gap under high pressure is more than two times of the band gap under no pressure, suggesting the enhanced proximity effects.

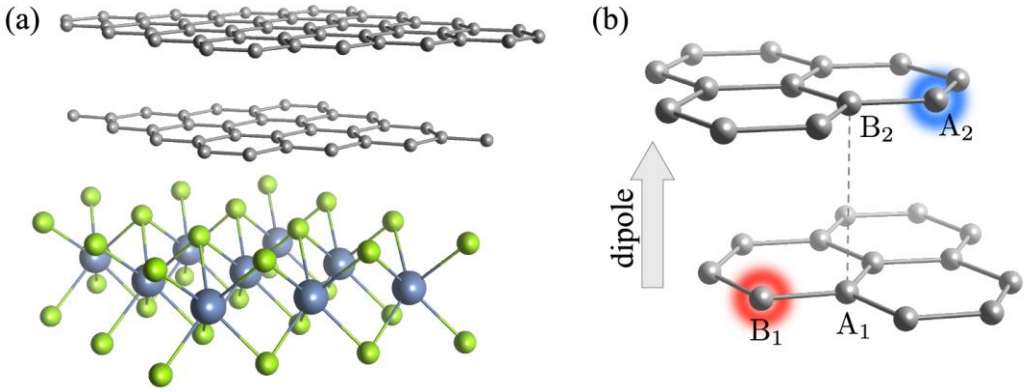

Figure 5.27. Schematic diagram to show the proximity effects. (a) Atomic structure of bilayer graphene on WSe2. (b) Orbitals on non-dimer atoms B1 and A2 form the low energy valence and conduction bands in the electronic structure of bilayer graphene. WSe2 layer is underneath the bottom layer so that B1 is closer to WSe2 and acquire much stronger proximity effects than A2. [Gmitra, Martin, and Jaroslav Fabian. "Proximity effects in bilayer graphene on monolayer WSe2: Field-effect spin-valley locking, spin-orbit valve, and spin transistor." arXiv preprint arXiv:1706.06149 (2017).]

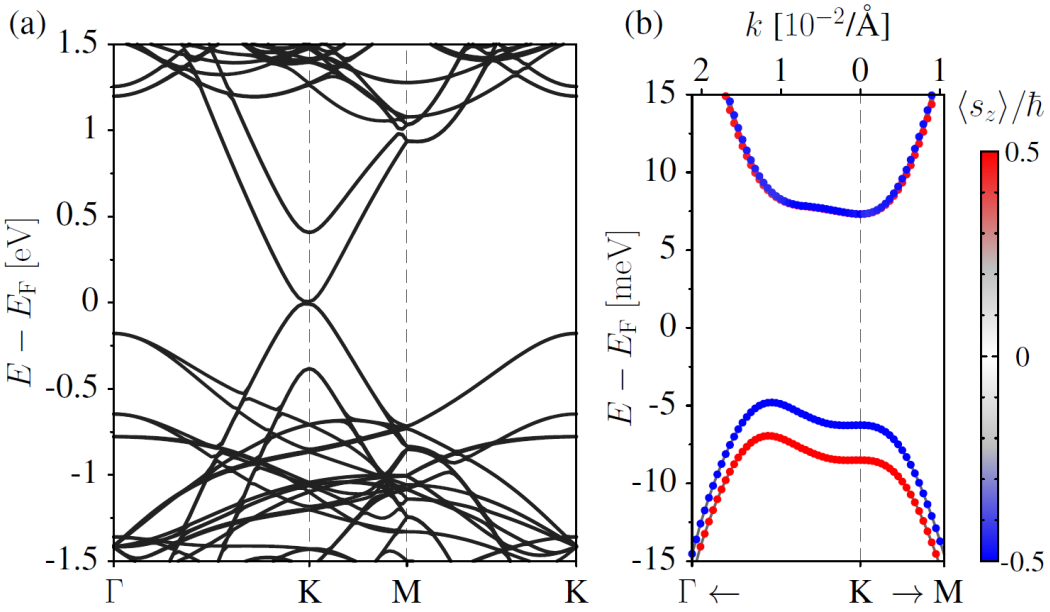

Figure 5.28. Band structure of graphene on monolayer WSe_2. (a) Calculated electronic band structure of bilayer graphene on WSe2 performed by Quantum ESPRESSO. (b) Zoom in view of the fine structure of the low energy bands close to the Fermi level. The red is spin up and the blue is spin down. [Gmitra, Martin, and Jaroslav Fabian. "Proximity effects in bilayer graphene on monolayer WSe_2: Field-effect spin-valley locking, spin-orbit valve, and spin transistor." arXiv preprint arXiv:1706.06149 (2017).]

In addition to the orbital effect, a spin splitting of in the order of 1 meV is induced in the valence band since B_1 is responsible for the valence band. This value is in the same order with the Rashba SOC strength of 1 meV calculated from WAL fitting.

In conclusion, WAL has been observed in the covered region with WSe_2 and only WL is observed in pristine region. This is unambiguous evidence to show the interfacial induced SOI in graphene. Band gap is opened due to the inversion symmetry broken and graphene behaves insulating. The band gap is larger under hydrostatic pressure, suggesting the enhanced proximity effects.

Bibliography

1 Novoselov, K. S. *et al.* Two-dimensional atomic crystals. *Proc Natl Acad Sci U S A* **102** (2005).

2 Mayorov, A. S. *et al.* Micrometer-scale ballistic transport in encapsulated graphene at room temperature. *Nano Lett* **11** (2011).

3 Balandin, A. A. *et al.* Superior thermal conductivity of single-layer graphene. *Nano Lett* **8** (2008).

4 Wilson, J. A. & Yoffe, A. D. Transition Metal Dichalcogenides Discussion and Interpretation of Observed Optical, Electrical and Structural Properties. *Adv Phys* **18** (1969).

5 Lu, J. M. *et al.* Evidence for two-dimensional Ising superconductivity in gated MoS_2. *Science* **350** (2015).

6 Saito, Y. *et al.* Superconductivity protected by spin-valley locking in ion-gated MoS_2. *Nat Phys* **12** (2016).

7 Xi, X. *et al.* Ising pairing in superconducting $NbSe_2$ atomic layers. *Nat Phys* **12** (2016).

8 Yu, Y. *et al.* Gate-tunable phase transitions in thin flakes of 1T-TaS_2. *Nat Nanotechnol* **10** (2015).

9 Gong, C. *et al.* Discovery of intrinsic ferromagnetism in two-dimensional van der Waals crystals. *Nature* **546** (2017).

10 Mermin, N. D. & Wagner, H. Absence of Ferromagnetism or Antiferromagnetism in One- or Two-Dimensional Isotropic Heisenberg Models. *Physical Review Letters* **17** (1966).

11 Zhang, W. B., Qu, Q., Zhua, P. & Lam, C. H. Robust intrinsic ferromagnetism and half semiconductivity in stable two-dimensional single-layer chromium trihalides. *J Mater Chem C* **3** (2015).

12 Wallace, P. R. The Band Theory of Graphite. *Phys Rev* **71** (1947).

13 Castro Neto, A. H., Guinea, F., Peres, N. M. R., Novoselov, K. S. & Geim, A. K. The electronic properties of graphene. *Rev Mod Phys* **81** (2009).

14 Novoselov, K. S. *et al.* Two-dimensional gas of massless Dirac fermions in graphene. *Nature* **438** (2005).

15 Zhang, Y., Tan, Y. W., Stormer, H. L. & Kim, P. Experimental observation of the quantum Hall effect and Berry's phase in graphene. *Nature* **438** (2005).

16 Young, A. F. & Kim, P. Quantum interference and Klein tunnelling in graphene heterojunctions. *Nature Physics* **5** (2009).

17 Stander, N., Huard, B. & Goldhaber-Gordon, D. Evidence for Klein tunneling in graphene p-n junctions. *Phys Rev Lett* **102** (2009).

18 Gorbachev, R. V., Mayorov, A. S., Savchenko, A. K., Horsell, D. W. & Guinea, F. Conductance of p-n-p graphene structures with "air-bridge" top gates. *Nano Lett* **8** (2008).

19 Beenakker, C. W. J. Colloquium: Andreev reflection and Klein tunneling in graphene. *Rev Mod Phys* **80** (2008).

20 Cheianov, V. V. & Fal'ko, V. I. Selective transmission of Dirac electrons and ballistic magnetoresistance of n-p junctions in graphene. *Phys Rev B* **74** (2006).

21 Wang, Z. *et al.* Origin and Magnitude of 'Designer' Spin-Orbit Interaction in Graphene on Semiconducting Transition Metal Dichalcogenides. *Phys Rev X* **6** (2016).

22 Yang, B. W. *et al.* Tunable spin-orbit coupling and symmetry-protected edge states in graphene/WS_2. *2d Mater* **3** (2016).

23 Wang, Z. *et al.* Strong interface-induced spin-orbit interaction in graphene on WS_2. *Nat Commun* **6** (2015).

24 Wang, Z. Y., Tang, C., Sachs, R., Barlas, Y. & Shi, J. Proximity-Induced Ferromagnetism in Graphene Revealed by the Anomalous Hall Effect. *Physical Review Letters* **114** (2015).

25 Qiao, Z. H. *et al.* Quantum Anomalous Hall Effect in Graphene Proximity Coupled to an Antiferromagnetic Insulator. *Physical Review Letters* **112** (2014).

26 Qu, Y. J., Pan, H. & Kwok, C. T. Hydrogenation-controlled phase transition on two-dimensional transition metal dichalcogenides and their unique physical and catalytic properties. *Sci Rep-Uk* **6** (2016).

27 Wang, Q. H., Kalantar-Zadeh, K., Kis, A., Coleman, J. N. & Strano, M. S. Electronics and optoelectronics of two-dimensional transition metal dichalcogenides. *Nature Nanotechnology* **7** (2012).

28 Xiao, D., Liu, G. B., Feng, W. X., Xu, X. D. & Yao, W. Coupled Spin and Valley Physics in Monolayers of MoS_2 and Other Group-VI Dichalcogenides. *Physical Review Letters* **108** (2012).

29 Zhu, Z. Y., Cheng, Y. C. & Schwingenschlogl, U. Giant spin-orbit-induced spin splitting in two-dimensional transition-metal dichalcogenide semiconductors. *Phys Rev B* **84** (2011).

30 Zeng, H. L., Dai, J. F., Yao, W., Xiao, D. & Cui, X. D. Valley polarization in MoS_2 monolayers by optical pumping. *Nature Nanotechnology* **7** (2012).

31 Mak, K. F., He, K. L., Shan, J. & Heinz, T. F. Control of valley polarization in monolayer MoS_2 by optical helicity. *Nature Nanotechnology* **7** (2012).

32 Cao, T. *et al.* Valley-selective circular dichroism of monolayer molybdenum disulphide. *Nat Commun* **3** (2012).

33 Zhong, D. *et al.* Van der Waals engineering of ferromagnetic semiconductor heterostructures for spin and valleytronics. *Sci Adv* **3** (2017).

34 Geim, A. K. & Grigorieva, I. V. Van der Waals heterostructures. *Nature* **499** (2013).

35 Lee, C. *et al.* Anomalous Lattice Vibrations of Single- and Few-Layer MoS_2. *Acs Nano* **4** (2010).

36 Alem, N. *et al.* Atomically thin hexagonal boron nitride probed by ultrahigh-resolution transmission electron microscopy. *Phys Rev B* **80** (2009).

37 Carteaux, V., Ouvrard, G., Grenier, J. C. & Laligant, Y. Magnetic-Structure of the New Layered Ferromagnetic Chromium Hexatellurosilicate $Cr_2Si_2Te_6$. *J Magn Magn Mater* **94** (1991).

38 Carteaux, V., Brunet, D., Ouvrard, G. & Andre, G. Crystallographic, Magnetic and Electronic-Structures of a New Layered Ferromagnetic Compound $Cr_2Ge_2Te_6$. *J Phys-Condens Mat* **7** (1995).

39 Li, X. X. & Yang, J. L. $CrXTe_3$ (X = Si, Ge) nanosheets: two dimensional intrinsic ferromagnetic semiconductors. *J Mater Chem C* **2** (2014).

40 Bjorkman, T., Gulans, A., Krasheninnikov, A. V. & Nieminen, R. M. van der Waals Bonding in Layered Compounds from Advanced Density-Functional First-Principles Calculations. *Physical Review Letters* **108** (2012).

41 May, A. F., Calder, S., Cantoni, C., Cao, H. B. & McGuire, M. A. Magnetic structure and phase stability of the van der Waals bonded ferromagnet $Fe_{3-x}GeTe_2$. *Phys Rev B* **93** (2016).

42 Chen, B. *et al.* Magnetic Properties of Layered Itinerant Electron Ferromagnet Fe_3GeTe_2. *J Phys Soc Jpn* **82** (2013).

43 Deiseroth, H. J., Aleksandrov, K., Reiner, C., Kienle, L. & Kremer, R. K. Fe_3GeTe_2 and Ni_3GeTe_2 - Two new layered transition-metal compounds: Crystal structures, HRTEM investigations, and magnetic and electrical properties. *Eur J Inorg Chem* (2006).

44 Zhuang, H. L. L., Xie, Y., Kent, P. R. C. & Ganesh, P. Computational discovery of ferromagnetic semiconducting single-layer $CrSnTe_3$. *Phys Rev B* **92** (2015).

45 Huang, B. *et al.* Layer-dependent ferromagnetism in a van der Waals crystal down to the monolayer limit. *Nature* **546** (2017).

46 McGuire, M. A., Dixit, H., Cooper, V. R. & Sales, B. C. Coupling of Crystal Structure and Magnetism in the Layered, Ferromagnetic Insulator CrI_3. *Chem Mater* **27** (2015).

47 Tsubokawa, I. On the Magnetic Properties of a $CrBr_3$ Single Crystal. *J Phys Soc Jpn* **15** (1960).

48 Cable, J. W., Wilkinson, M. K. & Wollan, E. O. Neutron Diffraction Investigation of Antiferromagnetism in $CrCl_3$. *J Phys Chem Solids* **19** (1961).

49 Hansen, W. N. & Griffel, M. Heat Capacities of CrF_3 and $CrCl_3$ from 15-Degrees-K to 300-Degrees-K. *J Chem Phys* **28** (1958).

50 Gong, C. *et al.* Discovery of intrinsic ferromagnetism in two-dimensional van der Waals crystals. *Nature* **546** (2017).

51 Kane, C. L. & Mele, E. J. Quantum spin Hall effect in graphene. *Physical Review Letters* **95** (2005).

52 Kane, C. L. & Mele, E. J. Z(2) topological order and the quantum spin Hall effect. *Physical Review Letters* **95** (2005).

53 Castro Neto, A. H. & Guinea, F. Impurity-Induced Spin-Orbit Coupling in Graphene. *Physical Review Letters* **103** (2009).

54 Elias, D. C. *et al.* Control of Graphene's Properties by Reversible Hydrogenation: Evidence for Graphane. *Science* **323** (2009).

55 Balakrishnan, J., Koon, G. K. W., Jaiswal, M., Neto, A. H. C. & Ozyilmaz, B. Colossal enhancement of spin-orbit coupling in weakly hydrogenated graphene. *Nature Physics* **9** (2013).

56 Cheng, S. H. *et al.* Reversible fluorination of graphene: Evidence of a two-dimensional wide bandgap semiconductor. *Phys Rev B* **81** (2010).

57 Zhou, J., Liang, Q. F. & Dong, J. M. Enhanced spin-orbit coupling in hydrogenated and fluorinated graphene. *Carbon* **48** (2010).

58 Schmidt, M. J. & Loss, D. Edge states and enhanced spin-orbit interaction at graphene/graphane interfaces. *Phys Rev B* **81** (2010).

59 Lee, C., Wei, X. D., Kysar, J. W. & Hone, J. Measurement of the elastic properties and intrinsic strength of monolayer graphene. *Science* **321** (2008).

60 Kim, E. A. & Castro Neto, A. H. Graphene as an electronic membrane. *Epl-Europhys Lett* **84** (2008).

61 Casolo, S., Lovvik, O. M., Martinazzo, R. & Tantardini, G. F. Understanding adsorption of hydrogen atoms on graphene. *J Chem Phys* **130** (2009).

62 Chernozatonskii, L. A., Sorokin, P. B., Belova, E. E., Bruning, J. & Fedorov, A. S. Superlattices consisting of "lines" of adsorbed hydrogen atom pairs on graphene. *Jetp Lett* **85** (2007).

63 Boukhvalov, D. W., Katsnelson, M. I. & Lichtenstein, A. I. Hydrogen on graphene: Electronic structure, total energy, structural distortions and magnetism from first-principles calculations. *Phys Rev B* **77** (2008).

64 Sofo, J. O., Chaudhari, A. S. & Barber, G. D. Graphane: A two-dimensional hydrocarbon. *Phys Rev B* **75** (2007).

65 Castellanos-Gomez, A., Wojtaszek, M., Arramel, Tombros, N. & van Wees, B. J. Reversible Hydrogenation and Bandgap Opening of Graphene and Graphite Surfaces Probed by Scanning Tunneling Spectroscopy. *Small* **8** (2012).

66 Balog, R. *et al.* Bandgap opening in graphene induced by patterned hydrogen adsorption. *Nat Mater* **9** (2010).

67 Cancado, L. G. *et al.* Quantifying Defects in Graphene via Raman Spectroscopy at Different Excitation Energies. *Nano Letters* **11** (2011).

68 Mihajlovic, G., Pearson, J. E., Garcia, M. A., Bader, S. D. & Hoffmann, A. Negative Nonlocal Resistance in Mesoscopic Gold Hall Bars: Absence of the Giant Spin Hall Effect. *Physical Review Letters* **103** (2009).

69 Abanin, D. A., Shytov, A. V., Levitov, L. S. & Halperin, B. I. Nonlocal charge transport mediated by spin diffusion in the spin Hall effect regime. *Phys Rev B* **79** (2009).

70 Sui, M. Q. *et al.* Gate-tunable topological valley transport in bilayer graphene. *Nature Physics* **11** (2015).

71 Schmidt, G., Ferrand, D., Molenkamp, L. W., Filip, A. T. & van Wees, B. J. Fundamental obstacle for electrical spin injection from a ferromagnetic metal into a diffusive semiconductor. *Phys Rev B* **62** (2000).

72 Fert, A. & Jaffres, H. Conditions for efficient spin injection from a ferromagnetic metal into a semiconductor. *Phys Rev B* **64** (2001).

73 Tombros, N., Jozsa, C., Popinciuc, M., Jonkman, H. T. & van Wees, B. J. Electronic spin transport and spin precession in single graphene layers at room temperature. *Nature* **448** (2007).

74 Amamou, W. *et al.* Contact induced spin relaxation in graphene spin valves with Al_2O_3 and MgO tunnel barriers. *Apl Mater* **4** (2016).

75 Wen, H. *et al.* Experimental Demonstration of XOR Operation in Graphene Magnetologic Gates at Room Temperature. *Phys Rev Appl* **5** (2016).

76 Dlubak, B. *et al.* Homogeneous pinhole free 1 nm Al_2O_3 tunnel barriers on graphene. *Appl Phys Lett* **101** (2012).

77 Dlubak, B. *et al.* Are Al_2O_3 and MgO tunnel barriers suitable for spin injection in graphene? *Appl Phys Lett* **97** (2010).

78 Jedema, F. J., Heersche, H. B., Filip, A. T., Baselmans, J. J. A. & van Wees, B. J. Electrical detection of spin precession in a metallic mesoscopic spin valve. *Nature* **416** (2002).

79 Sosenko, E., Wei, H. Z. & Aji, V. Effect of contacts on spin lifetime measurements in graphene. *Phys Rev B* **89** (2014).

80 Maassen, T., Vera-Marun, I. J., Guimaraes, M. H. D. & van Wees, B. J. Contact-induced spin relaxation in Hanle spin precession measurements. *Phys Rev B* **86** (2012).

81 Popinciuc, M. *et al.* Electronic spin transport in graphene field-effect transistors. *Phys Rev B* **80** (2009).

82 Mermin, N. D. & Wagner, H. Absence of Ferromagnetism or Antiferromagnetism in One- or 2-Dimensional Isotropic Heisenberg Models. *Physical Review Letters* **17** (1966).

83 Bloch, D., Chaisse, F. & Pauthenet, R. Variation Avec La Pression Des Points De Curie De Quelques Ferrites Dyttrium Et De Terres Rares a Structure Grenat. *Cr Acad Sci B Phys* **262** (1966).

84 Kaminow, I. P. & Jones, R. V. Pressure Dependence of the Microwave Resonance Properties of Some Spinel and Garnet Ferrites. *Phys Rev* **123** (1961).

85 Sawaoka, A. & Kawai, N. The Effect of Hydrostatic Pressure on the Magnetic Anisotropy of Ferrous and Ferric Ions in Ferrites with Spinel Structure. *J Phys Soc Jpn* **25** (1968).

86 Chi, Z. H. *et al.* Pressure-Induced Metallization of Molybdenum Disulfide. *Physical Review Letters* **113** (2014).

87 Nayak, A. P. *et al.* Pressure-induced semiconducting to metallic transition in multilayered molybdenum disulphide. *Nat Commun* **5** (2014).

88 Proctor, J. E. *et al.* High-pressure Raman spectroscopy of graphene. *Phys Rev B* **80** (2009).

89 Zhang, X. *et al.* Magnetic anisotropy of the single-crystalline ferromagnetic insulator Cr2Ge2Te6. *Jpn J Appl Phys* **55** (2016).

90 Xing, W. Y. *et al.* Electric field effect in multilayer $Cr_2Ge_2Te_6$: a ferromagnetic 2D material. *2d Mater* **4** (2017).

91 Ji, H. W. *et al.* A ferromagnetic insulating substrate for the epitaxial growth of topological insulators. *J Appl Phys* **114** (2013).

92 Alegria, L. D. *et al.* Large anomalous Hall effect in ferromagnetic insulator-topological insulator heterostructures. *Appl Phys Lett* **105** (2014).

93 Xiang, Z. J. *et al.* Pressure-Induced Electronic Transition in Black Phosphorus. *Physical Review Letters* **115** (2015).

94 Han, W., Kawakami, R. K., Gmitra, M. & Fabian, J. Graphene spintronics. *Nature Nanotechnology* **9** (2014).

95 Yang, T. Y. *et al.* Observation of Long Spin-Relaxation Times in Bilayer Graphene at Room Temperature. *Physical Review Letters* **107** (2011).

96 Pi, K. *et al.* Manipulation of Spin Transport in Graphene by Surface Chemical Doping. *Physical Review Letters* **104** (2010).

97 Kormanyos, A. *et al.* k.p theory for two-dimensional transition metal dichalcogenide semiconductors. *2d Mater* **2** (2015).

98 Gmitra, M. & Fabian, J. Graphene on transition-metal dichalcogenides: A platform for proximity spin-orbit physics and optospintronics. *Phys Rev B* **92** (2015).

99 Pierre, F. *et al.* Dephasing of electrons in mesoscopic metal wires. *Phys Rev B* **68** (2003).

100 Tikhonenko, F. V., Horsell, D. W., Gorbachev, R. V. & Savchenko, A. K. Weak localization in graphene flakes. *Physical Review Letters* **100** (2008).

101 McCann, E. *et al.* Weak-localization magnetoresistance and valley symmetry in graphene. *Physical Review Letters* **97** (2006).

102 Min, H. *et al.* Intrinsic and Rashba spin-orbit interactions in graphene sheets. *Phys Rev B* **74** (2006).

103 Tikhonenko, F. V., Kozikov, A. A., Savchenko, A. K. & Gorbachev, R. V. Transition between Electron Localization and Antilocalization in Graphene. *Physical Review Letters* **103** (2009).

104 Gershenzon, M. E., Gubankov, V. N. & Zhuravlev, Y. E. Weak Localization and Electron-Scattering in Silver Thin-Films. *Jetp Lett+* **35** (1982).

105 Hwang, E. H. & Das Sarma, S. Single-particle relaxation time versus transport scattering time in a two-dimensional graphene layer. *Phys Rev B* **77** (2008).

106 Stauber, T., Peres, N. M. R. & Guinea, F. Electronic transport in graphene: A semiclassical approach including midgap states. *Phys Rev B* **76** (2007).

107 Dyakonov, M. I. & Perel, V. I. Spin Relaxation of Conduction Electrons in Noncentrosymmetric Semiconductors. *Sov. Phys. Solid State* **13** (1972).

108 Elliott, R. J. Theory of the Effect of Spin-Orbit Coupling on Magnetic Resonance in Some Semiconductors. *Phys Rev* **96** (1954).

109 McCann, E. & Fal'ko, V. I. z -> -z Symmetry of Spin-Orbit Coupling and Weak Localization in Graphene. *Physical Review Letters* **108** (2012).

110 Rutter, G. M. *et al.* Microscopic polarization in bilayer graphene. *Nature Physics* **7** (2011).

111 Zhang, H. J. *et al.* Topological insulators in Bi_2Se_3, Bi_2Te_3 and Sb_2Te_3 with a single Dirac cone on the surface. *Nature Physics* **5** (2009).

112 Konig, M. *et al.* Quantum spin hall insulator state in HgTe quantum wells. *Science* **318** (2007).

113 Bernevig, B. A., Hughes, T. L. & Zhang, S. C. Quantum spin Hall effect and topological phase transition in HgTe quantum wells. *Science* **314** (2006).

114 Gmitra, M., Kochan, D., Hogl, P. & Fabian, J. Trivial and inverted Dirac bands and the emergence of quantum spin Hall states in graphene on transition-metal dichalcogenides. *Phys Rev B* **93** (2016).

115 Rengel, R. & Martin, M. J. Diffusion coefficient, correlation function, and power spectral density of velocity fluctuations in monolayer graphene. *J Appl Phys* **114** (2013).

116 McCann, E. & Koshino, M. The electronic properties of bilayer graphene. *Rep Prog Phys* **76** (2013).

117 Li, J. *et al.* Effective mass in bilayer graphene at low carrier densities: The role of potential disorder and electron-electron interaction. *Phys Rev B* **94** (2016).

118 Chen, J. H. *et al.* Charged-impurity scattering in graphene. *Nature Physics* **4** (2008).

119 Minot, E. D. *et al.* Tuning carbon nanotube band gaps with strain. *Phys Rev Lett* **90** (2003).

120 Heyd, R., Charlier, A. & McRae, E. Uniaxial-stress effects on the electronic properties of carbon nanotubes. *Phys Rev B* **55** (1997).

121 Yang, L. & Han, J. Electronic structure of deformed carbon nanotubes. *Physical Review Letters* **85** (2000).

122 Ni, Z. H. *et al.* Uniaxial Strain on Graphene: Raman Spectroscopy Study and Band-Gap Opening. *Acs Nano* **2** (2008).

123 Giovannetti, G., Khomyakov, P. A., Brocks, G., Kelly, P. J. & van den Brink, J. Substrate-induced band gap in graphene on hexagonal boron nitride: Ab initio density functional calculations. *Phys Rev B* **76** (2007).

124 Ribeiro, R. M., Peres, N. M. R., Coutinho, J. & Briddon, P. R. Inducing energy gaps in monolayer and bilayer graphene: Local density approximation calculations. *Phys Rev B* **78** (2008).

125 Zhou, S. Y. *et al.* Substrate-induced bandgap opening in epitaxial graphene. *Nat Mater* **6** (2007).

126 Castro, E. V. *et al.* Biased bilayer graphene: Semiconductor with a gap tunable by the electric field effect. *Physical Review Letters* **99** (2007).

127 Lee, J. U., Yoon, D. & Cheong, H. Estimation of Young's Modulus of Graphene by Raman Spectroscopy. *Nano Letters* **12** (2012).

128 Neek-Amal, M. & Peeters, F. M. Nanoindentation of a circular sheet of bilayer graphene. *Phys Rev B* **81** (2010).

129 Choi, S. M., Jhi, S. H. & Son, Y. W. Controlling Energy Gap of Bilayer Graphene by Strain. *Nano Letters* **10** (2010).

130 Son, Y. W., Cohen, M. L. & Louie, S. G. Half-metallic graphene nanoribbons. *Nature* **444** (2006).

131 McCann, E. Asymmetry gap in the electronic band structure of bilayer graphene. *Phys Rev B* **74** (2006).

132 Ohta, T., Bostwick, A., Seyller, T., Horn, K. & Rotenberg, E. Controlling the electronic structure of bilayer graphene. *Science* **313** (2006).

133 Zhang, Y. B. *et al.* Direct observation of a widely tunable bandgap in bilayer graphene. *Nature* **459** (2009).

134 Kaverzin, A. A., and B. J. van Wees. Electron transport nonlocality in monolayer graphene modified with hydrogen silsesquioxane polymerization. *Phys Rev B* **91** (2015).

135 Wang, W. H., *et al*. "Growth of atomically smooth MgO films on graphene by molecular beam epitaxy." *Applied Physics Letters* **93** (2008).

136 Popinciuc, M., *et al*. "Electronic spin transport in graphene field-effect transistors." *Phys Rev B* **80** (2009).

137 Qiao, Zhenhua, *et al*. "Quantum anomalous Hall effect in graphene from Rashba and exchange effects." *Phys Rev B* **82** (2010).